2018•2019

Faculteit Industriële ingenieurswetenschappen

master in de industriële wetenschappen: chemie

Masterthesis

High-Shear Wet Milling of API's

PROMOTOR :

Prof. dr. ir. Leen BRAEKEN

PROMOTOR :

dr. ing. Bjorn GIELEN

Arno De Vos

Scriptie ingediend tot het behalen van de graad van master in de industriële wetenschappen: chemie

Gezamenlijke opleiding UHasselt en KU Leuven

UHASSELT KU LEUVEN

UHASSELT KU LEUVEN

2018•2019

Faculteit Industriële ingenieurswetenschappen

master in de industriële wetenschappen: chemie

Masterthesis

High-Shear Wet Milling of API's

PROMOTOR :

Prof. dr. ir. Leen BRAEKEN

PROMOTOR :

dr. ing. Bjorn GIELEN

Arno De Vos

Scriptie ingediend tot het behalen van de graad van master in de industriële wetenschappen: chemie

ACKNOWLEDGEMENTS

This master's thesis, made as a part of my chemical engineering technology education, could not be realized without the support of a few people and, therefore, I want to express my gratefulness.

First of all, I would like to thank my supervisors, dr. ing. Bjorn Gielen and prof. dr. ir. Leen Braeken, for the delivered feedback, the necessary corrections, the trust, the input and the motivation during the whole period of research and writing. Their effort and enthusiasm ensured a pleasant collaboration, where I had the opportunity to learn a lot.

In addition, I want to thank the staff members from the crystallization unit (CTU) situated on the research and development site of Janssen Pharmaceutica in Beerse. Their interest on the subject, help in the lab and stories during the lunch break made me quickly feel at ease. Their proposals and questions about the experiments and the results, gave me the feeling that I was more involved in the daily operations of the company.

Also, I want to thank dr. Jeroen Lievens for the help during the writing work. Furthermore, I would like to express my gratitude towards my fellow students, in particular Stef Picard, for his help remembering the deadlines, and Dylan Caproens, for his feedback over the assignments such as the abstract and the poster.

Finally, I want to thank my family and girlfriend for their support and trust, despite my, sometimes, stressful mood. Their support and availability was the ideal outlet to forget all the stress and worries for a minute.

TABLE OF CONTENT

TABLE LIST

FIGURE LIST

GLOSSARY

μ_{tip}	Tip-speed
API	Active Pharmaceutical Ingredient
BCS	Biopharmaceutical Classification System
BI	Brittleness Index
Co	Comminution Number
D	Rotor Diameter *[m]*
E	Elasticity *[GPa]*
FBRM	Focused Beam Reflectance Measurement
H	Hardness *[GPa]*
HSWM	High-Shear Wet Mill
IST	Inertial Subrange Turbulence
Kc	Fracture Toughness *[MPa $m^{1//2}$]*
MT	Macroscale Turbulence
NaCl	Sodium Chloride
PVM	Particle Vision and Measurement
RBI	Relative Backscatter Index
RMSE	Root-Mean-Square Error
RPM	Rotations Per Minute
Rs	Shear Rate
SEM	Scanning Electron Microscope
v	Velocity *[m/s]*
ρ	Density *[kg/m³]*
w	Angular Speed *[rad/s]*

ABSTRACT

The research and development site of Janssen Pharmaceutica, situated in Beerse, works on the improvement of the bioavailability of the active pharmaceutical compound, which is responsible for the medicinal effect of a drug. A popular method is increasing the specific surface area, wherefor dry milling units are used. Currently, for safety and efficiency reasons, wet milling units are increasing in popularity. This master's thesis investigates the influence of solid properties and mechanical properties of the wet mill on the breaking mechanism of crystals.

A high-shear wet mill (HSWM) is gravitationally placed under a two liter vessel. The output of the HSWM is piloted back in the reactor, creating a recycle loop. A focused beam reflectance measurement (FBRM) keeps track of the particles and their size to determine the influence of different solids, solid loading, starting size, RPM… on the breakage. Besides, the influence of a different setup was compared, to determine the influence of possible segregation.

The research shows that the influence of the set-up, starting size and solid loading is negligible. The influence of different RPM and solid properties is compared to a previous research, to validate the results. Notable is the breakage of sodium chloride, that deviates from the theory. Finally, the influence of tip-speed turns out to be the most significant on the breakage mechanism. As the tip-speed increases, the distribution of the particle size narrows and lower C90 values can be achieved.

ABSTRACT IN DUTCH

De onderzoeks- en ontwikkelingssite van Janssen Pharmaceutica te Beerse werkt aan de verbetering van de biologische beschikbaarheid van de actieve farmaceutische component, verantwoordelijk voor het medicinale effect van een medicijn. Een populaire methode hiervoor is het vergroten van het specifieke oppervlak van de component. Tegenwoordig worden hiervoor wet mills gebruikt. Deze masterthesis bestudeert de invloed van de kristaleigenschappen en de mechanische eigenschappen van de maler op het brekingsmechanisme.

Een high-shear maler wordt gravitair onder een 2L vat geplaatst. De uitlaat van de maler wordt teruggeleid naar de reactor om zo een recycle stroom te creëren. In het vat worden het aantal deeltjes en hun grootte gedurende het maalproces opgevolgd aan de hand van een FBRM-meettoestel, om zo de invloed van verschillende materialen, massa lading, start grootte… op de breking te testen. Daarnaast wordt een tweede opstelling getest om de invloed van mogelijke segregatie te bepalen.

Het onderzoek toont dat de invloed van de verschillende opstellingen, massa lading, start grootte en HSWM configuratie verwaarloosbaar is. De invloed van de rotor snelheid en kristaleigenschappen zijn, ter validatie, vergeleken met een eerder uitgevoerd onderzoek. Hier blijkt de breking van natriumchloride af te wijken van de theorie. De invloed van de verschillende rotor-snelheden blijkt wel een grote invloed te hebben op het maalgedrag. Een grotere tip-speed zorgt voor een smallere verdeling van de kristalgrootte en een lagere C90 grootte.

1 INTRODUCTION

Janssen Pharmaceutica is an international, pharmaceutical company of Johnsen&Johnson (J&J) working to prevent, treat, cure and stop diseases all over the world [1]. The research and development site, situated in Beerse (Antwerp), is responsible for the product- and process innovation of various Active Pharmaceutical Ingredients (API's), which are subsequently commercialized in the form of medicines.

During the synthesis of de API's, several purification steps are necessary. The final purification step, after synthesis, often is the crystallization, where the API is, next to purified, converted in the required morphology. Next to the morphology, the efficiency of API is directly related to the solubility of the compound. Traditionally, this solubility is manipulated through several methods such as salt forming and adding excipients. However, due to the recent lack of success and possible toxic side effects of these methods, the popularity of size reduction for increasing specific surface area and subsequently increasing solubility is rising.

Size reduction is often achieved via dry milling. Due to safety risks associated with dry milling, pharmaceutical companies attempt to shift from the dry mills to wet mills. Unfortunately, the knowledge about these instruments is still limited. Therefore, this master's thesis focusses on the influence of several properties on the working mechanism of IKA Magic Lab® rotor-stator high-shear wet mill (HSWM), in the context of possibly designing a scale-up method in the future. During this research, only model compounds in sucrose, ascorbic acid, glycine and sodium chloride are used.

Within Janssen Pharmaceutica, the set-up of lab scale HSWM experiments differs from the production set-up. Since the scale-up is not sufficient, the question raises whether the difference in set-up can have a large influence on the breakage mechanism. Therefore, the two set-ups are compared on lab scale to discover the influence hereof. In order to avoid the possible influence of the set-up on the following tests, the production scale set-up is consistently used over all experiments.

Furthermore, the influence of compound dependable properties on the milling process is tested. Different solid loading is compared to determine the influence of particle-particle breakage. The starting particle size of sucrose is compared by examining respectively a starting size between 250 µm – 450 µm mesh size and 450 µm – 1 mm mesh size. Thereafter, the specific properties (e.g. hardness, elasticity, fracture toughness) dependable theory, established by Ghaderzadeh, is validated using the same compounds and sodium chloride.

Next to the influence of solid properties, the influence of operational properties is analyzed. The milling chamber of IKA's Magic Lab® can be self-compiled. Therefore, the influence of different rotor-stator compilations is tested with all variables constant. Besides, the rotational speed of the rotor can be picked, with flowrate and shear differences as a result.

This master's thesis consists of 4 chapters. First of all, the reader receives a theoretical background through a literature study which respectively describes the API, various crystallization processes, particle size reduction and previous scale-up attempts. Thereafter, the material and methods illustrates the experimental procedure used during the experiments and the various characterization equipment, both on-line and off-line instruments, applied for particle size measurements and imaging. Furthermore, the third chapter consists of the results and discussion concerning the experiences made around the influential properties on the HSWM mechanism and the validation of Ghaderzadeh's theory. Finally, the conclusion summarizes the most important results and ends with a few recommendations.

2 LITERATURE STUDY

This literature study is divided in four chapters. First, a broad overview of the active pharmaceutical ingredient (API) is given: the working process, a short production process, classification…. Thereafter, in chapter two, the crystallization process of API's is discussed. Subsequently, more information about the particle size reduction and influential parameters concerning the breaking mechanism are clarified. Finally, some previous scale-up methods are discussed.

2.1 ACTIVE PHARMACEUTICAL INGREDIENT

An active pharmaceutical ingredient (API) is the active component in a pharmaceutical drug that is responsible for the effects of the drug. Manufacturing such a component is usually done in five steps, as illustrated in Figure 1: organic synthesis, crystallization, filtration, drying process and formulation. The organic synthesis of an API strives to develop a route that consists of 5 to 10 synthetic steps, starting with basic organic compounds. Because the API, after the organic synthesis, is still contaminated with impurities, a crystallization step is required to purify the component. The crystallization will be discussed further in the literature study. After the purification, the formed solid crystals are filtered from the slurry and dried. Finally, during the formulation the API is combined with different components, producing the final medicinal product.

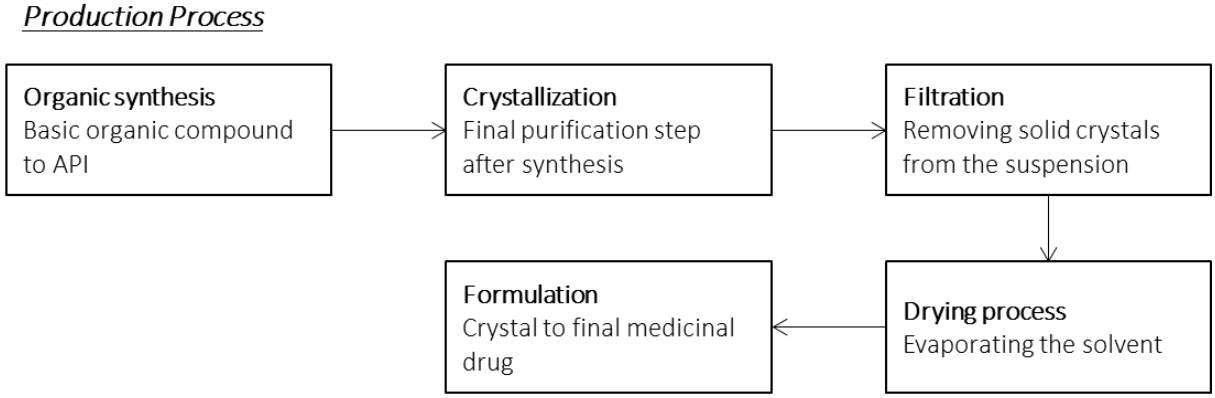

Figure 1 - Production process of an API

A commonly known example of an API is acetaminophen, better known as paracetamol, which is generally used for treating pain. For a drug to enter the bloodstream, it has to be absorbed through the membrane. This absorption determines the bioavailability of the API and depends on mainly two factors: solubility and permeability. Therefore, the efficiency of API's is directly related to those two factors. First of all, the drug needs to be dissolved in order for absorption to take place. Even if the substance is in solution, the absorption may not take place due to low permeability, which is a rate of how easily the substance can diffuse through the membrane.

To distinguish API's, based on their bioavailability, a Biopharmaceutic Classification System (BCS) is designed [2]. Using this classification system, it is possible to predict the *in vivo* pharmacokinetic performance of drug products based on the permeability and solubility of the API [3]. The pharmacokinetic performance of a drug is a mathematical description of the

concentration in body fluids based on the dose of the administered drug. It is determined by the absorption rate through the membrane, drug distribution rate and the drug elimination due to metabolism and excretion [4]. As suggested in Figure 2, the BCS consists of 4 classes. Over 60% of the recently discovered crystallizable API's have low solubility in water (<10 mg/L) [5], [6], therefore they belong to the classes II and IV.

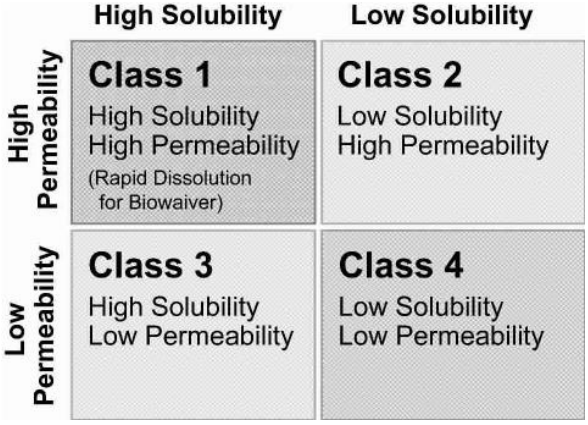

Figure 2 – Biopharmaceutical classification system [3]

The bioavailability of API's of BCS class IV is limited due to low solubility and low permeability. Due to the double limitations, improving only the solubility does not suffice to increase the bioavailability. Nevertheless, bioavailability of BCS class IV compounds can still be improved by combining solubility improvement with absorption enhancers (e.g. sodium caprate, sodium deoxycholate) [7], [8]. The bioavailability of API's of BCS class II is only limited due to the solubility of the substance, thus increasing the bioavailability is possible, thanks to the high permeability, by improving the solubility of the API. Currently, salt-forming and adding excipients are the most used methods to increase the solubility and dissolution rate, which are simplistically related by the Noyes–Whitney, Equation 1 [9]. Because these methods aren't always successful and can even entail toxic side effects, increasing the specific surface area (SS_A), due to particle size reduction, can be a good alternative to increase the solubility. [10], [11]

$$J = K \cdot A \cdot (C_s - C)$$

$$J = dissolution\ rate$$

$$K = constant$$

$$A = surface\ area\ solid \quad (1)$$

$$C_s = solubility$$

$$C = concentration\ in\ medium$$

The principle of salt formation is to pair an API with an appropriate counterion. This influences the physiochemical properties of the API, often without changing the pharmacological properties of the medicinal drug. Inside the intestine (pH 7), the salt buffer will release protons, decreasing the pH of the microenvironment of the drug resulting in an increasing solubility and

dissolution rate of a basic drug, while in the stomach (pH 1.5), the salt buffer will increase the pH of the microenvironment of the drug resulting in an increasing solubility and dissolution rate of an acidic drug [12]. For example, the dissolution rate of the sodium salt of tolbutamide is approximately 5 000 times faster in acidic media then the free acid. [12], [13]

Solubility is dependent on the free energy of the solid and the molecules in solution. The free energy of the solid is constant, while the free energy of the molecules in solution depends on the solvent and the solution concentration. When the solution is saturated, the energy levels of the solid and the molecules in solution are equal. The principle of an excipient is to decrease the chemical potential of the molecules in solution, increasing the necessary solution concentration (i.e., solubility) to achieve the equilibrium. There are various types of excipients, for example via specific interactions such as complexation [14].

2.2 CRYSTALLIZATION

During the organic synthesis of API's, several purification steps are performed ending with a final crystallization, as suggested in Figure 1. Crystallization is a separation process that consists of two consecutive steps: nucleation and crystal growth. During the nucleation microscopic solid particles with a crystal structure, nuclei, are formed from a homogeneous mixture due to the random collisions between the many atoms and molecules in the mixture. The formed nuclei can then dissolve in the mixture, or grow into bigger crystals. This crystal growth occurs thanks to the diffusion of molecules towards the nuclei surface, causing them to attach on the nuclei, increasing its size. [15]

The crystallization process depends on the difference in chemical potential between the solid phase and the liquid phase. Although, in practice, the term supersaturation is often used. Supersaturation is the concentration of a certain product in a solvent that exceeds the theoretical solubility at a given pressure and temperature, as illustrated in Figure 4. Various crystallization techniques are available to achieve this oversaturation. Most commonly cooling crystallization, anti-solvent crystallization or evaporative crystallization are used [16].

2.2.1 Nucleation and Crystal growth

As mentioned above, crystallization consists of two consecutive steps: nucleation and crystal growth. Nucleation can be divided into primary and secondary nucleation. Where the primary nucleation can be subdivided into homogeneous and heterogeneous primary nucleation. This is illustrated in Figure 3.

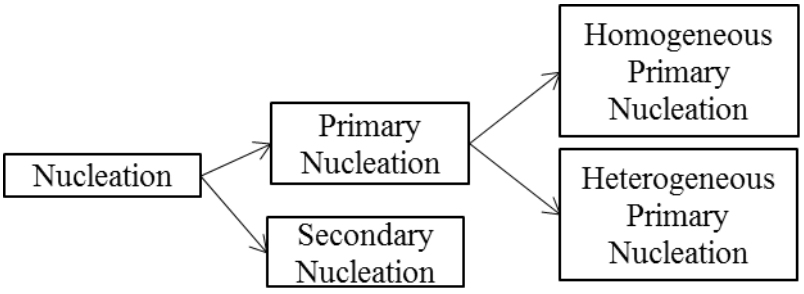

Figure 3 – Schematically nucleation process

Primary nucleation is the formation of nuclei in the solution, as there are no nuclei formed yet. This nucleation happens due to higher energy levels mostly thanks to a temperature difference. If the nucleation takes place in absence of solid phase materials, such as a stirrer and the reactor wall, it is called a primary homogeneous nucleation. Whereas nucleation takes place on the surface of solid phase materials, as exclusively happens in practice, is called primary heterogeneous nucleation [17]. Nucleation that takes place while crystals are already present is called secondary nucleation. As the present crystals positively influence the nucleation, secondary nucleation takes place at lower supersaturation.

Crystal growth is the attachment of molecules and atoms at the present nuclei, causing the nuclei to grow in size. Hereby, the rate of crystal growth depends on the diffusion of the molecules,

as well as the attachment of the molecules on the crystal lattice. The crystal growth rate is given in Equation (2) [18].

$$N = K \cdot A \cdot (y - y_s) \tag{2}$$

Where N illustrates the growth rate, K the mass transfer coefficient, A the surface area of the crystal, y the concentration of the solution and y_s the theoretical solubility. The difference between the concentration in solution and the theoretical solubility gives the supersaturation.

2.2.2 Cooling crystallization

Cooling crystallization responds to the temperature dependence of the solubility. As suggested in Figure 4, the solubility of most API's is proportional to the temperature. The higher the temperature, the higher the sensitivity of the solubility. An unsaturated solution (point A, Figure 4) is the starting point of the cooling crystallization. If the temperature decreases, the solubility curve will be exceeded at a certain point (point B, Figure 4). The solution, of which solid phase and liquid phase are now in chemical balance, is currently part of the metastable zone (MSZ), which is the zone between unsaturated and supersaturated where no spontaneous nucleation occurs [19]. As the solution is further cooled, it will approach the supersaturation curve, where spontaneous nucleation can occur (point C, Figure 4). Due to the nucleation and crystal growth, the concentration in the solution will lower (point D, Figure 4), repeating the process described above.

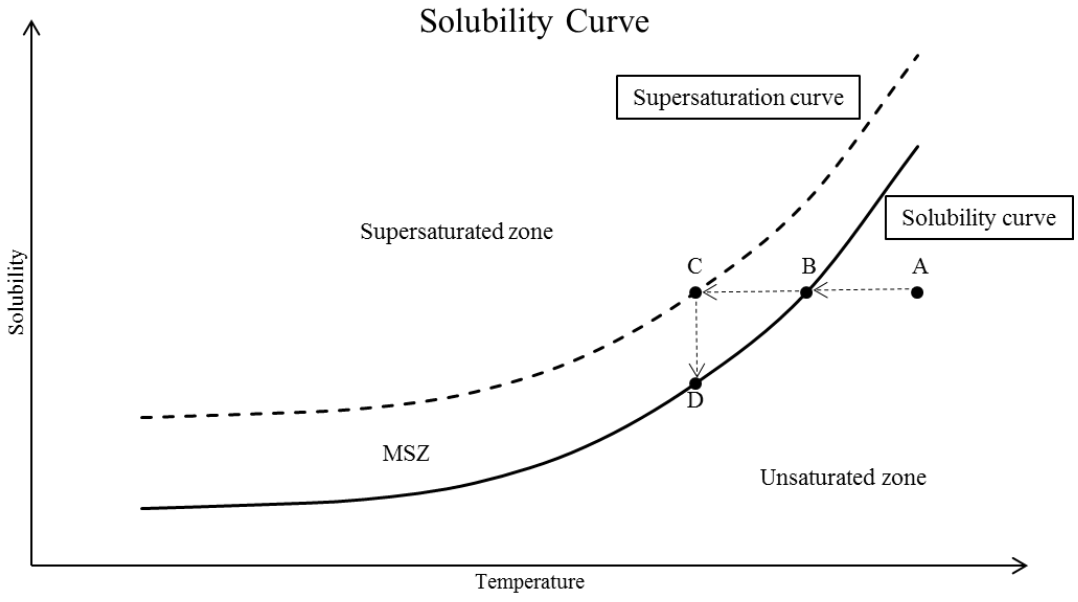

Figure 4 - Solubility curve, MSZ and saturation zones

Cooling crystallization is often used when an API has low solubility and the solubility is strongly temperature dependent. API's with a high solubility will dissolve really easy, making the necessary temperature difference to approach the supersaturation curve too high.

2.2.3 Anti-solvent dosage

The solubility of a compound differs in various solvents, for example sucrose has a high solubility in water (2100 g/L at 25 °C) but is insoluble in ethyl ether [20]. Solvents, in which a compound does not dissolve, are called anti-solvents. As the crystallizable compound is dissolved in a solvent, the solubility can be manipulated by dosing anti-solvent. As the amount of anti-solvent increases, the solubility will decrease causing the solubility curve, illustrated in Figure 5, to be exceeded and approach the supersaturation zone, starting the crystallization. As the crystallization is started, the solid concentration will drop because the solids come out of the solution. The trend will not follow the solubility curve exactly, due to a buildup that cannot be relieved fast enough through crystal growth and nucleation [21].

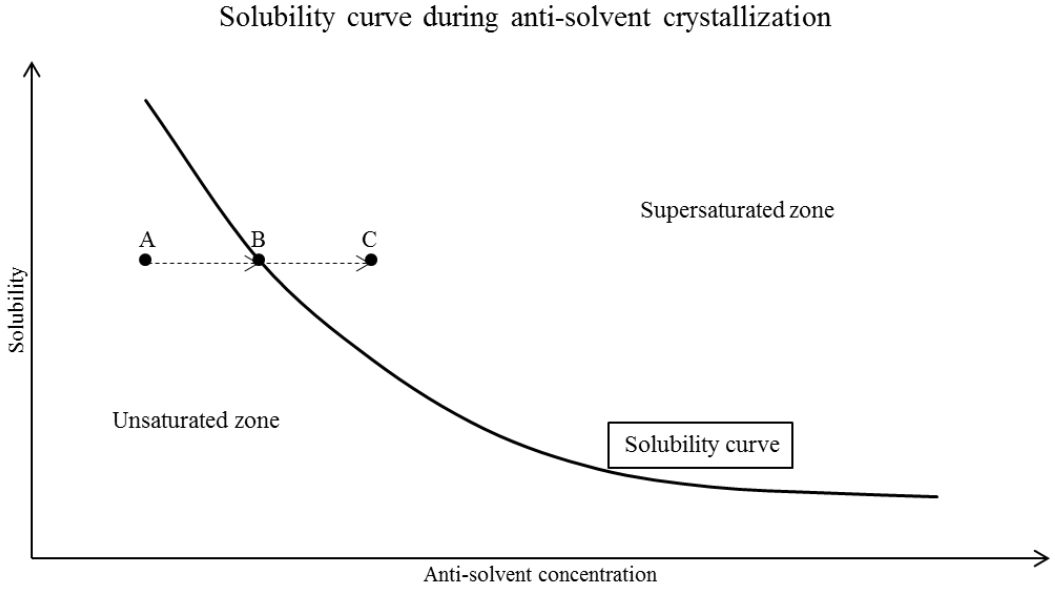

Figure 5 - Solubility curve anti-solvent crystallization

Often, this crystallization technique is utilized when substances are heat-sensitive, the compound is highly soluble in the solvent and the solubility is only weakly dependent on the temperature. If the anti-solvent can easily be separated from the solvent, anti-solvent crystallization can be assumed a low energy method. Although, the disadvantage of the method is that it is highly mixing dependent. If the mixture is not mixed homogeneously, local supersaturations can originate with high possibility for agglomeration, which is the accumulation of crystals. [22], [23]

2.2.4 Evaporative crystallization

The solubility of a compound is expressed in mass compound per mass solvent. By reducing the mass of the solvent and keeping the compound mass in the mixture constant, oversaturation will be created. Due to the high energy need of evaporative crystallization, it is most commonly used with substances where the solubility curve in function of the temperature, as illustrated in Figure 4, is so flat that the yield using cooling crystallization, discussed above, would be negligible or when the residual solubility remains too high for achievable temperatures during the cooling [24]. [25]

2.2.5 Particle Tuning

Besides the particle size, particle morphology and surface texture are other influential properties of a crystal. The crystallization conditions are critical to influence these properties [26]. Zeng et al. studied the influence of various crystallization conditions (e.g. solid loading, temperature…) on the morphology and surface texture of lactose. As the majority of the lactose crystals were tomahawk-shaped or pyramidal after a crystallization with an initial solid concentration in between 33% w/w and 43% w/w, the morphology changed to prismatic as the solid loading increased to around 50% w/w. From here, an increase in solid concentration causes the particles to elongate. Next to these influences, the temperature at which the crystallization is performed particularly influenced the regularity of the shape and smoothness of the surface area. A decrease in temperature caused a decrease in regularity. [26]

Another major influence in morphology can be obtained by changing the solvent. In theory the morphology of a interface between liquid and solid particles is been quantified as the α-factor [27]. This factor strongly depends on the solubility of the solids and the heat of the solution. Due to the influence of the solvent on the solubility and temperature, it is reasonable to conclude that the morphology is strongly dependent on the used solvent.[27]

2.3 PARTICLE SIZE REDUCTION

2.3.1 Increasing dissolution rate

Particle size reduction is directly associated with an increase of specific surface area ([m^2/m^3]), expressed as the surface of a compound per volume unit of the compound. As the particles have the same density, and the mass is constant, the volume of particles after size reduction is the same. As illustrated in Figure 6, the specific surface area of a spherical compound will increase exponentially, while the surface of one particle will decrease. This ensures the possibility for more interaction between the solid and the solvent, increasing the dissolution rate.

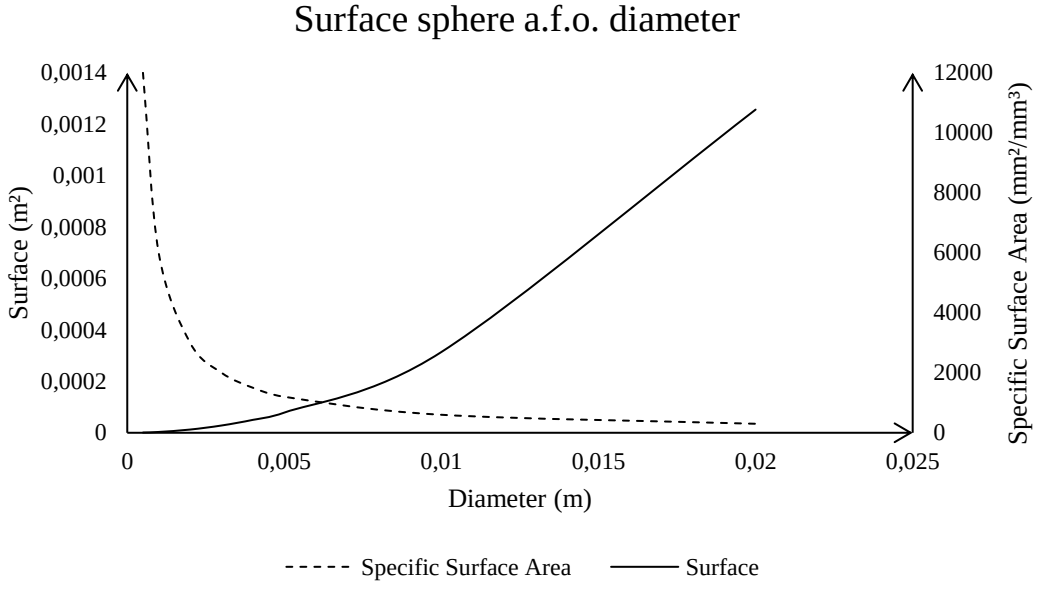

Figure 6 - Specific Surface Area a.f.o. diameter

2.3.2 HSWM – Rotor-stator principle

Increasing the specific surface area (SSA) of API's traditionally happens due to decrease in particle size. Therefore, traditionally dry mill units are used due to their scalability, broad availability and ability to deliver small particles. Unfortunately, dry milling may promote the deformation of the crystal lattice, induce crystal form conversion or loss of crystallinity and, if highly active compounds are milled, dry milling increases the chance of exposure, hence extensive environmental control is necessary [28]. Because wet milling mitigates some of the risks coming along with dry milling, it is relatively frequent used in the pharmaceutical industry [28]. Nevertheless, the mechanism of action still is indistinct and the influence of process parameters, such as concentration, temperature, solid loading…, is still unknown. IKA, leader in the world market in most of the product groups [29], determined the highly important and less important parameters on the final particle size, as illustrated in Table 1. Unfortunately, these assumptions have not been confirmed. [28], [30]

Table 1 - Influence of different parameters on final particle size according to IKA [31]

Minor Influence	Major Influence
Slurry concentration	Shear frequency
Shear gap	Number of turnovers
Flow rate	Crystal lattice strength
Initial particle shape	Tool configuration
Initial particle size	Tip-speed

High-shear wet mill devices work based on the rotor-stator principle. The rotors are connected to a rotating shaft, situated inside the working stage of the high shear mill, illustrated in Figure 63 added in Appendix A – Technical drawing 2P-4M configuration HSWM. On top of each rotor, a matching stator is installed. The slurry is fed radially in the head of the high-shear mill, where it is pushed axially through the rotor and stator gaps. Due to the high velocity of the rotor and the small gaps, a high shear rate *(R_s [1/s])* will form, causing the crystals to break. This shear rate can be calculated with Equation (3), where *V_u ([m/s])* symbolizes the velocity of the rotor and *d_s ([m])* the distance between rotor and stator, as indicated with the small arrow in Figure 7. [31]

$$R_s = \frac{V_u}{d_s} \tag{3}$$

Figure 7 illustrates the working mechanism of the rotor-stator principle where the rotor rotates inside the stator. As the rotor spins with high speed, the rotor gaps frequently align with the stator gaps. If the solid particles flow through the aligned gaps, the rotors tooth will impact the particle, transferring energy to the particle causing it to break. Because there is a chance a particle will pass through the gaps without colliding with the rotor tooth, multiple turnovers are required. [28], [30], [32]–[34]

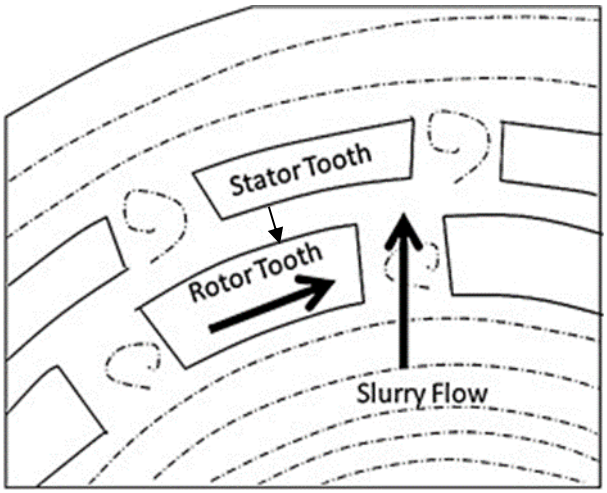

Figure 7 - Rotor-stator principle section

Previous studies have shown that introducing wet milling rotor-stator technologies avoid the common issues of dry milling units, which are briefly discussed above [30]. Wet milling units

can be applied in a continuous process, using a recycle loop and process analytical technology (PAT) to monitor the critical process parameters (CPP) during the milling [30].

2.3.3 Particle fracture

Fracture basically occurs above the stress or tensile strength of the material [35]. As shown in Figure 8A, the breakage of crystals depends on the size of the particles. As the particle size (share) decreases, the input energy, necessary to further break the particle, substantially increases [36]. Typically, this behavior is described using two stages: 'mass fracture' and 'attrition', illustrated in Figure 8B. Next to the particle size, several parameters influence the fracture of crystals (e.g. elasticity, hardness…) [37].

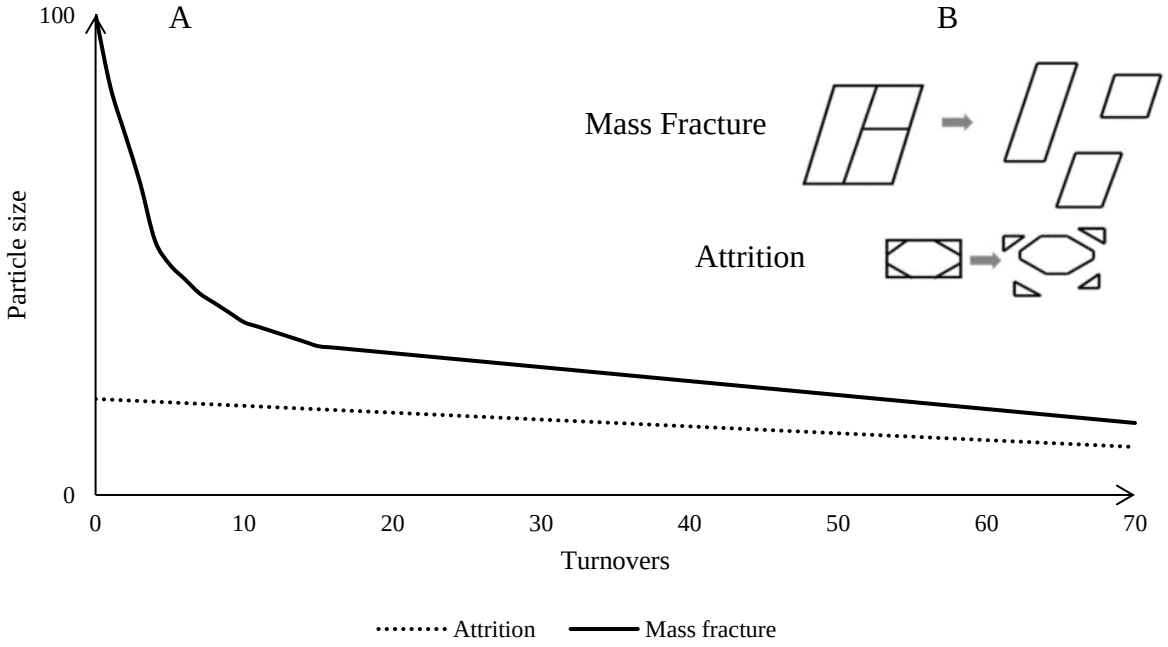

Figure 8 - A) Mass fracture, attrition a.f.o. particle size; B) Principle mass fracture, attrition [32]

Assuming that the mass fracture mainly happens at the point of highest energy, which Engstrom et al. determined to be at the point of contact between the rotor tooth and the fluid, particle-particle breakage, particle-wall breakage and fluid forces are considered negligible during the mass fracture [32].

To determine the influence of particle-particle, particle-wall and particle-probe interactions, Kim et al. did experiments with respectively different solid loading, a membrane between the wall of the reactor and the slurry; and a membrane between the probe and the slurry [38]. These experiments were carried out during sonofragementation of ionic crystals, but confirm the assumptions of Engstrom et al. that fracture happens at the point of highest energy. [32], [38]

2.3.3.1 Solid properties

Researchers at the University of Maryland have tested the influence of hardness and elasticity of a particle on the size reduction due to milling. Therefore, they introduced the Brittleness Index (BI). The BI is related to the elasticity (E), hardness (H) and fracture toughness (K_c).

These parameters are unique for every substance and can be determined through nanoindentation, where a small hard tip is pressed into the crystal with a specific maximum loading force (F) to create a puncture with a specific dept or displacement (h), diagonal length (a) and crack size (c). The loading force and the dept or displacement are continuously monitored. Figure 9 illustrates the dimensions of the puncture and the monitored parameters.

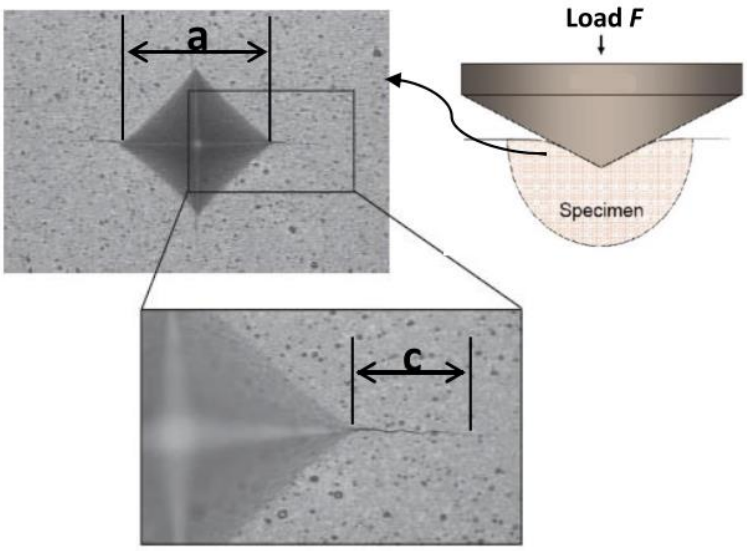

Figure 9 - Nanoindentation schematic [37]

The elasticity, or Young's modulus, is a mechanical property that expresses the stiffness in a numerical value (*[GPa]*). Traditionally, it is determined through the tensile test where E is estimated from the stress-strain response during the loading and unloading process of the tensile test [37]. The same principle applies during the nanoindentation, where the E is estimated from the stress-strain response during the loading and unloading of the tip.

The hardness of a substance is the resistance to plastic deformation, which can be described as a permanent change in shape due to a constant force. It can be calculated by dividing the applied force by the diagonal length of the indentation, as illustrated in Equation (4) [37].

$$H = \frac{F}{2a^2} \tag{4}$$

Next to the hardness and the elasticity, the fracture toughness plays an important role in the breaking mechanism. It can be described as the resistance to fracture, or the critical energy release rate per unit area of crack plane that is necessary for the crack propagation [39]. Ponton et al. reviewed and modified the fracture toughness calculation to a standard equation, illustrated in Equation (5) where ξ is a material independent calibration factor and c is the radial crack [40].

$$K_c = \xi \left(\frac{F}{c^{\frac{3}{2}}} \right) \tag{5}$$

Gahn and Mersmann assumed that deformation of crystals only takes place in the elastic stress field, which can be described as the applied stress that creates a recoverable change in shape, and due to this attrition is created. The assumption can be theoretically explained using

Rittinger's law, which states that a newly created surface caused by formation of a fragment is proportional to the elastic strain energy stored in the volume of the particle [41]. Based on this principle, a BI was developed, illustrated in Equation (*6*).

$$BI = \frac{H^{\frac{1}{2}}}{K_c^{\frac{3}{2}}} \tag{6}$$

Ghadiri and Zhang created a model that describes the attrition mechanism based on mainly plastic deformation. They noted that the impact on a particle causes a specific loading leading to significant plastic deformation followed by the formation of radial cracks and subsurface lateral cracks. When investigated further, the radial cracks turned out responsible for the mass fracture of a particle, while the lateral cracks propagate far enough into the body of the particle to create attrition. Like Gahn and Mersmann, Ghadiri and Zhang developed a BI based on the principle of plastic deformation, this BI is illustrated in Equation (*7*).[42]

$$BI = \frac{H}{K_c^2} \tag{7}$$

Gahn and Mersmann [43]; and Ghadiri and Zhang [42] already developed a Brittleness index, respectively based on the elastic – and plastic deformation mechanism. Because particle fracture consists of both, elastic - and plastic deformation, Ghaderzadeh and Calabrese developed a new principle including the elasticity [37]. As an impact of specific force hits a particle, the dent will have elastic deformation, that restores after the impact, and plastic deformation, that will remain. Based on this principle, a new BI, illustrated in Equation (*8*), is calculated. [37]

$$BI = \frac{H}{EK_c} \tag{8}$$

Furthermore, Ghaderzadeh and Calabrese compared the fracture between three components with different properties and thus different Brittleness Indices [37]. During the study, a silverson L4R rotor-stator mixer was used and the chord length distribution was measured using a Focused Beam Reflectance Measurement (FBRM), whereof the C10, C50 and C90 values can be verified. These values represent the particle chord length of which respectively 10, 50 and 90 percent of the total amount of measured particles are smaller. This is illustrated in Figure 10 with a perfect chord length distribution graph, in practice the clock curve will not be that perfect.

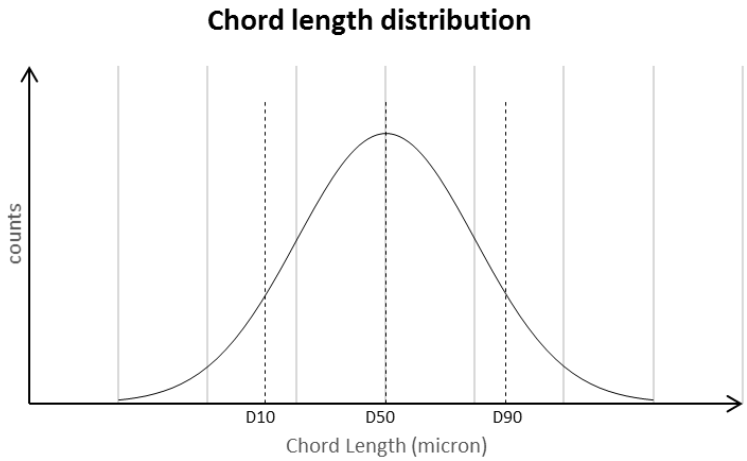

Figure 10 – Chord length distribution: C10, C50, C90

Different crystals with different properties, illustrated in Table 2, were milled using a HSWM. For each of these materials the BI is calculated for each of the above discussed principles. For each calculation, the BI sequence, from high to low, differs. Nevertheless, all theories are discussed to, if Ghalderzadeh's theory does not suffice, compare with the results to decide whether another principle is more sufficient. To validate the experiences of Ghaderzadeh and Calabrese, experiments with the same solids and one other solid, sodium chloride, are carried out.

What stands out is that with a higher BI, calculated according to Ghaderzadeh and Calabrese Equation (*8*), a lower C90 will be achieved. Nonetheless, the C10 will be higher with a higher BI. On the basis of this observation, it was stated that a higher Brittleness Index goes hand in hand with an easier to break substance. Because the crystals are easier to break, more mass fracture and less attrition (Figure 8B) will occur. This results in less miniscule attrition particles and more, larger mass fracture particles.

Table 2 - Material properties and BI [44]

	MATERIAL PROPERTIES			BRITTLENESS INDEX (BI)			C90	C10
	Elastic Modulus	Hardness	Fracture Toughness	Gahn and Mersmann	Ghadiri and Zhang	Ghaderzadeh and Calabrese	(micron)	
Crystal	E (GPa)	H (MPa)	K_c (MPa $m^{1/2}$)	$H^{1/2}/K_c^{3/2}$ (1/MPa $m^{11/4}$)	H/K_c^2 (1/MPa m)	H/EK_c (1/MPa $m^{1/2}$)		
Sucrose	21,15	1105	0,0971	$1,0 * 10^3$	$1,1 * 10^5$	0,54	31,3	10
Glycine	28,68	887,0	0,0894	$1,1 * 10^3$	$1,1 * 10^5$	0,34	62,5	3
Ascorbic Acid	32,27	1059	0,0695	$1,7 * 10^3$	$2,1 * 10^5$	0,47	37,5	11

2.3.3.2 Breakage model

During the particle breakage in a rotor-stator mixer, two opposite forces act on the crystal. The cohesive force creates a tendency to resist the separation of the particle, while the disruptive forces are responsible for the breakage of the particle. The disruptive forces ([N/m^2]) depends on the turbulence of the slurry. Due to a highly turbulent flow field, created by rotor-stator mixers, both macroscale turbulence and inertial subrange turbulence are present in the vessel. For macroscale turbulence, the disruptive force is proportional to the rotor tip-speed, while For the inertial subrange turbulence, the disruptive force is calculated via eddy fluctuations, which are flows running in opposite direction of the main flow which determine the speed of collision from the particles. The disruptive stresses are given in Table 3 Equation *(9), (10),* where ρ_p ([kg/m^3]) is the density of the compound, μ_{tip} is the tip-speed of the rotor ([m/s]), D is the diameter of the rotor ([m]) and x is the particle size ([m]).

Table 3 - Disruptive forces

Model	Macroscale Turbulence (MT)	Inertial Subrange Turbulence (IST)
Colission speed	~tip – speed	~Eddy velocity(x)
Disruptive force (τ_d)	$\rho_p {\mu_{tip}}^2$ *(9)*	${}^2\rho_p {\mu_{tip}}^2 \left(\frac{x}{D}\right)^{\frac{2}{3}}$ *(10)*

The cohesive forces ([N/m^2]) can be estimated via the models briefly describe above. Therefore, calculations based on elastic-, plastic and elastic-plastic breaking mechanisms are made. Each model determines the impact on a particle according to their mechanism. For example Ghaderzadeh stated that the impact on a particle can be divided into the elastic deformation and the plastic deformation. From that the fractional loss during an impact is calculated. The deviation for all models can be found in Ghaldezadeh's thesis [45]. The actual formulas for the cohesive forces are given in Table 4 Equation *(11) - (13),* where K_c is the fracture toughness ([$N/m^{3/2}$]), H is the hardness ([Pa]) and E is the elasticity ([N/m^2]).

Table 4 - Cohesive Forces

Model	Cohesive Force (τ_c)
Elastic Mechanism	$\frac{{K_c}^{\frac{3}{2}}}{H^{\frac{1}{2}} x^{\frac{3}{4}}}$ *(11)*
Plastic Mechanism	$\frac{{K_c}^2}{Hx}$ *(12)*
Elastic-Plastic Mechanism	$\frac{EK_c}{Hx^{\frac{1}{2}}}$ *(13)*

The breakage model, determined by Ghaderzadeh, now states that particles break if the disruptive forces exceed the cohesive forces. An equilibrium can be reached if the cohesive forces exceed the disruptive forces. Therefore, it is stated that the final size value after milling, should be the size at equilibrium and consequently, the disruptive forces and cohesive forces should be equal. Based on this principle, for each model, a correlation for the size as a function of the rotor speed and rotor diameter can be made. These correlations are given in Table 5 Equation *(14) - (19).* From these equations, a dimensionless numbers, called the Comminution number (Co), for solid fracture was derived.

Table 5 - Correlation maximum stable particle size

Plastic Mechanism	MT	$\frac{x}{D} \sim \frac{K_c^2}{\rho_p H D} \frac{1}{\mu_{tip}^3}$	*(14)*
	IST	$\frac{x}{D} \sim \left(\frac{K_c^2}{\rho_p H D}\right)^{\frac{3}{5}} \frac{1}{\mu_{tip}^{6/5}} = (Co_P)^{-\frac{3}{5}}$	*(15)*
Elastic Mechanism	MT	$\frac{x}{D} \sim \left(\frac{K_c^{\frac{3}{2}}}{\rho_p H^{\frac{1}{2}} D^{\frac{3}{4}}}\right)^{\frac{4}{3}} \frac{1}{\mu_{tip}^{8/3}}$	*(16)*
	IST	$\frac{x}{D} \sim \left(\frac{K_c^{\frac{3}{2}}}{\rho_p H^{\frac{1}{2}} D^{\frac{3}{4}}}\right)^{\frac{12}{17}} \frac{1}{\mu_{tip}^{24/17}} = (Co_E)^{-\frac{12}{17}}$	*(17)*
Plastic-Elastic Mechanism	MT	$\frac{x}{D} \sim \left(\frac{E K_c}{\rho_p H D^{\frac{1}{2}}}\right)^2 \frac{1}{\mu_{tip}^2}$	*(18)*
	IST	$\frac{x}{D} \sim \left(\frac{E K_c}{\rho_p H D^{\frac{1}{2}}}\right)^{\frac{6}{7}} \frac{1}{\mu_{tip}^{12/7}} = (Co_{EP})^{-\frac{6}{7}}$	*(19)*

By constructing a logarithmic plot of the particle size-rotor diameter ratio (x/D) as a function of the reversed tip-speed, as illustrated in Figure 11, the slope of the linear corresponds with the exponent of the tip-speed. This slope, according to Ghaderzadeh's experiments, is 1.6, which approaches the slope predicted via the plastic-elastic IST model where the slope is approximately 1.7.

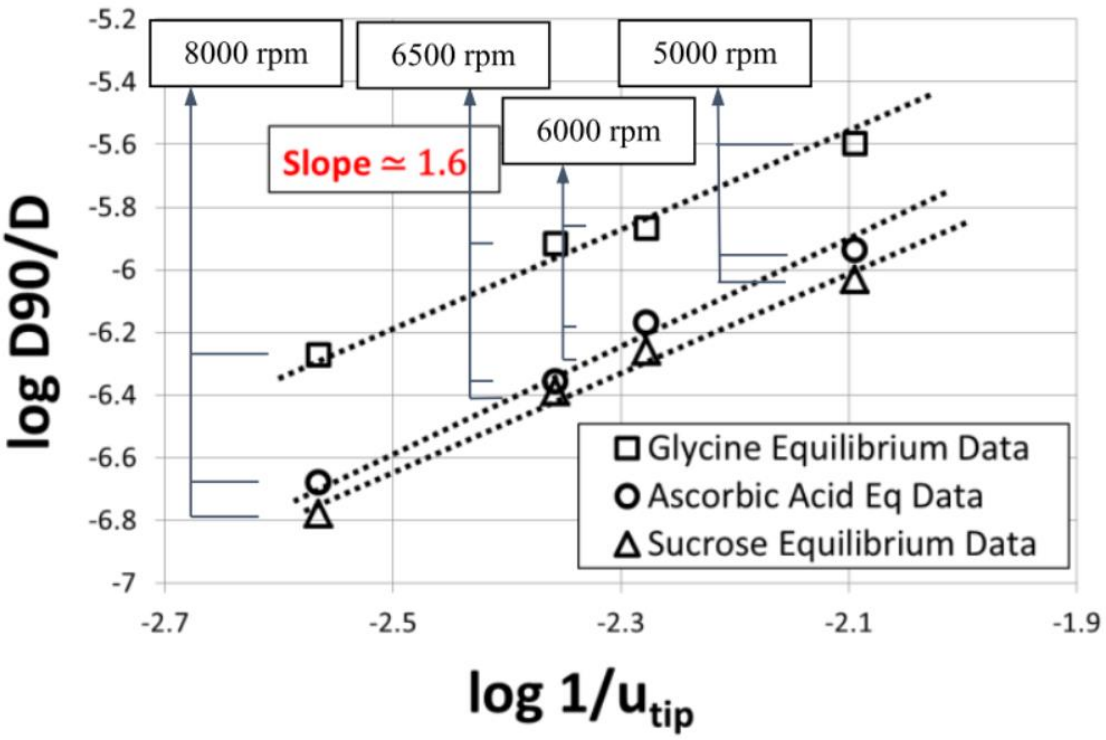

Figure 11 - Model validation according to Ghaderzadeh [45]

Models predicting a steeper slope, such as macroscale turbulence models, underestimate the energy required for the size reduction. It predicts a larger size reduction with the same amount of energy. Therefore, it was concluded that the breakage of particles in a rotor-stator mixer was particularly dependent on the IST. The reverse applies for the models predicting a milder slope. From the experiments was concluded that two slope predictions approached the actual slope, using the elastic mechanism of Gahn and Mersmann [43], predicting a slope of approximately 1.4, and the elastic-plastic mechanism, established during the research, predicting a slope of approximately 1,7.

Furthermore, the plot of the C90/D of all substances against the comminution number is created to confirm the breakage model. This is done for each IST model, after which the goodness off the fit is validated through the R^2 value, which represent the linear correlations between the data and the fit and needs to be as close to 1 as possible, and the root-mean-square error (RMSE), which represents the difference between measured and predicted value and, therefore, needs to be minimized. These data is given in Table 6.

Table 6 - Goodness fit Ghaderzadeh

Model	Goodness of fit
Plastic mechanism	$R^2 = 0.63$ $RMSE = 4.6 * 10^{-4}$
Elastic Mechanism	$R^2 = 0.60$ $RMSE = 5.0 * 10^{-4}$
Elastic-plastic Mechanism	$R^2 = 0.91$ $RMSE = 1.7 * 10^{-7}$

Again the elastic-plastic model achieves the best fit with the highest R^2 and the lowest RMSE, while the elastic model from Ghan completely deviates. This plot, illustrated in Figure 12, gives a material dependent trend to predict the C90 value of a compound with specific properties (H, E and K_c) with a specific rotor diameter in a specific mill.

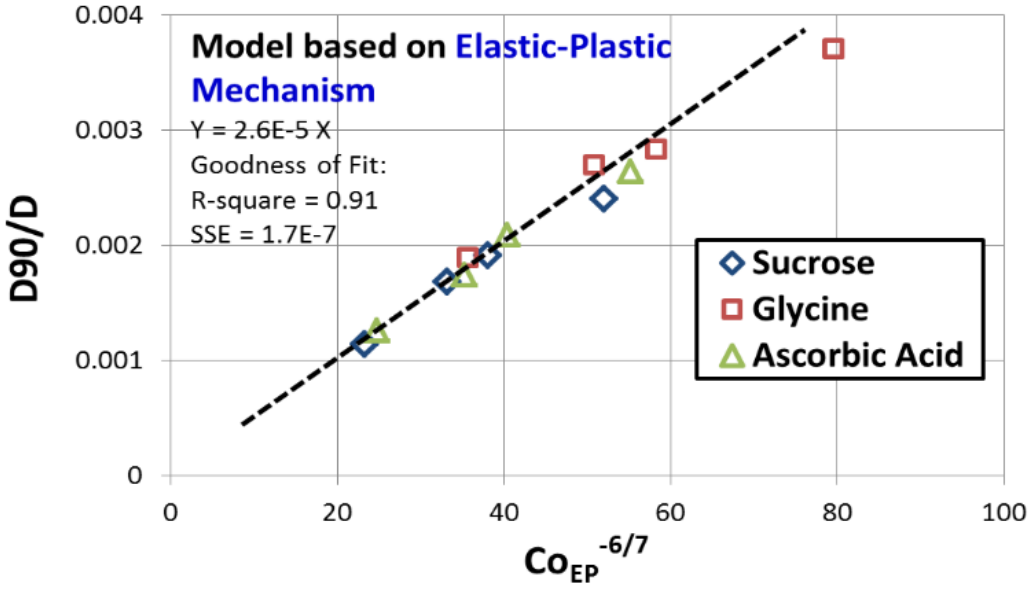

Figure 12 - Comminution number plot – Ghaderzadeh [45]

It has to be noted that Ghaderzadeh states that the geometry of the mill and therefore the energy dissipation, is different between mills. Therefore, the model is not able to predict the breakage of particles by other mills with various geometries. However, a comparison could possibly be made based on the energy dissipation rates of the mills.

2.4 SCALE-UP METHODE

Scale-up for high-shear wet milling is a common problem within the pharmaceutical sector. Currently a few methods, based on normalized energy [32], geometrical differences in the mill [34], tip-speed…[46], [47] have been developed. Unfortunately, further development and validation of the methods is necessary. Although some scale-ups were successful, it was only confirmed for a few compounds, independent of the properties of the compounds. Transfer of these scale-up approaches to other compounds with totally different properties (e.g. BI) is still unknown.

2.4.1 TIP-SPEED

Traditionally, HSWM are scaled-up based on an equal tip-speed of the rotor across all scales. Since the highest shear is achieved each time the rotor and stator teeth meet [47], the breakage model is determined based on the rotational speed of the rotor and the amount of teeth the rotor and stator own. As the rotational speed, or the tip-speed, from the rotor increases, the number of encounters between the rotor and stator teeth increases proportionally. Therefore, Lee stated that to scale-up a process, the encounters between rotor and stator, called the shear frequency, on lab scale and production scale should remain the same. Because the rotor and stator sizes over the various scales differ, the tip-speed can remain the same via manipulation of the rotational speed of the rotor. This scale-up method is mostly used as a basis for other scale-up methods.

2.4.2 NORMALIZED ENERGY

Engstrom et al. introduced a new scaling approach for the particle size reduction of a specific compound in a specific solvent using a high-shear wet mill based on normalized energy. This method is an expansion of the tip-speed method, discussed above.

The normalized energy (E*) is a calculation, made relative to a reference experiment and can be calculated using Equation (*20*). The reference experiment is carried out with one coarse generator, a tip-speed of 11,0 m/s, 40 turnovers and a flowrate of 0.43 L/min.

$$E^* = \varphi_r \cdot E_r \tag{20}$$

$$E_r = \frac{v^2}{v_b^2} \tag{21}$$

$$\varphi_r = \frac{NR_0 \cdot NS_0 \cdot \omega}{NR_{0b} \cdot NS_{0b} \cdot \omega_b} \cdot \frac{TO \cdot \frac{G}{\dot{Q}}}{TO_b \cdot \frac{G_b}{\dot{Q}_b}} \cdot \frac{H \cdot W}{H_b \cdot W_b} \tag{22}$$

The velocity (*v [m/s]*) of the rotor tooth depends on the angular speed of the rotor (*w [rad/s]*). During the energy calculation, only the number of outer row rotor (*NR*) and stator (*NS*) teeth will be taken into account because it is assumed that the other rows have a negligible impact. Hence, as the inner rows each have a smaller diameter, corresponding to a lower velocity at the same angular speed, the dissipation energy is reduced. The number of turnovers (*TO*) combined

with the number of generators (G), which are the rotor-stator combinations, and the flow rate ($\dot{Q}$) gives the relative residence time. Combining the height (H) and width (W) of the rotor teeth, gives the area of impact. The subscript b refers to the reference experiment.

The normalized energy, whereof the calculation is given in Equation (*20*) - (*22*), is calculated for each experiment and, on logarithmic scale, plotted against the mean square weight particle size, measured using FBRM software. The mean square weight particle size is the average of all measured, squared chord lengths in the vessel. This is illustrated in Figure 13. For the used compound, the logarithmic correlation of particle size versus the energy input was sufficient, achieving a R^2 value of 0.90. Nevertheless, it is not expected for all compounds to correlate this way due to the influence of solid properties and their fracture mechanism [35]. Therefore this method, using the normalized energy for scale-up, in combination with understanding the fracture mechanism of a given compound can serve as an initial platform to improve the scalability of particle size reduction using HSWM. [32]

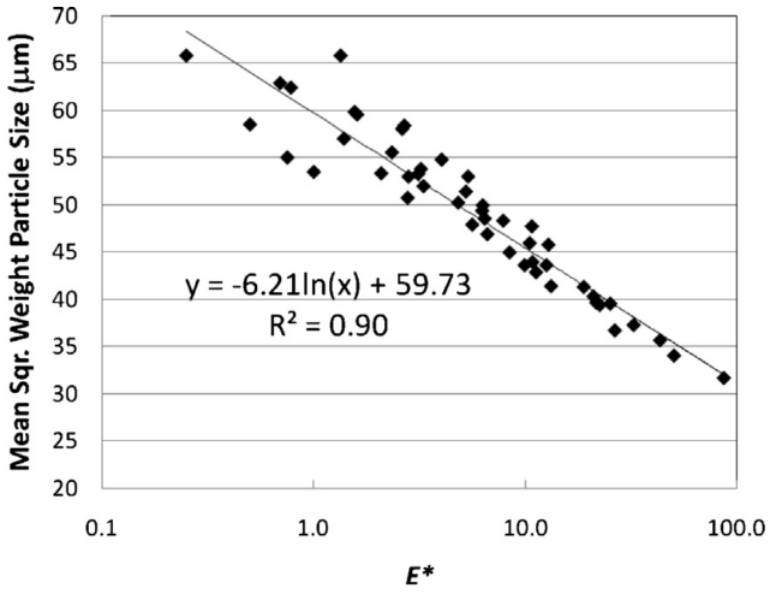

Figure 13 - Mean square weight particle size as a function of the normalized energy [32]

The trend above suggests that the particle size approaches a linear relationship with the normalized energy (E*). Notable is the scattering at lower E*, probably due to the decreasing difficulty in size reduction as the particles are larger. As the energy level increases, the particles become smaller and subsequently need even more energy to break again. As the breakage of a larger particle is easier, it is possible that too much energy is immediately added for the breakage, while this was already possible with less energy. Therefore, a scatter will be created. If, for example, a large particle is broken several times, the first time the particle is large with multiple weak points and easy to break, as the particle becomes smaller, there will be less weak points and the fracture will need more energy to find the weakest point, which is always stronger than the previous weak points. The same principle applies with the fracture of crystals during wet milling.

2.4.3 GEOMETRICAL DIFFERENCES IN THE MILL

Harter et al. experimentally tested the efficiency of the tip-speed scale up method, discussed above. Therefore, experiments on lab, pilot, and production scale were carried out at a tip-speed of 17 m/s, as illustrated in Figure 14.

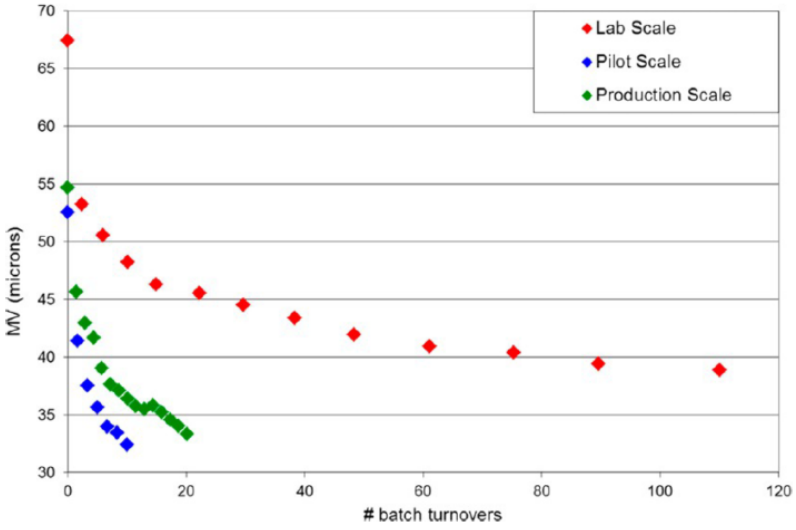

Figure 14 - Particle size i.f.o. number of batch turnovers: different scales; tip-speed 17 m/s [34]

The y-axis symbolizes the particle size as the volumetric mean of the particle size distribution (MV), which is the average of the volumetric distribution of the particles. The volumetric distribution can be interpreted as illustrated in Figure 15, where the bigger particles also occupy a larger volume.

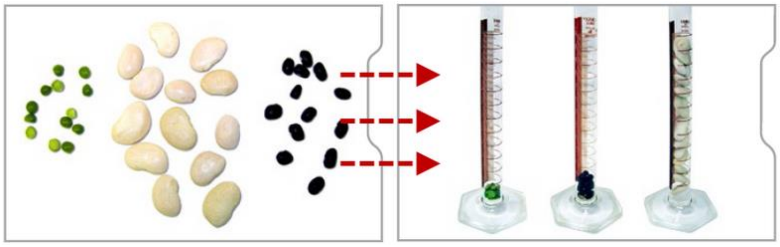

Figure 15 - Number distribution to volumetric distribution

Although all experiments were carried out using the same batch, it has to be noted that the starting particle size differs over the three scales (53 µm – 55 µm – 67 µm). One batch was created and subdivided into three shares. As only one milling experiment could be carried out at once, each share had different mixing times. As the mixing time increases, the particle size will be reduced due to shear effects from the agitator. These differences are thought to be insignificant because the shear, created by the agitator, is negligible in comparison to the shear obtained by the mill [34].

The influence of the starting particle size, slurry concentration and flow rate, which is manipulated using a pump, is illustrated in Figure 16. Each graph illustrated the evolution of the particle size, expressed as the volumetric mean, in function of the batch turnovers. As the flow rate increases, the residence time of a single particle in the mill will decrease, therefore the particle size reduction will progress slower. Besides the flowrate, the influence of starting

size is determined negligible, the progress of the larger starting size appears to have a larger slope in the early breakage region which is reasonable because the breakage of larger particles is easier than the breakage of smaller particles. Although this cannot be confirmed without the exact data. Finally, the both slurry concentrations appear to behave the same way over the whole milling process. The negligible differences in final particle size, created by these properties, are too small to explain the discrepancies observed between the different scales, illustrated in Figure 14.

Therefore, to explain the obvious inequality over the various scales, the focus is shifted to the geometrical design of the mill [34]. The importance of the geometrical component to scale-up was already stroke by Engstrom as he imported the size of the rotor tooth in Equation (*7*).

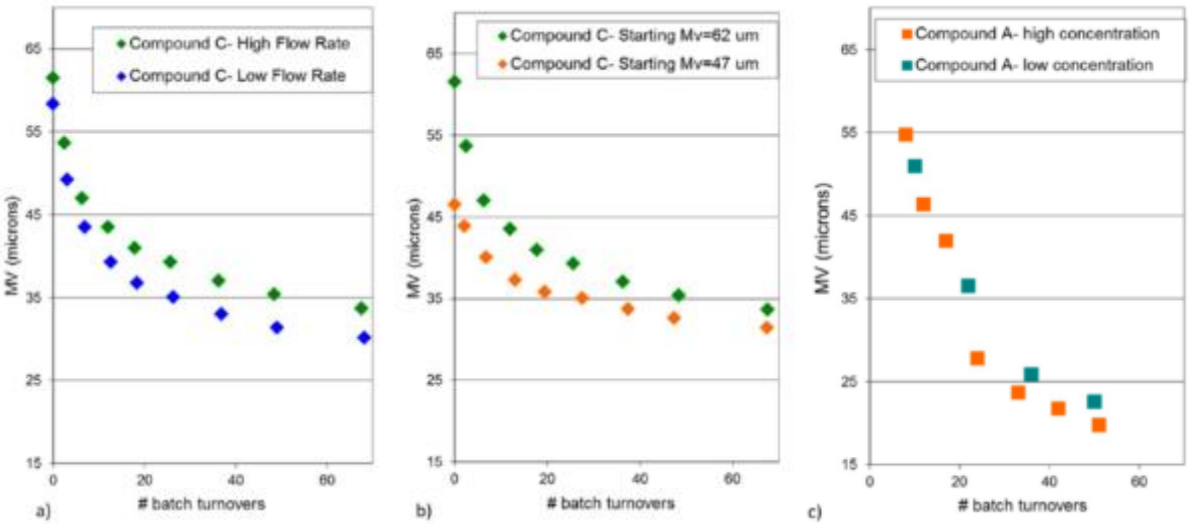

Figure 16 - Influence A) flow rate; B) starting particle size; C) solid loading on endpoint [34]

From all the possible dimensions of the high-shear rotor-stator mill, six were determined to be crucial due to their impact on the maximum shear stress and hydrodynamics. These six dimensions are illustrated in Figure 17. First of all, the number of slots is an important dimension because it increases the possibility of collisions between particles with the rotor teeth. The height, thickness and width of the slots influence the area of collision. Increasing this area also increases the possibility of collision between the teeth and particles. The last two dimensions are the horizontal and vertical gap between the rotor and stator. [34]

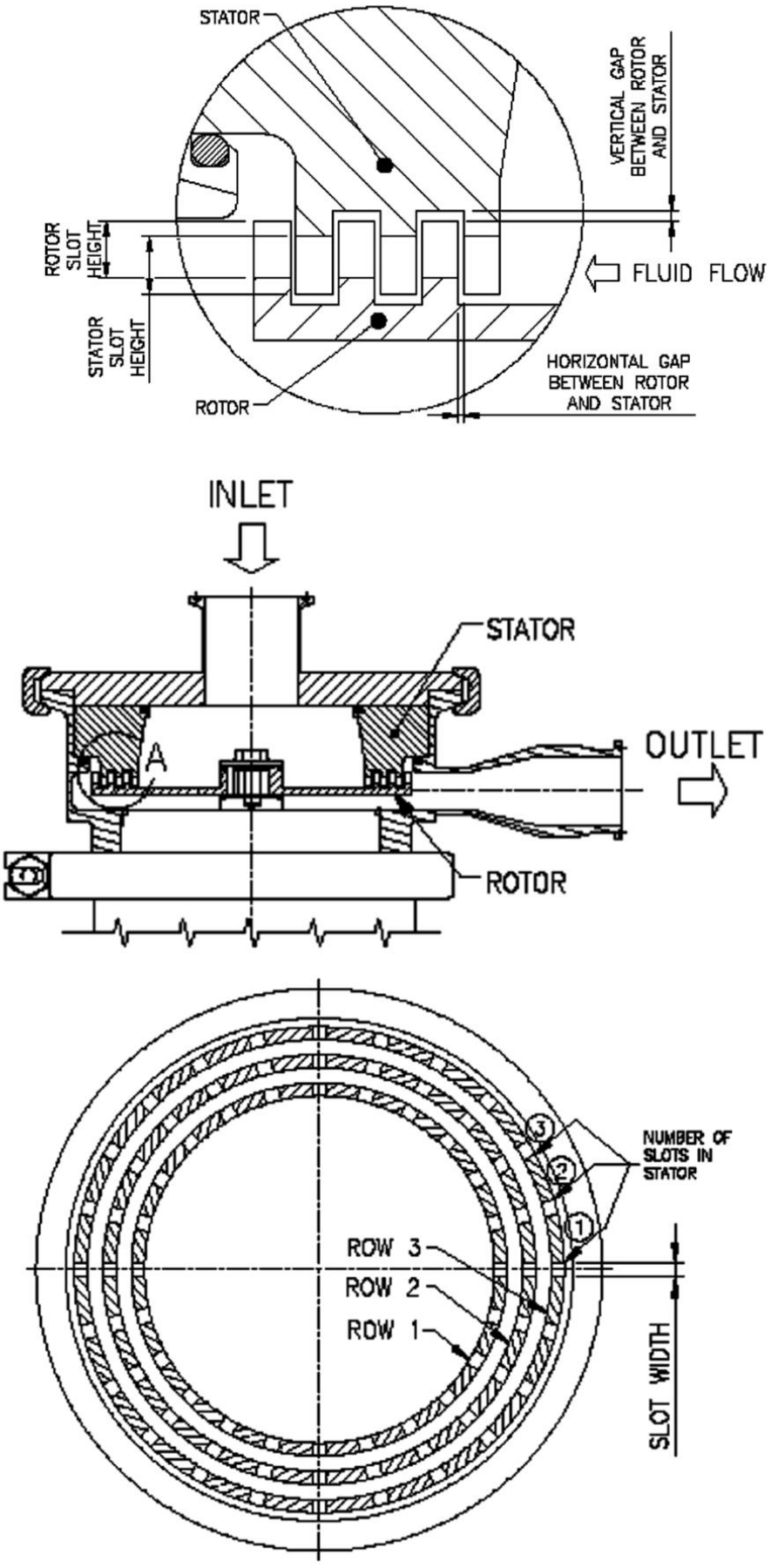

Figure 17 - HSWM dimensions [34]

Since several researches show the highest shear stress exists within the slots of the rotor and stator, attention was focused on the potential impact of the teeth on the particles [34], [48], [49]. Therefore, a Slot Event Model is introduced, where the slots of the rotor are responsible for the breakage of the particles. In contrast to the assumption of Engstrom that only the outer row is responsible for breakage, Harter et al. took all rotor teeth into account. Based on the frequency, Equation (*23*), and the probability, Equation (*24*), of a slot event, the follow equation, Equation (*25*), is composed.

$$Frequency = T \cdot RS \tag{23}$$

$$Probability = \frac{H \cdot W \cdot RS}{(H \cdot W \cdot RS) + (D \cdot \pi \cdot VG)} \tag{24}$$

$$Number\ of\ slot\ events = (T \cdot RS) \cdot \left(\frac{H \cdot W \cdot RS}{(H \cdot W \cdot RS) + (D \cdot \pi \cdot VG)}\right) \tag{25}$$

$T = \ number\ of\ batch\ turnovers$

$RS = \ number\ of\ rotor\ slots$

$H = height\ of\ rotor\ slot$

$W = width\ of\ rotor\ slot$

$D = diameter\ of\ outside\ row\ of\ rotor\ teeth$

$VG = vertical\ gap$

Scale-up, based on number of slot events, is possible if the geometry of the larger scale mill is known. This scale-up was successfully done for three different compounds, converting lab scale in to pilot scale based on the slot event calculation as shown in Equation (*26*) and illustrated in Figure 18.

$$T_{pilot} = \frac{T_{labo} \cdot RS_{labo} \cdot probability_{labo}}{RS_{pilot} \cdot probability_{pilot}} \tag{26}$$

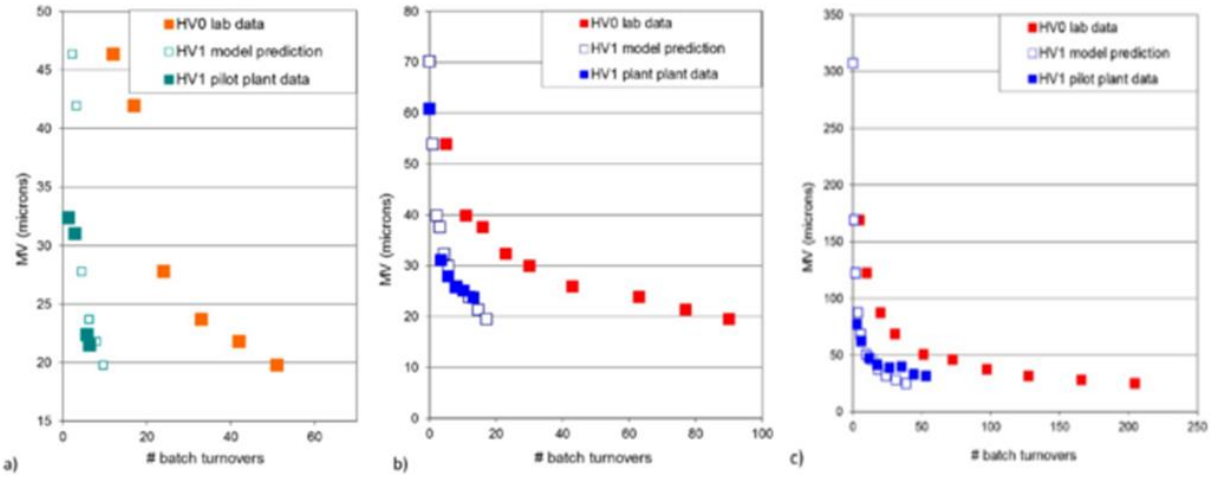

Figure 18 – Scale-up lab scale to pilot scale A) compound A; B) compound B; C) Aspirin [34]

Despite the successful scale-up from lab scale to pilot scale, this method doesn't take the influence of starting size, morphology, solid loading and BI… into account, assuming this influence to be negligible. This assumption will therefore be studied during this thesis. On top of that, scale up to production scales has not yet been confirmed.

3 MATERIALS AND METHODS

Materials and methods handles the experimental procedures performed during the experiments, as well as the working process and specifications of the used on-line and off-line measurement tools.

3.1 EXPERIMENTAL PROCEDURE

3.1.1 Set-up

Traditionally, during the lab scale experiments, the slurry is sucked out of the vessel from above and flowed back in from above, but below the surface to prevent splashing of crystals against the wall and to reduce air supply. During suction from above, the effect of segregation, which is the separation between particles due to their size, density, volume, shape…, is a possibility. In this case, the same compound, consequently the same density, could segregate due to the size of the crystal. Larger crystals could segregate to the bottom of the vessel, while smaller particles could float at the top of the vessel. If the suction happens from above, there could be a possibility that the larger, heavier particles remain on the bottom of the vessel, preventing them to go through the mill. This is illustrated in Figure 19. As the tubing of the suction does not reach the bottom of the reactor, the bottom of the vessel can be filled with the large particles.

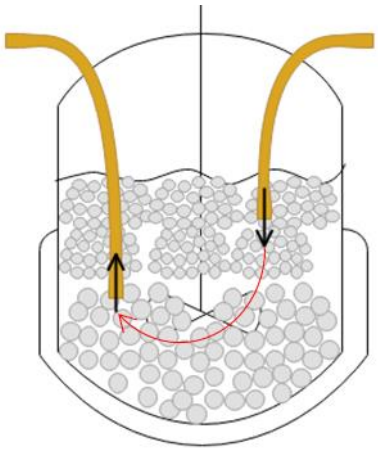

Figure 19 – Segregation

To avoid the effect off segregation as much as possible, the tubing of the suction and the flowback are put on opposite sides of the reactor and on a different height inside the reactor. The reactor is surrounded with a double wall filled with thermal oil, creating the opportunity to control the temperature inside the vessel. Around the HSWM, a cooling water flow can also be connected to decrease the rising temperature due to the high shear inside the mill. To start up this procedure, the three-way valve, illustrated in Figure 20, is turned to the vacuum and the flowmeter. Using a finger, the top neck of the three-necked flask is shut to activate the vacuum, sucking the slurry through the HSWM. From the moment some slurry is through the HSWM, the valve is quickly returned in the position as it is now displayed in Figure 20. After the milling, the vacuum tube is replaced by a nitrogen tube, illustrated in red on Figure 20, and the tubes are purged using this nitrogen flow.

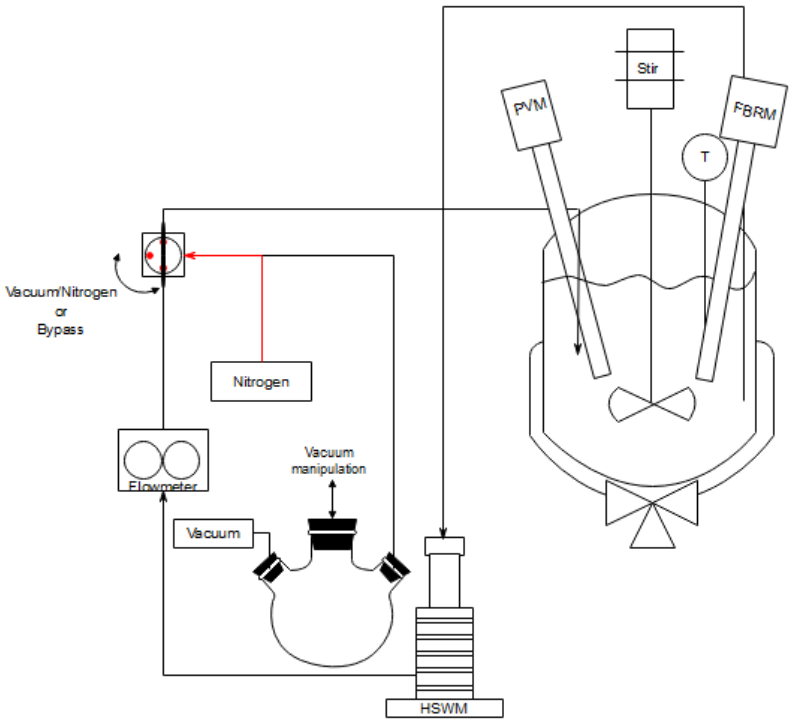

Figure 20 - Set-up suction from above

Despite the fact that lab scale works with suction from above, the production scale always works with suction from the bottom valve. Therefor, the set-up on productionscale is recreated on lab scale. Where the vacuum tubing is still connected, but accually should be unnesecairy. Using this set-up, the slurry should reach the HSWM due to gravitary, but to be sure the HSWM is not milling air, the vacuum tubing is nevertheless used during start up. The nitrogen purge is connected at the bottom valve off the vessel and used to purge the tubing after milling.

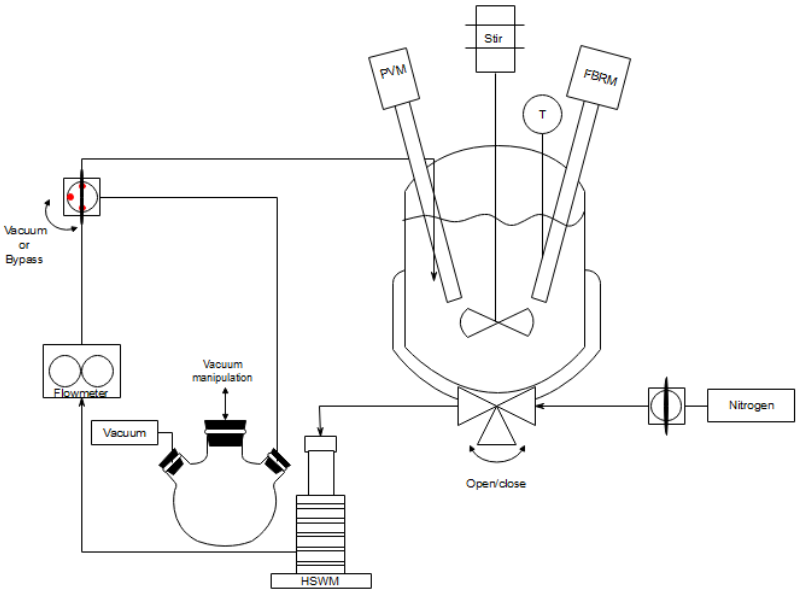

Figure 21 - Set-up suction from below

3.1.2 IKA High-Shear Wet Mill (HSWM)

IKA's magic LAB® High-Shear wet mill device, illustrated in Figure 22, is a small-scale mixing, dispersing and wet milling instrument. The in-line device is equipped with a single-stage dispersing module ULTRA-TURRAX® UTL. The slurry is radially fed through the inlet clamp, passes by the rotor and stator and finally leave the HSWM axially through the outlet clamp. On the operating unit, the rotations per minute (RPM) of the stator can be set between 7 000 RPM and 26 000 RPM in steps of 200 RPM. Next to the rotating speed, the torque of the motor, which is the power the motor needs to achieve the chosen RPM, can be read. [50]

Figure 22 - IKA's HSWM [50]

IKA's magic lab® works based on the rotor-stator principle, discussed in 2.3.2 HSWM – Rotor-stator principle. The rotors are connected to a rotating shaft, situated inside the working stage of the high shear mill. On top of each rotor, a matching stator is installed. A maximum of three rotors and stators can be used in several combinations. Figure 23 shows the different possibilities of rotor-stators of which three can be combined. The configuration of the mill always start with the top rotor-stator to the bottom rotor-stator, for example: a 2P-4M configuration consist of the 2P rotor-stator on top of the 4P rotor-stator.

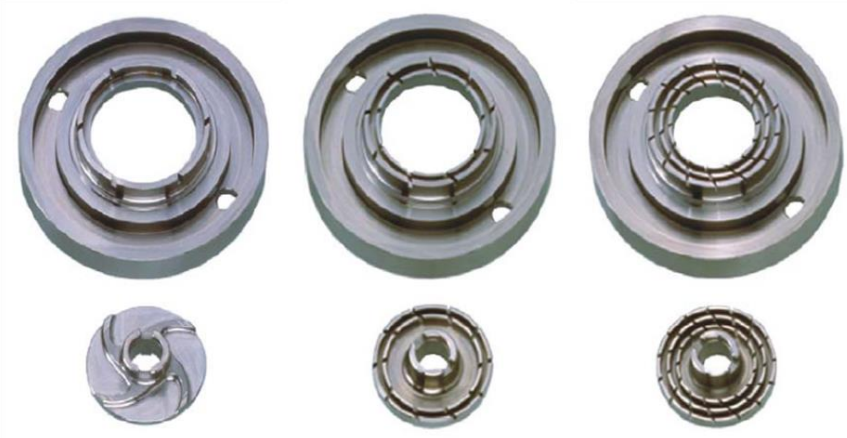

Figure 23 - Rotor-stators left to right: 2P, 4M, 6F

3.1.3 Preparation of the slurry

For each experiment the slurry is created inside the vessel. Throughout the experiments, four different solids were used, each with a different density, given in Table 7. Based on the densities (ρ *[kg/m³]*), the total volume of each batch is kept constant at a value of 1,56 L with a constant solid loading (*m/m%*) of 7m/m%. Therefore, Equation (27) is used. The slurry inside the vessel is kept at a temperature of around 25 °C (±5°C). The temperature effect on solubility is practically negligible since ethanol is an anti-solvent for all used compounds.

$$V_{total} = \frac{m_{Ethanol}}{\rho_{Ethanol}} + 0{,}07 \cdot \frac{m_{Ethanol}}{\rho_{substance}} \qquad (27)$$

An example calculation is made for the model compound, sucrose:

$$1{,}56\ L = \frac{m_{Ethanol}}{0.79\frac{g}{cm^3} \cdot \frac{1\ cm^3}{1000\ L}} + 0.07 \cdot \frac{m_{Ethanol}}{1.59\frac{g}{cm^3} \cdot \frac{1\ cm^3}{1000\ L}} => m_{Ethanol} = 1190\ g$$

$$m_{sucrose} = 83.3\ g$$

Table 7 - Density

Substance	Density (*[g/cm³]*)	Mass for 1,56 L 7m/m% slurry (*[g]*)
Sucrose	1.59	83.3
Ascorbic Acid	1.65	83.3
Glycine	1.61	83.3
Sodium Chloride	2.16	84.0
Ethanol	0.79	Sucrose, Ascorbic Acid, glycine: 1190 Sodium Chloride: 1200

Noted is that the masses of all the compounds, except for sodium chloride, are the same due to rounding of the values. For ethanol, two values are given which corresponds to respectively the mass ethanol necessary to create the sucrose, ascorbic acid and glycine 7m% slurry and the mass ethanol necessary to create the chloride 7m% slurry.

3.1.4 Sieving

A Retsch AS 200 sieving device, shown in Figure 24, is used to provide all substances the same starting size distribution (e.g. 250 µm – 450 µm). Using a vibration plate, stacked with sump tray and respectively a 250 µm mesh sieve and a 450 µm mesh sieve, the crystals are sieved. The fraction between the two sieves is kept for experiments and should have approximately the same starting distribution for each compound. Each batch was sieved for 20 minutes with an

interval of 10 seconds, a motion over both horizontal and vertical axes and an amplitude of 1.80 mm.

Figure 24 - Retsch AS 200

The starting particles after sieving are illustrated in …, where the sucrose particles are damaged due to the use of manual force to achieve the particle size.

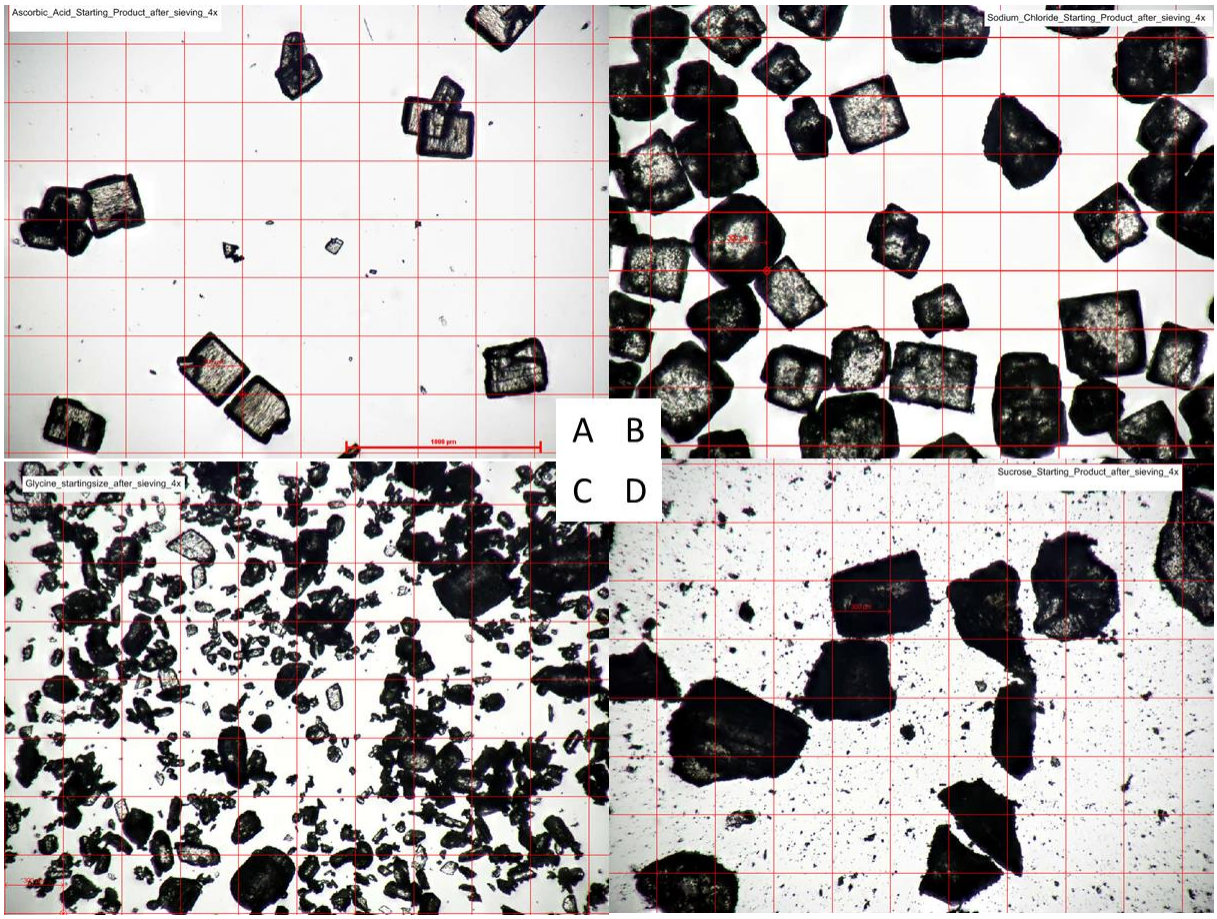

Figure 25 – After sieve: A) Ascorbic Acid: B) NaCl; C) Glycine; D) Sucrose; 4x magnification

3.2 CHARACTERIZATION EQUIPMENT

3.2.1 Focused Beam Reflectance Measurement (FBRM)

The particle size and counts are tracked using Mettler's FBRM. This Lasentec instrument features a probe that is directly inserted in the vessel, preferably under an angel to ensure that the particles can easily flow around the probe window. Through the probe, a laser beam is transmitted and focused at a point near the probe window. This laser beam spins at a fixed rotation speed, typically 2 m/s. Hereby, multiple particles at the probe window can be measured in short time.

Because the laser collides with the particles, the beam will be backscattered to the probe. These pulses of backscattered light are detected and, on basis of time, converted to a distance. This distance is described as the chord length of a particle, which is correlated with the actual particle size. Due to the multiple measurements in a brief amount of time, an accurate distribution of the chord lengths over time can be created. From these distributions, multiple statistical data, such as the fine counts, can be calculated. A visual representation of the chord length of a particle is given in Figure 26. Every 10 seconds, a measurement was saved. [51], [52]

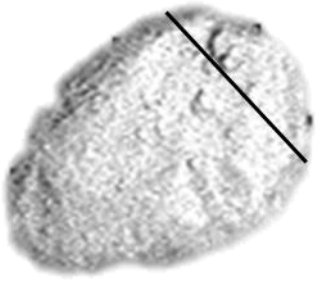

Figure 26 - Chord Length

The measurement data can be plotted in multiple weight types, illustrated in Table 8. Since the milling process mainly provides small particles, the no weight measurements are the most interesting during this study. These types are calculated via the Weighted Chord Distribution (WCD), represented in Equation *(28)* [53].

$$\mathrm{WCD} = \frac{M_i^x}{\sum_{i=1}^{k} n_i M_i^x} \qquad (28)$$

In this equation, the n_i represent the average counts of a particular channel, which is a size range, with M_i as the midpoint of that size range. The exponent x is varied to obtain the various weight types. A brief overview of these weight types, each with the specific exponent of x, is given in Table 8. It has to be noted that the no weighted measurements actually corresponds with the length weighted measurements because for a larger particle, the chance to measure multiple chord lengths increases [53].

Table 8 - Weight types FBRM

Measurement technique	x	Definition
No Weight	0	Chord Length, emphasizing small particles, raw data
Length Weight	1	The chord length's will be distributed according to the length of a particle.
Square Weight	2	Chord Length squared, emphasizing larger particles.
Cube Weight	3	Neglecting the really small particles

During this study, the no weighted and square weighted measurements will be used. The no weighted because during the milling, the small particles that are achieved are important, while after the milling it is important to know what happened with the larger particles, therefore the square weighted measurements will be used.

Figure 27 is a schematic representation of the structure of the FBRM probe. The chord length, measured by this instrument, correlates to the actual particle size. Unfortunately, a reconstruction of the actual particle size, starting from the chord length distribution of non-spherical particles, is no possibility yet.

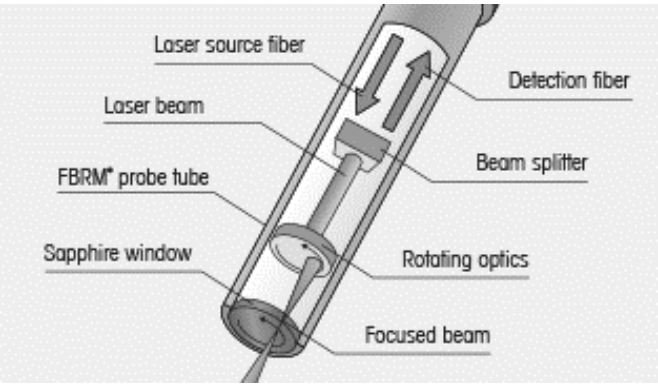

Figure 27 - Schematic FBRM probe [54]

3.2.2 Particle Vision and Measurement (PVM)

To gain in-line visualization of the particles, the Mettler PVM is used. This probe based video microscope is inserted directly in the vessel. The probe is equipped with a high resolution CCD camera and an internal illumination system [55]. On the basis of the taken images, the Relative Backscatter Index (RBI) is calculated. This property is related to the particle size and slurry concentration.

Figure 28 - PVM probe [55]

3.2.3 Scanning Electron Microscope (SEM)

The crystal size, shape and surface morphology are visualized using a Phenom Pro scanning electron microscope (SEM), illustrated in Figure 29A. Before the images were taken, the samples were coated with a gold layer and subjected to a fixed current of 30 mA for 2 minutes via a Quorum Q150R S sputter device, illustrated in Figure 29B, to make the samples conductive, increase the resolution and prevent movement of the sample.

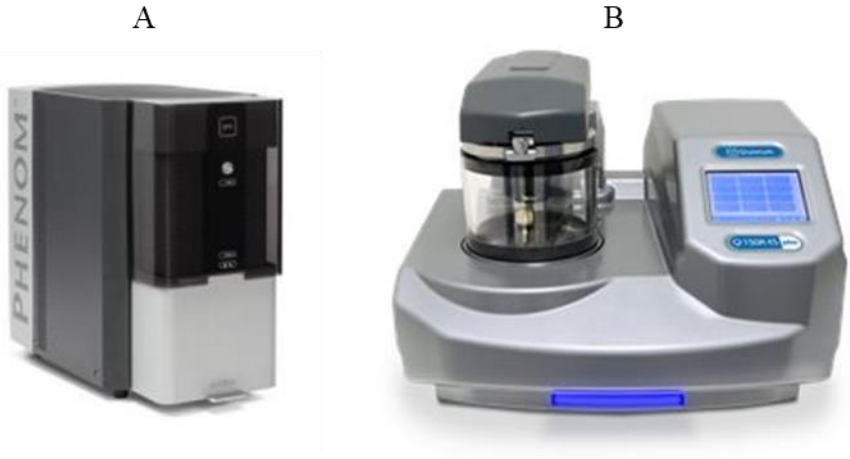

Figure 29 - A) Phenom Pro [56]*; B) Quorum Q150R S* [57]

Figure 30 illustrates the schematic working process of the SEM. To prevent the interference of air, SEM measurements always take place under high vacuum. The Electron gun creates an electron cluster, from primary electrons, that is launched at the sample at high speed. The cluster is focused and aligned using an electromagnetic field created by respectively the magnetic condenser- and objective lens. Hereby, the electrons will move over the sample surface in a two-dimensional grid. Once the electrons reach the surface of the sample, one of two possible outcomes happen: the primary electrons backscatter or the primary electrons bumps an electron from the sample, secondary electron, out of place. The backscattered electrons and secondary electrons are measured as an electric current. On the basis of the current strength and time related place of the electron beam, a visual off the sample surface is created.

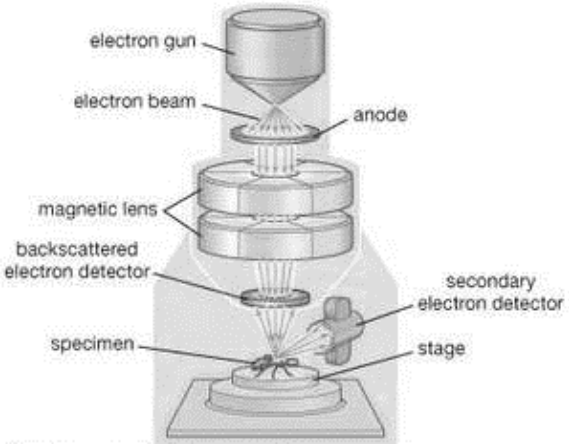

Figure 30 - Schematic SEM representation [58]

Figure 31 illustrates a result from a Phenom Pro SEM measurement of sucrose at a magnification of 300 times after coating with a Quorum Q150R S sputter device. The magnification can be adjusted.

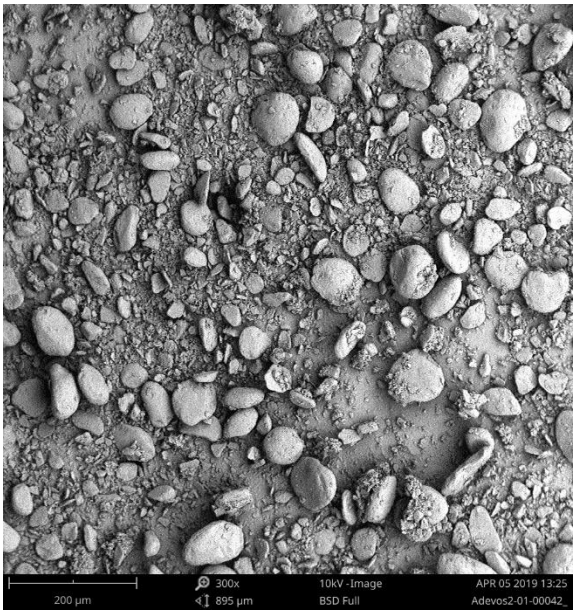

Figure 31 - SEM image sucrose after milling, 300x magnified

3.2.4 Malvern G3 Morphology

For the analysis of off-line samples, image analysis is used. Image analysis is the process of extracting data from images. Therefore, the Morphology G3 illustrated in Figure 32, provided by Malvern Instruments. The dry sample is dispersed via a dispersion clock on the glass plate. The right magnification is chosen via the software and the SOP is set to the desired settings. The Malvern now will measure the surface area of the particles on the glass plate and convert them to the diameter of an sphere with the same surface are as the particle.

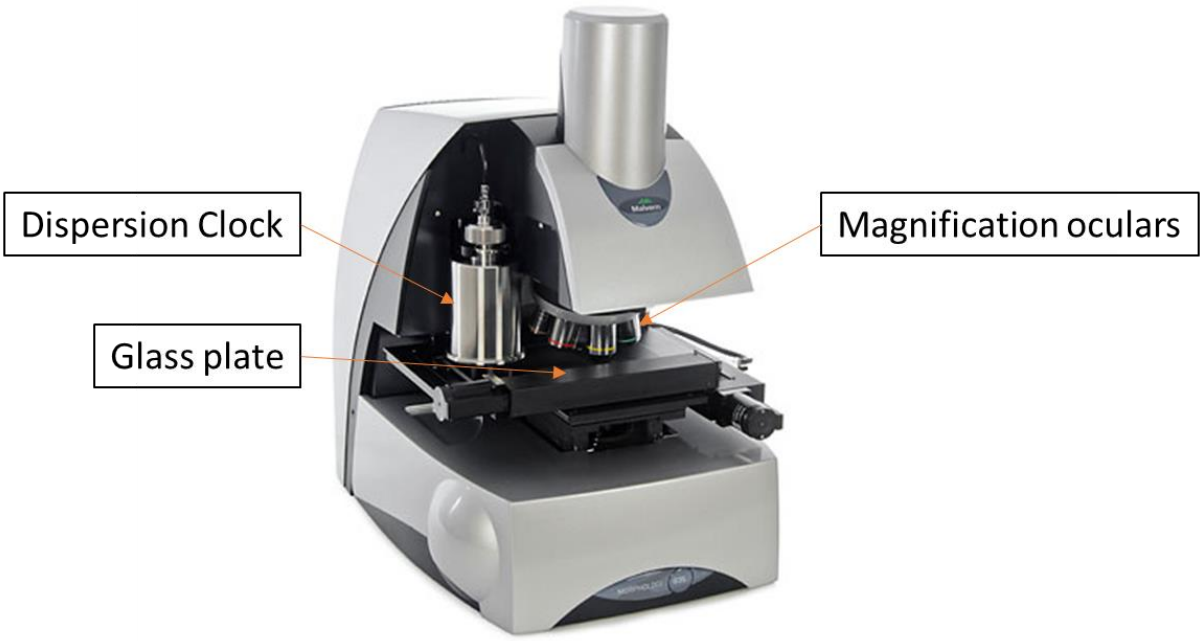

Figure 32 - Malvern Morphology G3

4 RESULTS AND DISCUSSION

4.1 SOLID PROPERTIES ON WET MILLING PROCESS

The traditional use of dry mills, especially in the pharmaceutical sector decreases die to the possibility of crystal lattice deformation, crystal form conversion or loss of crystallinity. Moreover, if highly active compounds are milled, dry milling increases the chance of exposure. As a result, the HSWM application recently made a strong rise. The shift from dry milling to wet milling also brings challenges. At the moment, the mechanism of action of the HSWM is still indistinct and a clear, robust scaling method is not developed yet. Therefore, this chapter will discuss the influence of various solid dependable process parameters (e.g. solid loading, starting size, BI) on the milling process. All experiments were carried out in duplicate, using suction from the bottom valve as discussed in the materials and methods section above.

4.1.1 Solid loading

Because breakage is energy related, it can occur due to shear effects, particle-particle collision and particle-wall collisions. Therefore, several experiments were carried out to explore the influence of the particle-particle collisions by milling slurries of sucrose in ethanol with different solid loading (e.g. 5 m%, 7 m% and 10m%).

An increase in solid loading entails an increase in the chance of particle-particle collisions and, possibly, particle-wall collisions. Although, due to a constant area of the wall and a larger amount of particles in the vessel, it is a possibility that the particles will obstruct one another and prevent collision with the wall surface. Therefore, it is not a certainty that an increase in solid loading will entail more particle-wall collisions. Based on this theory it is determined that an increase in solid loading will particularly affect the amount of particle-particle collisions. Therefore, it is reasoned that the variation over the experiments with different solid loading is due to the particle-particle collisions. The composition of the slurries is given in Table 9.

Table 9 - Slurry composition various solid loading

Slurry solid loading (*m/m%*)	Mass Ethanol (*g*)	Mass Sucrose (*g*)
Sucrose Slurry 5 m%	1201	60.1
Sucrose Slurry 7m%	1190	83.3
Sucrose Slurry 10m%	1173	117.3

For each slurry the total volume was kept constant as the solid loading changed. The slurry was milled using the IKA Magic Lab®, using the 2P-4M configuration at 18 000 RPM. The temperature was kept constant at 25°C (±5°C), with a rotating speed of the overhead stirrer of 500 RPM. During the milling process, it is important for all particles to reduce in size. To determine whether each particle is reduced in size, it would be ideal to track the largest particle size, being the C99, inside the vessel. Due to strong fluctuations in the measurements in the

C99, the C90 value will be tracked using FBRM software. The C90 and C99 represent the particle size whereof respectively 90% and 99% of all particles in de vessel are lower. Other values such as C50, C10, mean… were tracked as well, but show the same trend as the C90. These measurements are included in Appendix B – Additional solid loading measurements.

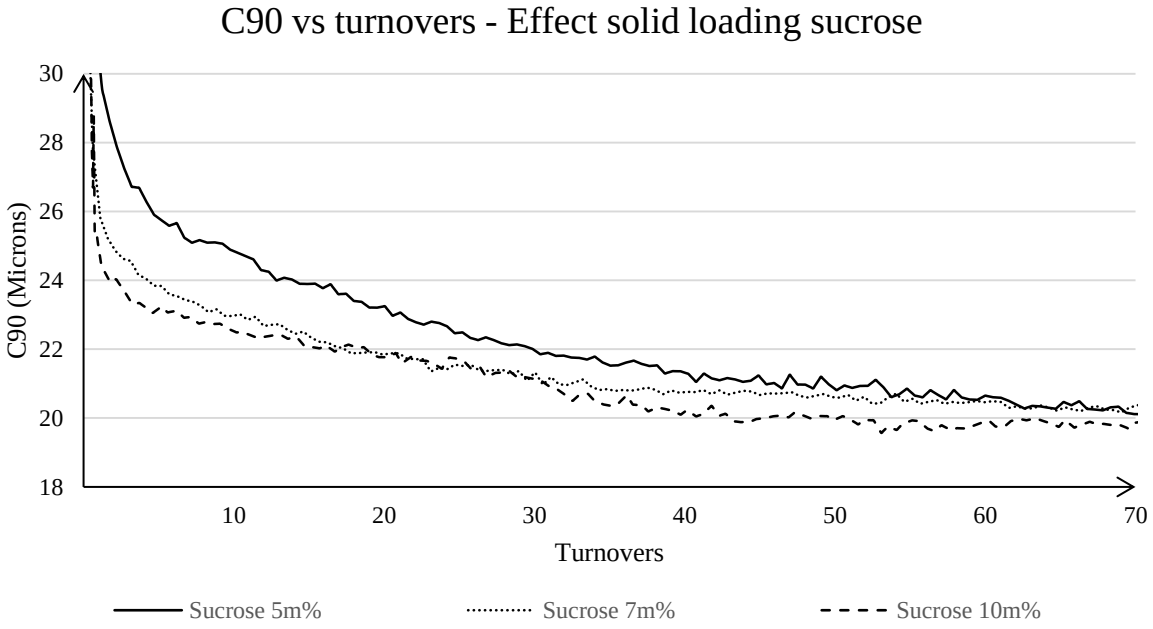

Figure 33 - C90 vs turnovers – effect Solid loading Sucrose

The results, illustrated with the C90 of the different experiments in Figure 33, suggest that the influence of the solid loading on the milling is rather small. After 70 turnovers the various slurries all approach the same minimum value of approximately 20 microns (±1 micron). As discussed in the literature study, the breaking mechanism of particles can simplistically be illustrated with two mechanisms: mass fracture and abrasion or attrition. Mass fracture mostly occurs on the larger particles and causes a fast decrease in particle size, while abrasion occurs on the smaller particles ensuring a more gradual decrease in particle size. Therefore, the mass fracture regime is determined by the first part of the curves illustrated in Figure 33. Notable is the development of the various curves, where the attrition regime of the curves are approximately parallel and the transition of the steep mass fracture regime to the more stagnating attrition regime occurs at a larger particle size as the solid loading decreases. The solid loading appears to influence particularly the fracture behavior of the milling process. This observation can be explained by the particle-particle interactions, which can be illustrated via two properties: frequency of collisions and the intensity of the collisions. As the solid loading increases, the number of particles inside the slurry increases proportionally. This increase in quantity, while the volume of the slurry remains constant, increases the probability of two particles to collide, which is described as the frequency of collision. Therefore, the mass fracture of the large particles will occur faster.

As the particles become smaller, the number of particles inside the vessel will keep increasing, consequently increasing the frequency of collision. Despite the constant increase in collision frequency, the endpoint of all experiments remain approximately the same. Due to a decrease in particle size, the mass of a particle will reduce proportionally because the constant density

of the crystal. As the mass of a particle decreases and the flowrate during the experiments remain constant, the kinetic energy of a particle will decrease as well. This theory is confirmed via Equation *(29)* where m illustrated the mass of the particle and v the velocity of the particle.

$$E_{kin} = \frac{1}{2}mv^2 \qquad (29)$$

Due to a lower kinetic energy of the particle, the collision will have a lower impact, described as the intensity of the collision. As it is described in the literature study that a smaller particle requires more energy to break, which is not gained from the lower intensity of collision. After a certain number of batch turnovers, all the slurries will approach approximately the same particle size, and consequently these particles will have roughly the same energy which will not cause any more breakage. Therefore, it is reasonable to conclude that only the intensity of the collision can influence the endpoint of the experiment, while the frequency of collision can only influence the breakage rate of the milling.

These observations are confirmed in the literature by Ghaderzadeh [45], who tested the milling of respectively 2m%, 5m%, 10m% and 15m% of sucrose in IPA using a silverson L4R. The slopes all increase proportional to the solid loading. Similarly, Harter et al. as well carried out two milling experiments at different solid loading, from which the specific concentration is unknown, and did not observe any difference in particle size reduction rate and equilibrium size [34].

Additionally, solid loading experiments were carried out for Ascorbic Acid at 7m% and 10m%, confirming this result with a difference in equilibrium size of approximately 2 µm, which can be explained by a standard deviation because the experiment was not duplicated. These measurements are added in Appendix B – Additional solid loading measurements.

4.1.2 Starting solid size

As suggested in the literature study, larger particles need less energy to break and have a higher probability to experience mass fracture. Therefore, two different starting sizes for sucrose have been tested. Next to the sucrose sieved to a mesh size between 250 µm and 450 µm, a sucrose slurry consisting of particles sieved to a mesh size between 450 µm and 1 mm have been proceeded. Because the available sucrose crystals were too big, the fraction between 250 µm and 450 µm was created by applying manual force to push the crystal through a 450 µm sieve. After milling, the substance is sieved. Nonetheless, very small particles are stuck on the larger particle surface and therefore, despite their small size, remain in the fraction between 250 µm and 450 µm. The difference in starting particle size is illustrated in Figure 34 captured by an optical microscope at a magnification of 4. The grid of the left image has a width of 500 µm, while the grid on the right image has a width of 100 µm.

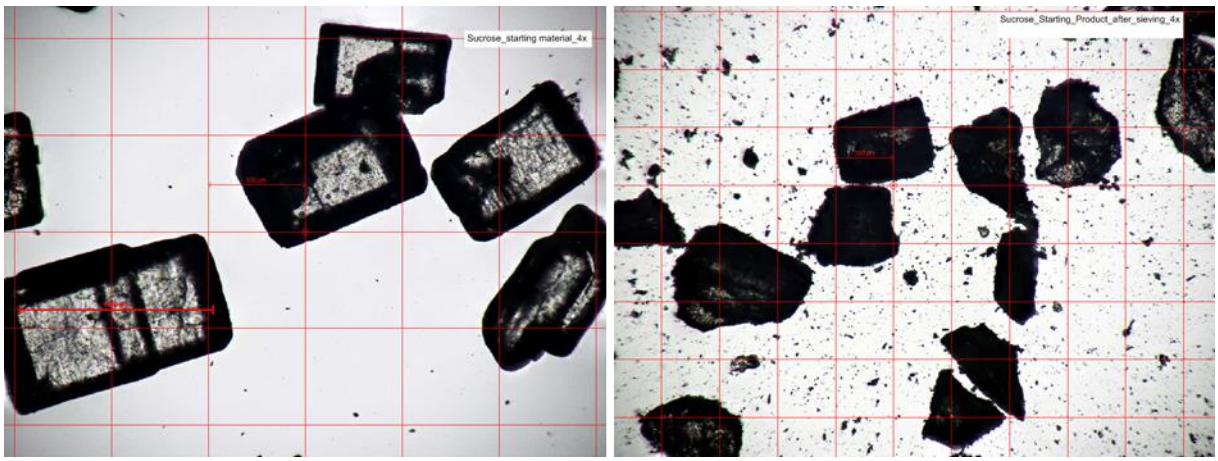

Figure 34 - Starting particle sucrose: left not sieved; right: sieved - 4x magnification

The experiments were carried out keeping all variables, apart from the starting particle size, constant. The volume was kept at 1.56 L with a solid loading of 7m%. Both slurries were milled with a 2P-4M configuration and a rotating speed of the rotor at 18 000 RPM. The stir was kept constant at a rotational speed of 500 RPM and the temperature inside the vessel was 25 °C (± 5°C). The development of the mean chord length, measured using FBRM software, is illustrated in Figure 35.

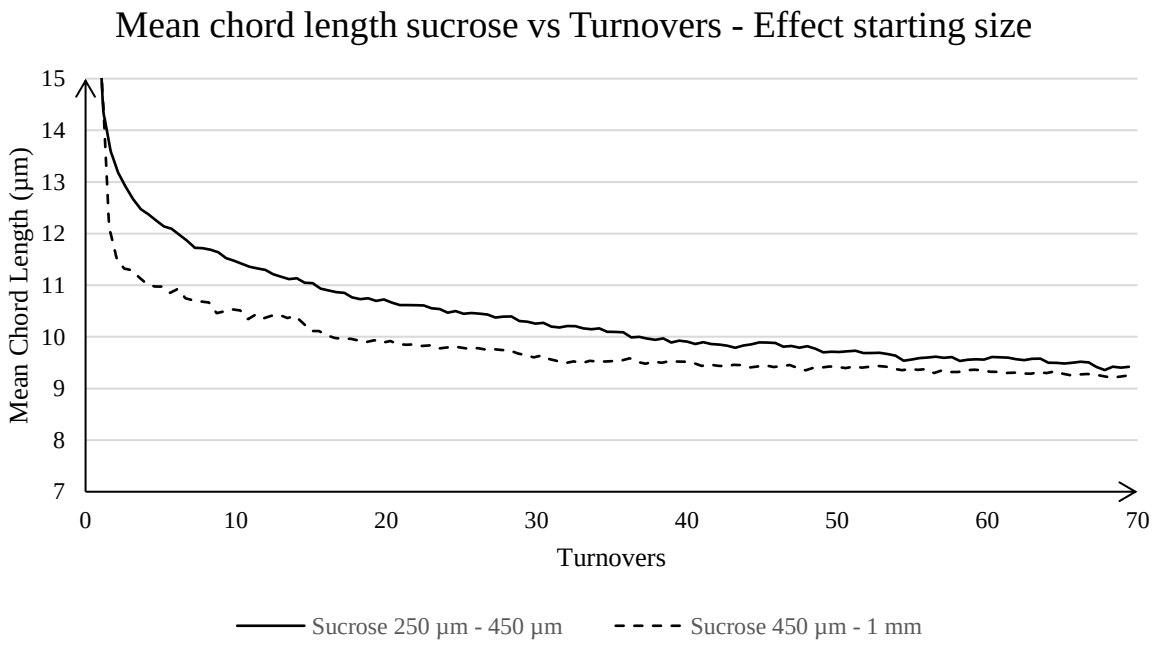

Figure 35 - Mean chord length versus turnovers - Effect starting size

Figure 35 shows the mean no weighted chord length distribution of the two slurries during the milling process as a function of the turnovers. Similar to the solid loading observations made above, the discrepancies between the two milling experiments is barely noticeable in the endpoints, which only differ approximately 0.2 µm. Again, this observation can be explained by the particle-particle collisions. As the solid loading, compound and total mass of the solid, consequently the volume, are kept constant, a larger starting particle size will result in less particles inside the vessel. This is substantiated by Equation *(30)* where m ([*kg*]) represent the

total mass of solids, ρ ([kg/m^3]) the density of the solid substance and $\bar{V}$ the average particle size.

$$Number\ of\ particles = \frac{\frac{m_{tot,solid}}{\rho_{solid}}}{\bar{V}_{particle}} \qquad (30)$$

Less particles causes a lower chance for particle-particle collisions to occur, consequently decreasing the collision frequency. Based on this theory, an increase in starting particle size would cause a more gradual curve. Nonetheless, the opposite occurs due to the intensity of the collisions. As the particle size increases, the mass of a particle with the same density will increase proportionally. Due to the increase of mass, the kinetic energy of a particle will increase, as suggested by Equation *(29)*. The increase in collision intensity will cause the breakage rate of large particles to increase, up to a certain point in the milling process where the particles are too small to create a collision intensity high enough to break. Therefore, the attrition regime will be reached faster with a larger starting particle size. Despite these differences, the influence of starting solid size on the particle size reduction via wet milling is negligible.

Harter et al. as well tested the influence of starting particle size on the breakage mechanism with a difference of approximately 15 MV [34]. The discrepancies between the two experiments were indistinct and were not elaborated further. It seems like the slopes deviate from each other, but it is a certainty that the influence is less notable than in Figure 35. Next to experiments using wet milling for size reduction, Jordens et al. determined the influence of starting particle size on the equilibrium size during sonofragementation, confirming the negligible impact of the starting size [59]. As the literature confirms the negligible impact of the starting size on the milling process, experiments for other products with different starting size were not carried out.

4.1.3 Brittleness Index

Recent literature examined the influence of solid properties on the milling process. Therefore, the BI was introduced to determine the breaking mechanism of a compound. For the calculation of this index, 3 theories, respectively based on plastic-, elastic-, and plastic-elastic deformation, are established. The BI of each compound, according to each model, is given in Table 10.

Table 10 - BI Sucrose - Ascorbic Acid - Glycine – NaCl for all models

Compound	Elastic deformation [$1/MPa\ m^{11/4}$]	Plastic deformation [$1/MPa\ m$]	Elastic-plastic deformation [$1/MPa\ m^{1/2}$]
Sucrose	$1.0 * 10^3$	$1.1 * 10^5$	0.54
Ascorbic Acid	$1.1 * 10^3$	$1.1 * 10^5$	0.47
Glycine	$1.7 * 10^3$	$2.1 * 10^5$	0.35
NaCl	$1.6 * 10^2$	$5.4 * 10^3$	0.03

Ghaderzadeh stated that, based on the BI, the compounds breaking behavior can be estimated. But depending on the theory, the order, based on the BI from high to low, differs. Because both, the elastic- and plastic deformation model, does not include the influence of the elasticity of the compound, Ghaderzadeh's elastic-plastic deformation model will be utilized to confirm the breakage behavior of the compounds. Which states that a higher BI can be associated with more mass fracture and a lower BI with more abrasion, resulting in respectively a lower C90 value and a lower C10 value.

The experiments were carried out keeping all variables, apart from the compound and the starting size of glycine, constant. The starting size was previously proven to be a non-influential property, and would therefore not play a role. The batch volume was kept at 1.56 L, as discussed in materials and methods, with a solid loading of 7m%. All slurries were milled with a 2P-4M configuration and a rotating speed of the rotor at 18 000 RPM. The stir was kept constant at a rotation speed of 500 RPM and the temperature inside the vessel was 25 °C (± 5°C). Figure 36 shows the C10 value of each compound plotted as a function of the turnovers.

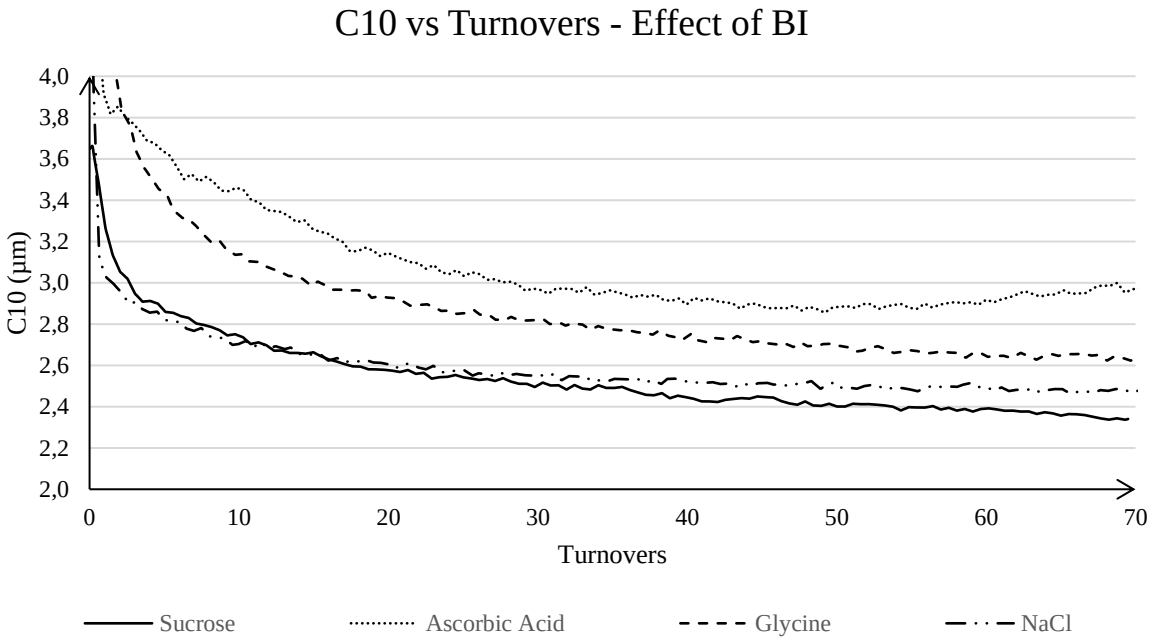

Figure 36 - C10 vs Turnovers – Effect of BI

Expected, according to Ghaderzadeh's theory, is a graph where sodium chloride reaches the lowest C10 value and glycine, ascorbic acid and sucrose each would respectively achieve a higher C10 value. Because the BI of sodium chloride drastically differs from the other compounds, it was expected that the C10 value would be significantly lower, although, As shown in Figure 36, the measurements do not fit the theory. It has to be noted that the discrepancies in C10 value over all components lies in between 0.6 µm from each other.

Because attrition particles become very small, it is possible that the lower limit of the FBRM software is exceeded. Therefore, the small particles are not measured and the C10 value, displayed by the software, is an overestimation of the actual C10 value. Also, small particles can stick together, causing the FBRM data to measure one large particle. Besides, the probability for the FBRM laser to detect these small particles is lower than the probability to

detect the larger particles, as the small particles can also disappear behind the large particles or stick at the surface of a larger particle. To confirm the measurements of the FBRM software, off-line wet- and dry samples are taken. The dry samples are vacuum filtered and dried in a vacuum oven, hereafter, measurements using the Malvern G3 Morphology are carried out. The results of the off-line measurements exclude particles with a solidity lower than 0.95 because these particles have various shapes and could influence the measurements. Table 11 show the results of the Malvern G3.

Table 11 - Malvern measurements -BI

Compound	C90 (µm)	C10 (µm)
Sucrose	9.86	2.73
Ascorbic Acid	10.53	2.21
Glycine	13.92	4.00
Sodium Chloride	12.23	2.32

It has to be noted that the measured values of the Malvern G3 can deviate from the actual values due to losses during vacuum filtering of the samples. Although, the same trend can be notices where all compounds, apart from sodium chloride, decrease in C90 as the BI, according to Ghaderzadeh, increases. To avoid the losses during sampling, off-line wet samples were taken as well. These samples are kept in a measuring cylinder, illustrated in Figure 37.

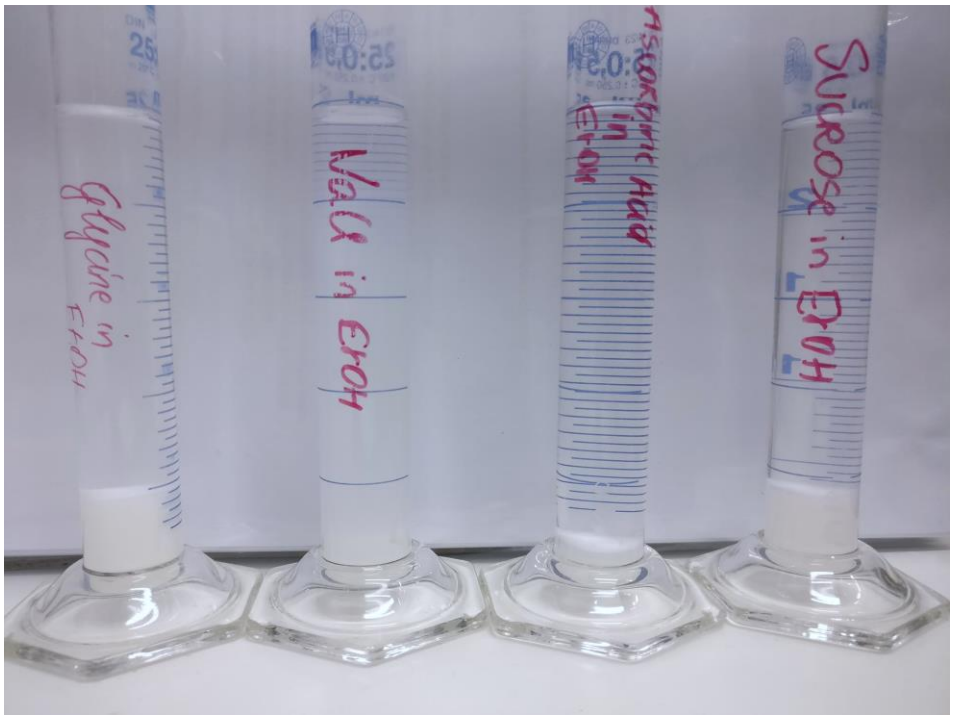

Figure 37 - Settling test after 10 hours

The cylinders from left to right are respectively filled with glycine-, sodium chloride-, ascorbic acid- and sucrose slurry in ethanol after milling. To test the precipitation rate of each slurry, which according to the Stokes' law depends on the particle size [60], the cylinders are agitated at the same moment to subsequently follow the precipitation of each slurry over time. Figure 37 illustrates this settling test after approximately 10 hours of settling. While sucrose, ascorbic acid and glycine are already settled, the sodium chloride slurry remains cloudy, suggesting the presence of more small solids. While sucrose and ascorbic acid almost immediately precipitated, the precipitation of glycine lasted a little longer, insinuating that the milling of glycine generated more finer material. To confirm that the cloudiness of the sodium chloride slurry is due to small solid particles, a wet sample from the top of the precipitation cylinder, after a moment of settling, was taken and examined with an optical microscope, as illustrated in Figure 38.

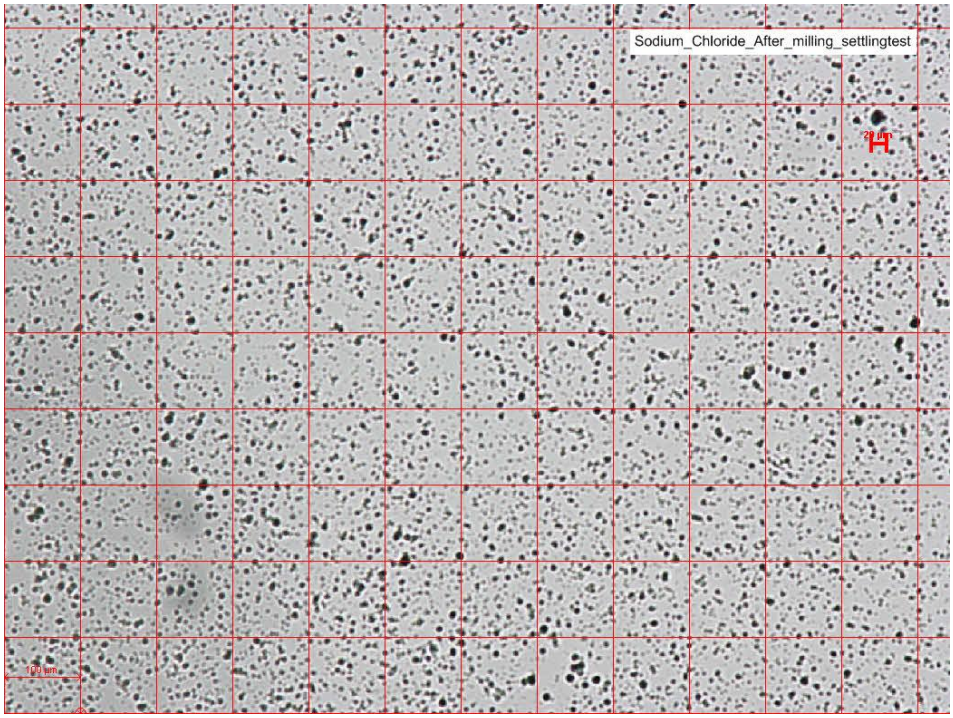

Figure 38 - Sodium Chloride settling layer – 10x magnification; grid 100 µm

Visually the average particle size illustrated in Figure 38 is estimated around 4 microns, which is near the lower limit of 1 µm of the FBRM. To confirm that these small particles are lost during dry sampling, SEM images are taken. These images, shown in Figure 39, illustrate the different compounds after milling with a magnification factor of 300. The larger sucrose and ascorbic acid particles appear to have smooth edges, while the large sodium chloride particles show more rough edges. This behavior does confirm Ghaderzadeh's theory that a decreasing BI is associated with tougher breakage, therefore, the surface of the sodium chloride is edgier due to the attrition of the particle. Important to notice is the lack of fine sodium chloride particles, which are found in the wet sample after milling. This observation confirms the loss of small particles due to vacuum filtration. A too large filter size, which lets the small particles through, can be a potential explanation for this observation. This observation explains why, despite the small particles present in the slurry, the C10 value, measured via the Malvern G3, does not estimates a lower value than for sucrose and ascorbic acid.

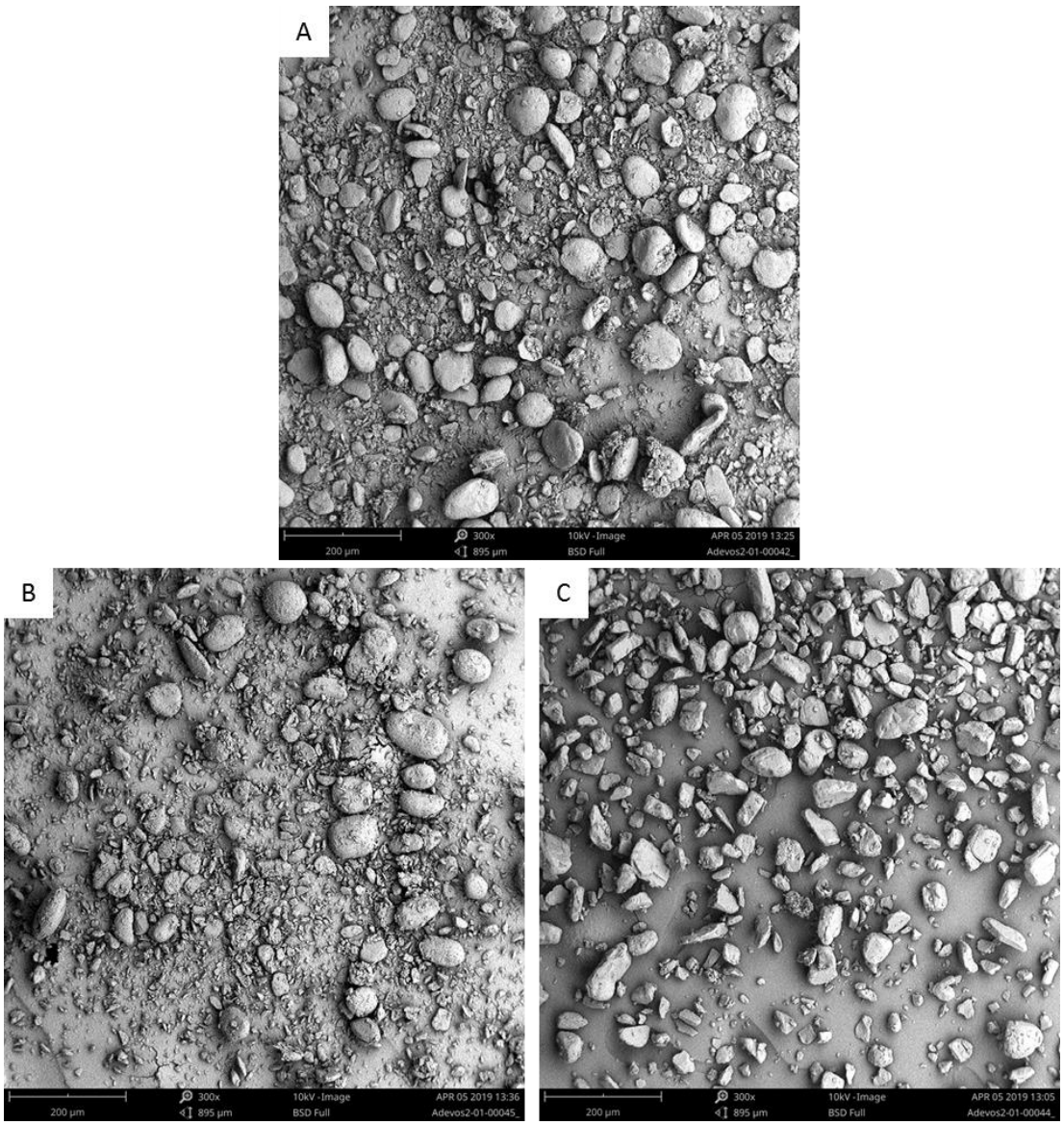

Figure 39 - SEM images A) Sucrose; B) Ascorbic Acid; C) NaCl; 300x amplified

Figure 40 shows the C90 progress of the different compounds during the milling process as a function of the turnovers. Each curve, apart from sodium chloride, confirms the breakage theory, where the C90 should decrease with a higher brittleness. The deviation from sodium chloride, which has completely different properties than the other substances, indicates that the breakage mechanism for this substance differs from the other solids.

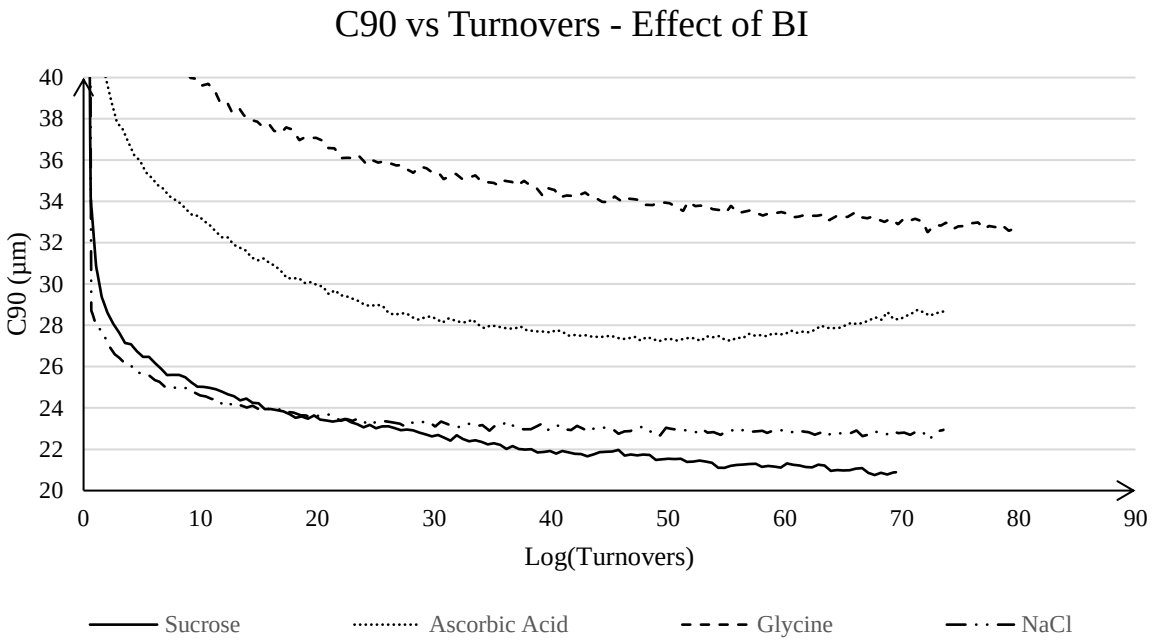

Figure 40 - C90 vs Turnovers – Effect of BI

As Ghaderzadeh's theory is based on the elastic-plastic deformation mechanism for the breakage of crystals, it is not certain that each substance behaves accordingly. Therefore, the milling of sodium chloride is tested. The properties of sodium chloride are completely out of line with the properties of sucrose, glycine and ascorbic acid, testing the theory of elastic-plastic deformation for a substance with totally different properties. Due to the deviation of sodium chloride from the theory, the possibility that the breakage of particles with different properties occurs according to Gahn's theory of purely elastic deformation [41], or Ghadiri's theory of purely plastic deformation [42] increases. Perhaps the three breakage theories are correct for a certain range of properties, insinuating that a classification system based on the properties could determine whether the breakage happens according to plastic-, elastic- or elastic-plastic deformation. On the bases of such a classification system, a robust scale-up method can be developed.

4.2 OPERATIONAL PROPERTIES ON WET MILLING PROCESS

Next to solid properties, operational properties (e.g. set-up, configuration, tip-speed) can be influential on the milling process. Therefore, the influence of these parameters is tested. All the experiments were produced in duplicate, using suction from the bottom valve, except for the experiments testing a different set-up. Each experiment was carried out with the same volume of 1.56 L, and a solid loading of 7m%. Except for the experiences at different tip-speed, all experiments were carried out with a tip-speed of 18 000 RPM. The temperature inside the vessel was kept constant at 25°C (±5°C).

4.2.1 Set-up

Traditionally, the setup in lab scale and production scale differ. Lab scale uses the suction from above, depicted in Figure 20, while production scale uses the bottom valve for suction, as represented in Figure 21. Due to a size difference between the crystals inside the vessel, segregation could influence the milling process. Again, based on Stokes' law and the stirring power is mostly distributed in the bottom part of the vessel, larger particles will have a higher probability to occur in the lower part of the vessel, while it is more likely for small particles to appear in the upper part of the suspension, as indicated in Figure 19.

During this experiment, the effect of segregation is stimulated by increasing the starting size of the solids. Therefore, three slurries with each the same solid loading (7m%), but a different starting size are made. A glycine slurry, consisting particles sieved under 250 µm mesh size, was compared with two sucrose slurries with respectively a starting size of 250 µm - 450 µm; and 450 µm - 1 mm. The progress of the C90 value, measured using FBRM software, as a function of the turnovers are illustrated in Figure 41.

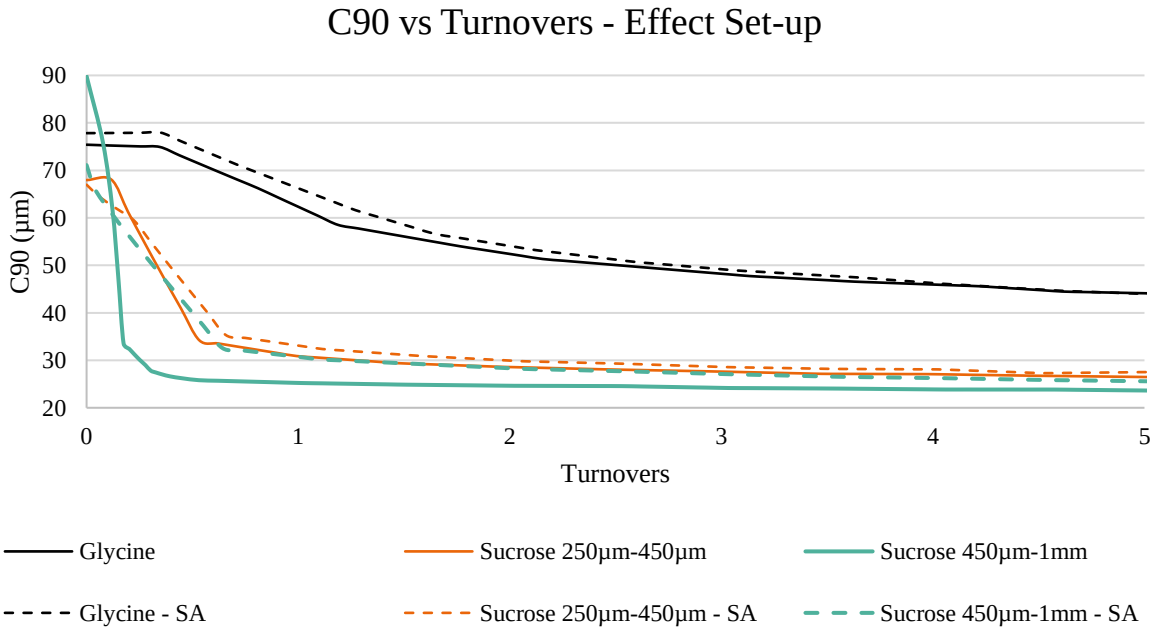

Figure 41 - C90 - set-up

Figure 41 emphasizes the first 5 turnovers from the 70 turnovers that has been made, as the further progress of the curves is identical for both set-ups. The endpoint of both set-ups is, over all three slurries, approximately the same. An important observation is the difference in turnovers necessary to achieve the endpoint. The set-up with suction from the bottom valve requires less turnovers to achieve the endpoint. The disparity between the two set-ups amplifies with larger, and consequently heavier starting crystals. Because the large particles are more likely to remain at the bottom of the vessel, they are automatically closer to the bottom valve. Therefore, it is expected for the suction from the bottom valve for the large crystals to immediately enter the mill, while for suction from above, the heavier particles will enter the mill later. This difference is amplified as the starting size increases. This confirms the influence of segregation. Therefore, all experiments were carried out using the set-up with suction from the bottom valve. During this experiments, next to the difference in set-up, the influence of only the starting size on the milling mechanism is again confirmed as the two sucrose slurries achieve the same endpoint but have a different slope at the start of the process. This is already explained above.

The fact that the segregation only influences the number of required turnovers and not the endpoint value, can be explained by the function of the stir. Because a down pumping stirrer was used, the slurry gets pushed down against the bottom of the vessel. This will create an upstream of the slurry against the wall of the vessel. This motion will release the large, heavy particles from the bottom, to make sure they pass through the mill. The effect of the stir is illustrated in Figure 42.

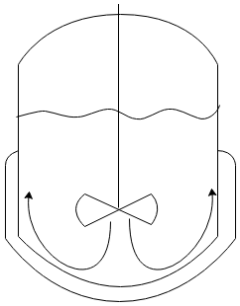

Figure 42 - Stirring effect down pumping stirrer

The same effect can be created with the outlet stream of the HSWM. Due to the high flowrates, achieved by the HSWM, the outlet stream will push the slurry, which passes in front of the outlet, down to the bottom of the vessel. If the flowrate increases, this effect will amplify, pushing the slurry down with a force large enough to hit the bottom of the vessel and create the same upstream motion as illustrated in Figure 42. Because the flowrate depends on the tip-speed of the HSWM, it is reasonable to assume that the influence of segregation can be amplified with lower tip-speeds. Using a up pumping stirrer, or reversing the rotation of the stirrer can stimulate the segregation as well.

Next to the problem of segregation, a “short-circuit” can occur with suction from above. A “short-circuit” means that the outlet stream of the HSWM is immediately sucked back through the mill. As a result, the same particles would be milled, while other particles would only have a limited amount of passes through the mill. The “short circuit” is illustrated with an arrow on

Figure 43. To avoid the creation of a short-circuit, the inlet and outlet stream of the HSWM are placed on opposite sides of the reactor and preferably on deferent heights inside the vessel.

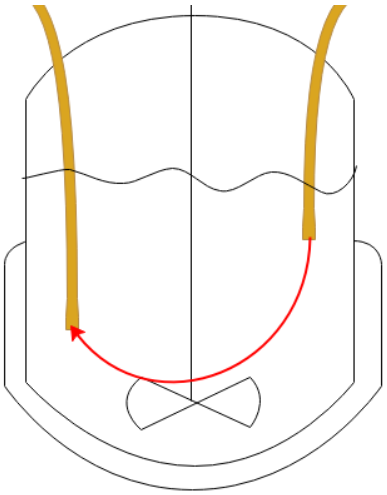

Figure 43 - Short-circuit

The fact that both set-ups achieve the same endpoint, insinuates that there was no “short-circuit” created. Although, a partially short-circuit could result in the differences obtained in the set-up, where only a limited amount of the outlet is sucked directly back in resulting in more turnovers necessary for all particles to pass through the mill. The effect of the short circuit can be tested using an angular outlet tube, so that the stream is diverted away from the inlet tube. Nevertheless this effect is scale dependent, as the possibility of a short-circuit is smaller in a larger vessel, where the inlet and outlet tube are even further removed from each other.

4.2.2 HSWM configuration

The working chamber of the HSWM, illustrated in Figure 63 added in appendix A, can be adjusted with different configurations of rotors and stators. Each rotor and stator is equipped with a certain amount of teeth, as shown in Figure 23. As the increment in teeth complicates the passage through the mill, due to a pressure drop, the flow rate will decrease. To test the influence of the configuration on the flowrate, experiments using only ethanol, water and aceton were carried out. The influence of the rotor-stator configuration on the flow rate of ethanol, which is used throughout all experiments, is illustrated in Figure 44. The flowrate of the other solvents are plotted in Figure 67 included in Appendix C – Flowrate influence configuration. The difference in flowrate, probably due to the difference in viscosity, between the various solvents is approximately 0.5 L/min depending on the used configuration.

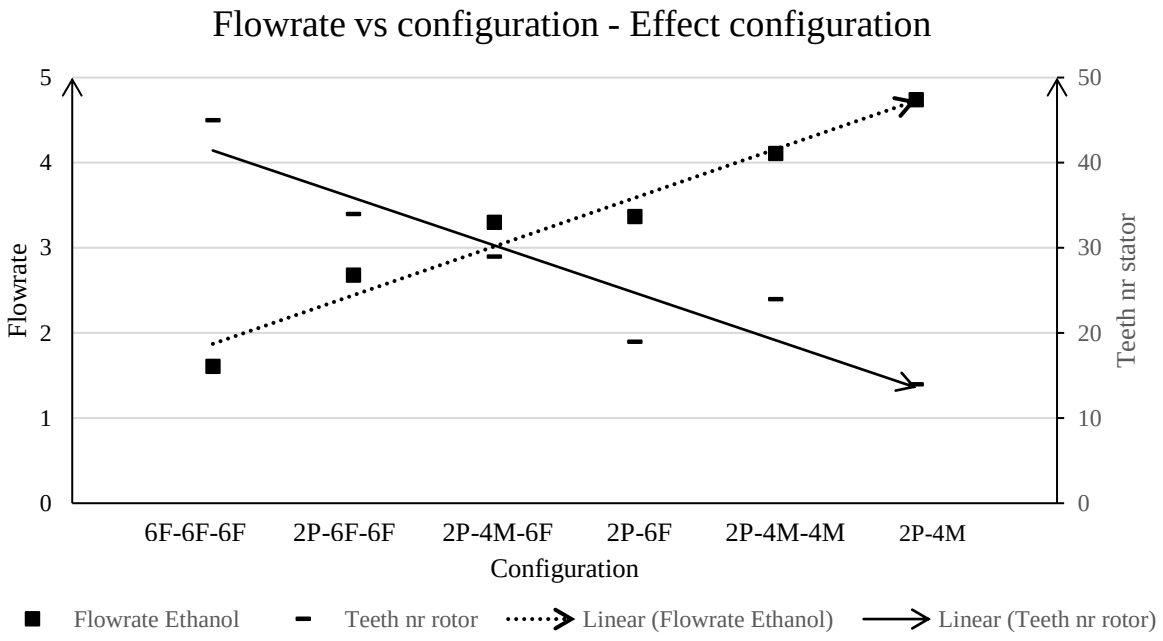

Figure 44 – Flowrate vs configuration - Effect configuration

The flowrate changes drastically as the configuration changes. Next to the flowrate, the change in teeth number of the rotors in various configurations is plotted. What immediately stands out is that the flowrate decreases as the number of teeth increases. Only the change from 2P-6F too 2P-4M-4M is an increase of teeth numbers that is followed by an increase of flowrate. A possible explanation for this observation could be the density of the 6F rotor, which can be interpreted as the number of teeth per surface area, causing more obstruction than the two stacked 4M rotors, which consists of only 2 borders with teeth and consequently is less dense.

Important to take into account is that an increase of rotor teeth results in a decrease of flowrate which means that for the same amount of batch turnovers, a significantly longer milling period is necessary. This will influence the time efficiency of the production process as well as the residence time of one particle inside the mill. This last parameter, the residence time, could be monitored using an external pump to influence the flowrate.

Next to the influence on flowrate, an increase in the amount of teeth increases the probability for a stress event to happen as the shear delivered by the disks increases proportional to the number of teeth [31]. Therefore, expectations are that the particle size would decrease as the amount of rotor-stator teeth increases. Figure 45 illustrates the FBRM data of the experiments with different configurations, carried out with glycine as solid compound.

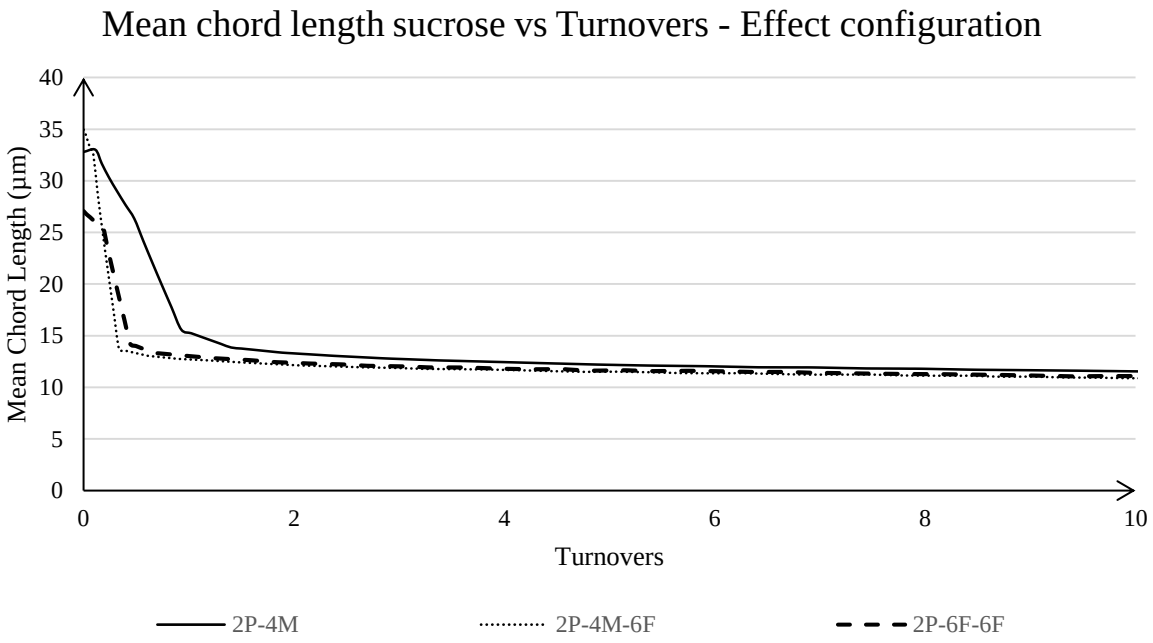

Figure 45 – Mean chord length sucrose vs Turnovers - Effect configuration

The trends from Figure 45 suggest that the rotor-stator does not influence the endpoint of the compound. By increasing the rotor teeth, the compound will only reach the endpoint slightly faster, this is confirmed via the same experiment with glycine where the same trend is noticed between the 2P-4M and 2P-4M-6F configuration, but no variation was noticed between the 2P-4M-6F and 6F-6F-6F configuration, these results are depicted in Figure 46. The conclusion cannot be made that this effect is due to the variation in configuration solely, since the tip-speed in this experiment depends on the configuration of the mill which consequently will influence the residence time of the particles in the mill, as mentioned above. To gain a better inside on the influence of only the configuration, an external pump can be implemented in the set-up. If the discrepancies are due to the configuration, the efficiency of the milling will drop as the configuration changes to higher density rotor-stators, due to a higher energy need of the mill and a lower flowrate.

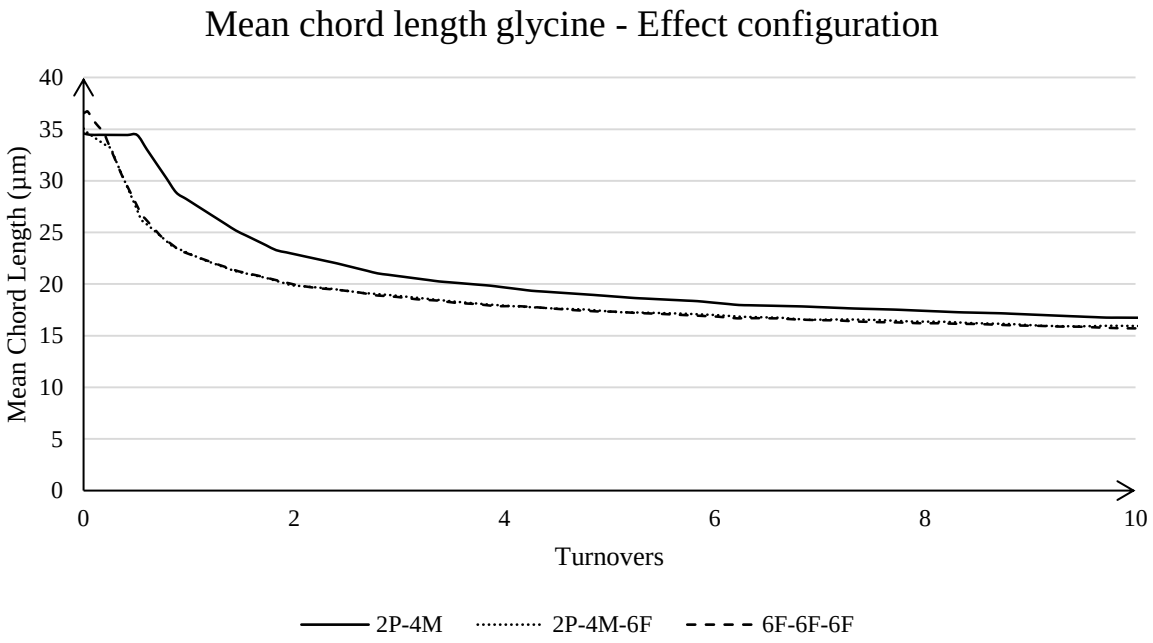

Figure 46 - Mean Chord Length Glycine – Effect Configuration

The same experiment was carried out by Engstrom et al. [32] in a vessel of 0.5 L, using a different mill, different tip-speed and different configurations, classified as respectively coarse, medium and fine, then used during this experiment. The discrepancies in endpoint between the coarse and the fine mill was around 10 microns, which is not noticed during the experiment with sucrose, nor during the experiment with glycine, where the endpoints only differ approximately 1 micron.

A possible explanation for this observation is that the particles achieved a size so small that the energy requirements to break again are too high. Transition from one configuration to another does not generate enough energy or shear for the further breakage although the number of teeth increases. This observation might confirm the theory of Engstrom et al. that states that only the other row of the rotor and stator teeth are responsible for the breakage of crystals because the extra rows are associated with a smaller diameter, which results in a lower tip-speed at the same RPM, which consequently results in a lower energy or shear generation for the collision with a particle than the outer rows [32]. Therefore, an increase in rotor stator teeth will not result in a lower particle size because the shear generation, associated with the tip-speed, of the inner teeth will not cause particle breakage below a certain size.

4.2.3 Tip-speed

The rotation speed of the rotor is adjustable at the operating unit of the HSWM. A lower rotation speed will result in a lower flowrate and, according to Equation (3), less shear generation. As the gap between the rotor and the stator is constant, the shear is directly proportional to the tip-speed of the rotor. The influence of the tip-speed, determined by the RPM of the rotor and the radius of the rotor which is constant throughout the experiments, on the flowrate is tested using only ethanol solvent and a 2P-4M configuration at three different tip-speeds: 12 000 RPM, 15 000 RPM, 18 000 RPM. The connection between the RPM of the rotor and the tip-speed is shown in Equation (31). Due to the directly proportional relationship, RPM and tip-speed will

be used interchangeably, nonetheless it will clearly be point out which unit will be used in equations that use RPM or tip-speed.

$$Tip - speed = 2\pi \cdot r_{rotor} \cdot \frac{\frac{Rotations}{minute}}{60\frac{seconds}{minute}} \quad (31)$$

From the equation can be concluded, due to a constant rotor diameter, that the tip-speed is directly proportional to the RPM. The results of the solvent based experiments are illustrated Figure 47.

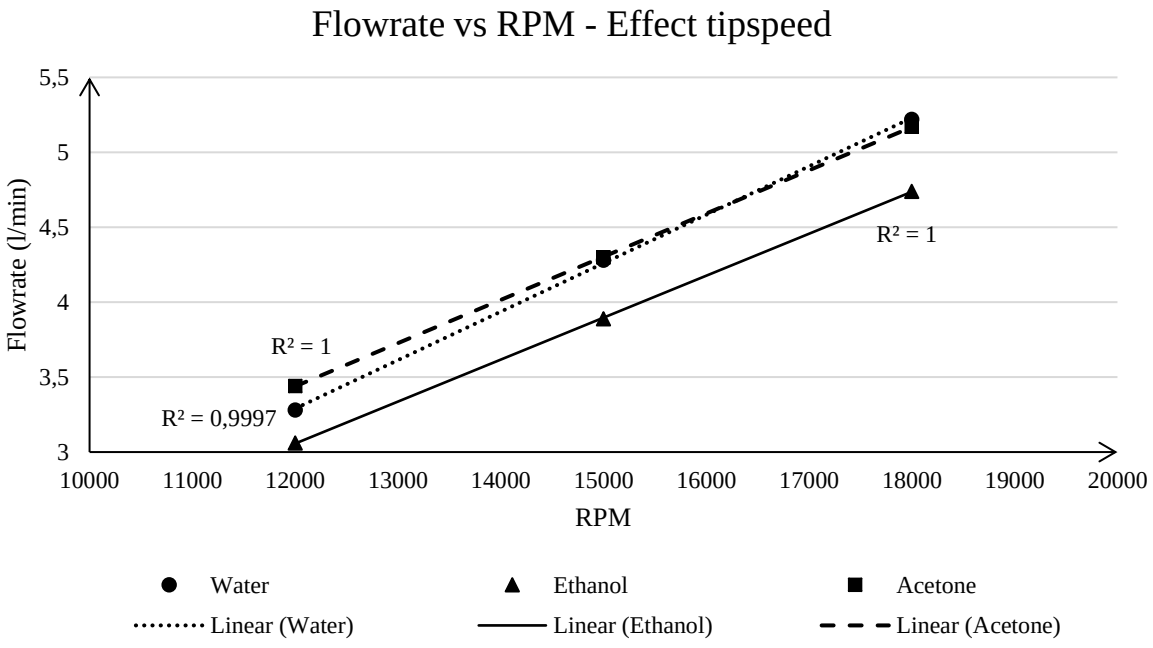

Figure 47 – Flowrate vs RPM - Effect tip-speed (2P-4M configuration)

Figure 47 shows that the flowrate is directly proportional to the RPM of the rotor. Therefore, it is also directly proportional to the tip-speed. A higher RPM will consequently result in a lower process time. Next to the lower process time, an increase in tip-speed is related to an increase in temperature. This effect can be a disadvantage as the solubility of the milled substance can strongly temperature dependent, therefore anti-solvent is used in these milling experiments. The effect of tip-speed on the temperature change in the vessel is shown in Figure 48, where the temperature increases proportional as a function of the tip-speed with a configuration of 2P-4M. Notable is the difference between the solvents, which is explained by their heat transfer coefficient as the heat transfer coefficient of water is by far the highest. This observation is dipicted in Figure 68 added in Appendix D – Energy intake – Effect heat transfer coefficient where the energy intake of the solvents during a milling process with a 2P-4M configuration at 18 000 RPM is plotted as a function of the heat transfer coefficient. This experiment was also carried out with various configurations. The influence of this is negligible as the difference in temperature change is around the three degrees between the various configurations. These results are depicted in Figure 67 added in the Appendix C – Flowrate influence configuration..

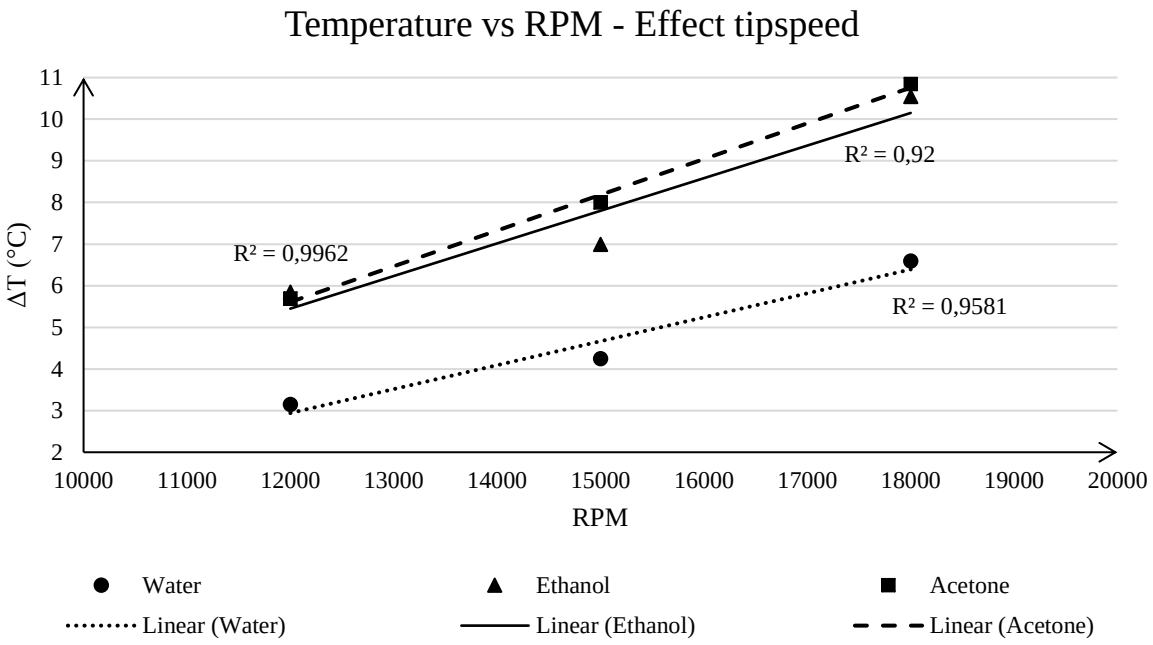

Figure 48 - Temperature vs RPM - Effect tip-speed (2P-4M configuration)

The influence of the tip-speed on the size reduction is tested using respectively 8 000, 12 000, 15 000, 18 000, 20 000 and 25 000 RPM with four different compounds, being sucrose, ascorbic acid, glycine and sodium chloride. As stated above, a higher RPM value is directly proportional with a larger increase of temperature. To keep the temperature in the vessel approximately constant around 25°C (±5°C), the temperature of the double wall of the vessel must be preemptively set at lower temperatures as the tip-speed increases. For every experiment, apart from the experiments carried out at 25 000 RPM, it was succeeded to keep the temperature inside the vessel between the lower- and upper limit of respectively 20°C and 30°C. It is important to note that anti-solvent was used, consequently the influence of the temperature during this experiment is negligible. Nevertheless, the temperature influence might be important as API's are milled, what makes it important to note that the temperature control is more difficult with increasing tip-speed. The result of the different experiments are plotted in a graph, illustrated in Figure 49.

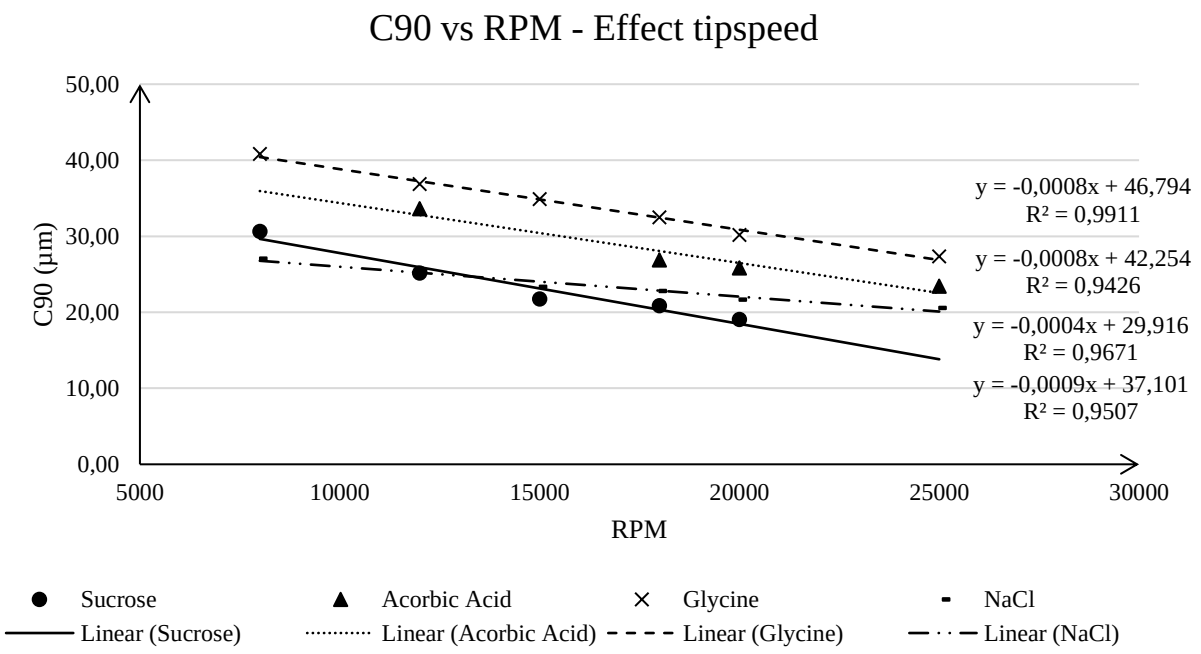

Figure 49 - C90 vs Turnovers – Effect tip-speed

It is reasonable to conclude that the milling process is correlated with the RPM of the rotor. All C90 values of the different compound have a linear relationship with the RPM, confirmed via R^2 values approaching 1. Notable is the slope of the linear from the compounds, as sucrose, ascorbic acid and glycine have, roughly, the same slope, sodium chloride clearly deviates with approximately half the slope from the other materials. This confirms the deviant behavior of sodium chloride compared to the other compounds and suggest a classification system based on material properties and possibly the breakage rates. To gain more insight on the effect of rotational speed of the rotor, the influence of tip-speed on the C10 value is plotted in Figure 50.

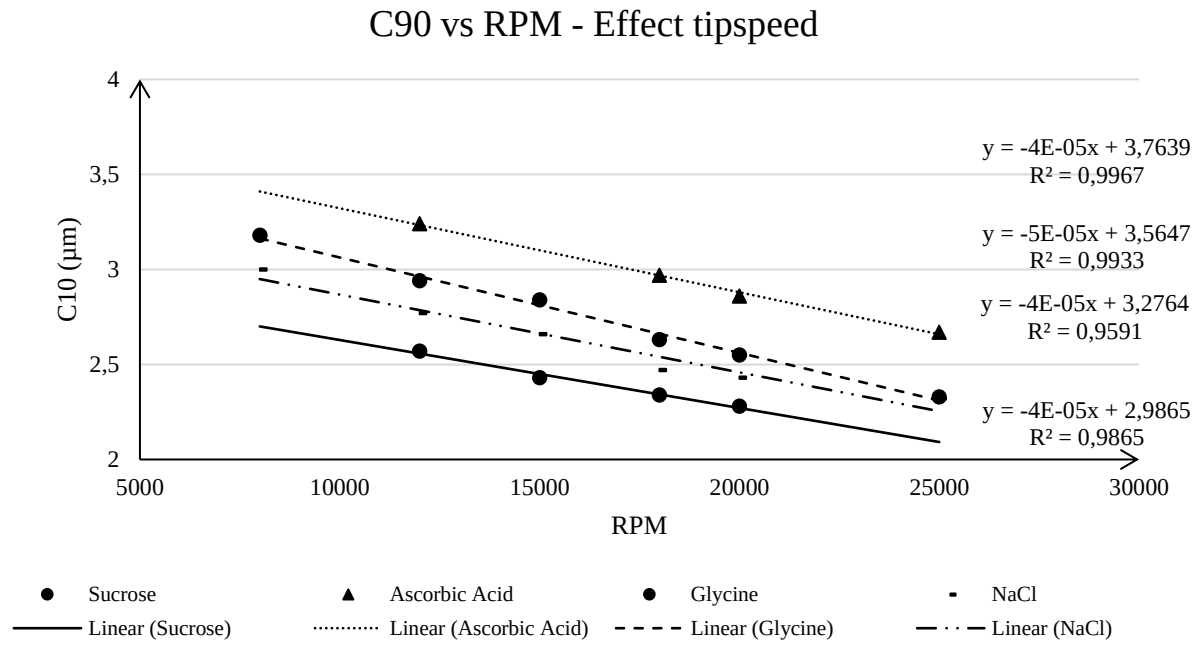

Figure 50 - C10 vs Turnovers - Effect tip-speed

Based on the both graphs, C90 and C10, the influence of the rotational speed can be determined on both small and coarse crystals. As illustrated in the graph, the C10 values are, such as the C90 value, reversely proportional to the rotation speed of the rotor. The difference between highest and lowest C10 value is much lower, suggesting that a higher rotational speed particularly influences the coarse crystals in the slurry. The slope of glycine's C10 value is slightly higher, approximately 1.5 times the slope of sucrose, than the other compounds, suggesting that glycine generates more fines at higher RPM values. Again the measurement errors of the FBRM, discussed above, could be an explanation for the deviation.

As the influence of RPM on each component, apart from sodium chloride, delivers a difference in C90 of around 13 µm (±3µm) between lowest and highest RPM values, while change in other properties only delivered changes of around 2 µm, it is reasonable to say that the influence of rotational speed of the rotor is the most influential parameter in the milling test. Both coarse and fine crystals are influenced.

4.3 BREAKAGE MODEL VALIDATION

As Ghaderzadeh compared different breaking models respectively based on elastic-, plastic- and elastic-plastic deformation by milling sucrose, ascorbic acid and glycine with a silverson L4R rotor-stator mixer at various tip-speeds, the same experiments were carried out with the IKA Magic Lab® to validate the three different methodologies of breakage based on respectively elastic-, plastic- and elastic-plastic deformation for a different mill. Therefore, experiments with the same solid loading (7m%) at various tip-speeds are carried out for sucrose, ascorbic acid and glycine. Due to the different behavior of sodium chloride in the previous experiments, sodium chloride is also plotted to confirm the methodology for compounds with a deviant behavior. The calculations are made for both, macroscale turbulence and inertial subrange turbulence.

4.3.1 Validation methodologies

Figure 51 illustrates the logarithmic plot of the C90 divided by the rotor diameter as a function of the inversed tip-speed. The regression of this plot gives a function as illustrated in Equation *(32)*.

$$\log\frac{C90}{D} = a \cdot \log\frac{1}{tip - speed} + b \qquad (32)$$

The slope, which is represented by "a" in the equation above, can be, according to the conversion of logarithms, illustrated as the exponent of the tip-speed. Ghaderzadeh predicted this exponent for each breakage model, this prediction is discussed in the literature study and illustrated in Table 12.

Table 12 - Slope prediction breaking models [45]

Model	Prediction slope
Elastic Deformation	$\frac{24}{17} \approx 1.4$
Plastic Deformation	$\frac{6}{5} \approx 1.2$
Elastic-Plastic Deformation	$\frac{12}{7} \approx 1.7$

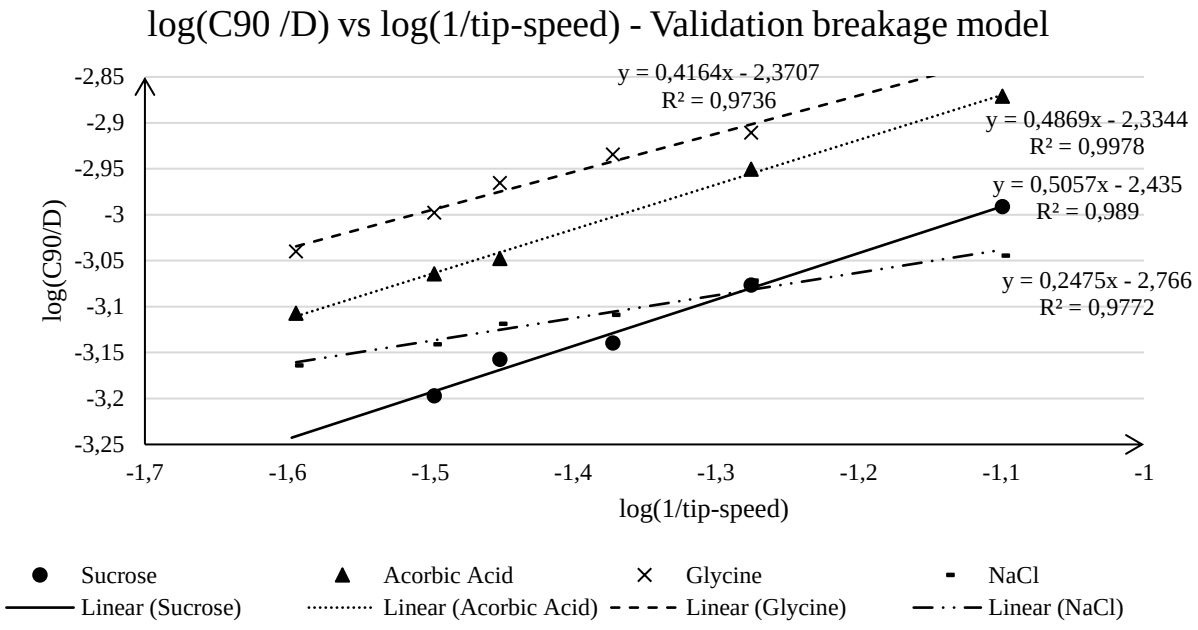

Figure 51 – Log(C90/D) vs log(1/tip-speed) – Validation breakage model

Immediately the same observation as Ghaderzadeh can be made. The slopes of sucrose, glycine and ascorbic acid are roughly the same with an average of 0.47. Again, the deviation of sodium chloride is obvious. The slope is about half the slope of the other curves, insinuating a different breakage model. In contrast to Ghaderzadeh, the slopes of the curves are less steep, which indicates that each of the different breakage models underestimates the energy necessary to break the particles. The difference in mill can be a possible explanation for the deviation in slope, as the energy dissipation over the mill can differ. Because the C90 decrease, using the Silverson mill, is much higher, it is reasonable to conclude that the energy dissipation over the IKA mill is less efficient. To confirm the deviation, the data is plotted as a function of the Co, shown in Table 13, these results, for both MT and IST, are depicted in Figure 52 - Figure 57.

Table 13 - Comminution number plot - breakage models

Model	Plot IST	Plot MT
Plastic Deformation	$\frac{x}{D} \sim \left(\frac{K_c^2}{\rho_p H D}\right)^{\frac{3}{5}} \frac{1}{\mu_{tip}^{6/5}} = (Co_P)^{-\frac{3}{5}}$	$\frac{x}{D} \sim \frac{K_c^2}{\rho_p H D} \frac{1}{\mu_{tip}^3}$
Elastic Deformation	$\frac{x}{D} \sim \left(\frac{K_c^{\frac{3}{2}}}{\rho_p H^{\frac{1}{2}} D^{\frac{3}{4}}}\right)^{\frac{12}{17}} \frac{1}{\mu_{tip}^{24/17}} = (Co_E)^{-\frac{12}{17}}$	$\frac{x}{D} \sim \left(\frac{K_c^{\frac{3}{2}}}{\rho_p H^{\frac{1}{2}} D^{\frac{3}{4}}}\right)^{\frac{4}{3}} \frac{1}{\mu_{tip}^{8/3}}$
Elastic-Plastic Deformation	$\frac{x}{D} \sim \left(\frac{E K_c}{\rho_p H D^{\frac{1}{2}}}\right)^{\frac{6}{7}} \frac{1}{\mu_{tip}^{12/7}} = (Co_{EP})^{-\frac{6}{7}}$	$\frac{x}{D} \sim \left(\frac{E K_c}{\rho_p H D^{\frac{1}{2}}}\right)^{2} \frac{1}{\mu_{tip}^2}$

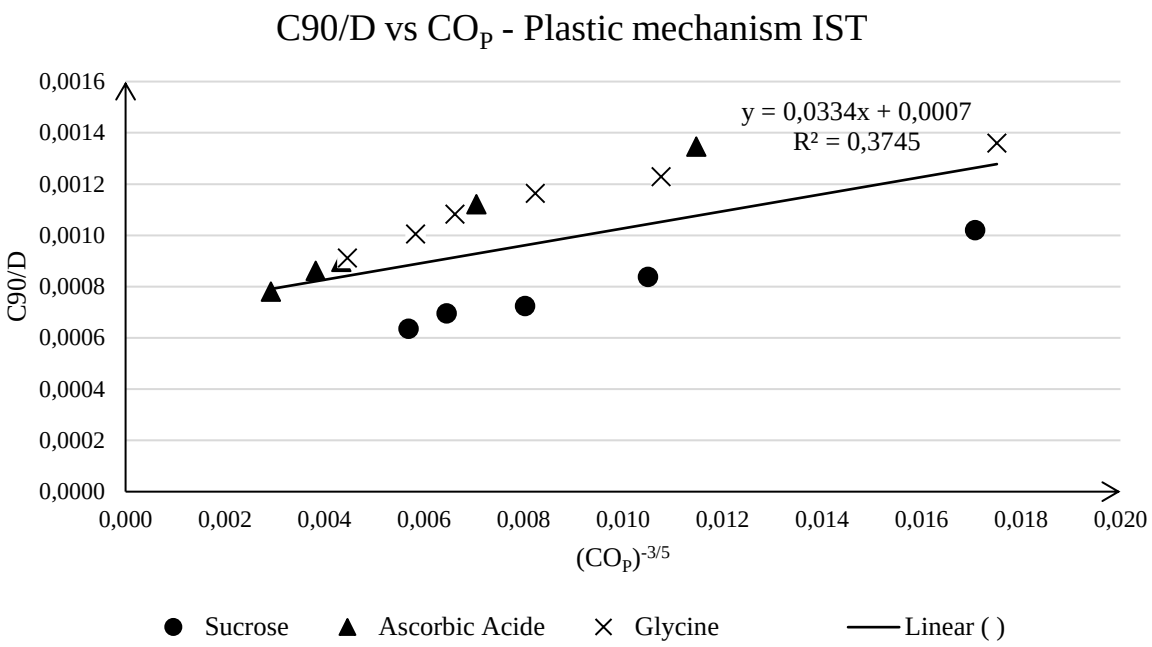

Figure 52 - C90 vs CO$_P$ - Plastic breakage mechanism IST

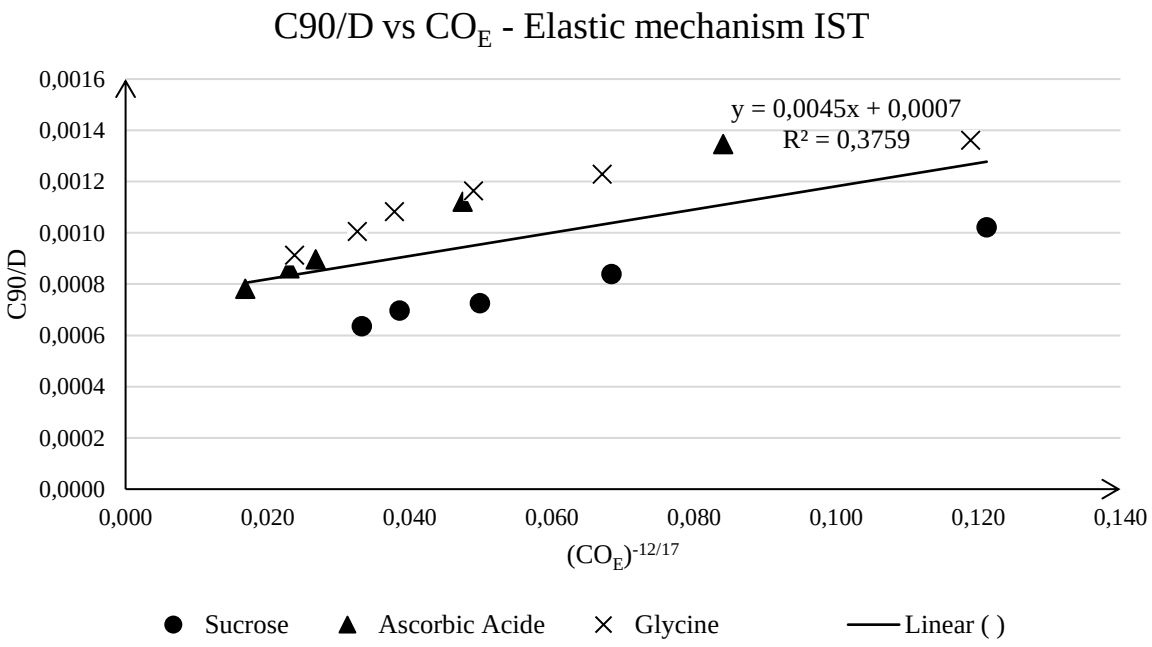

Figure 53 - C90/D vs CO$_E$ - Elastic breakage mechanism IST

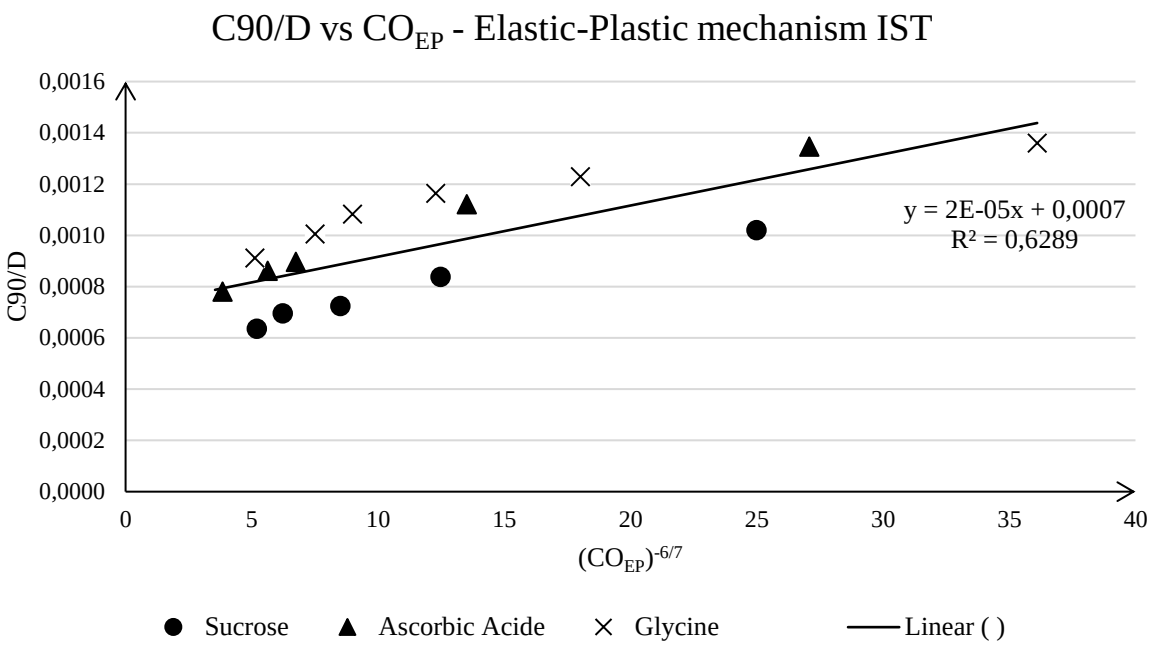

Figure 54 - C90/D vs CO_{EP} - Elastic-Plastic breakage mechanism IST

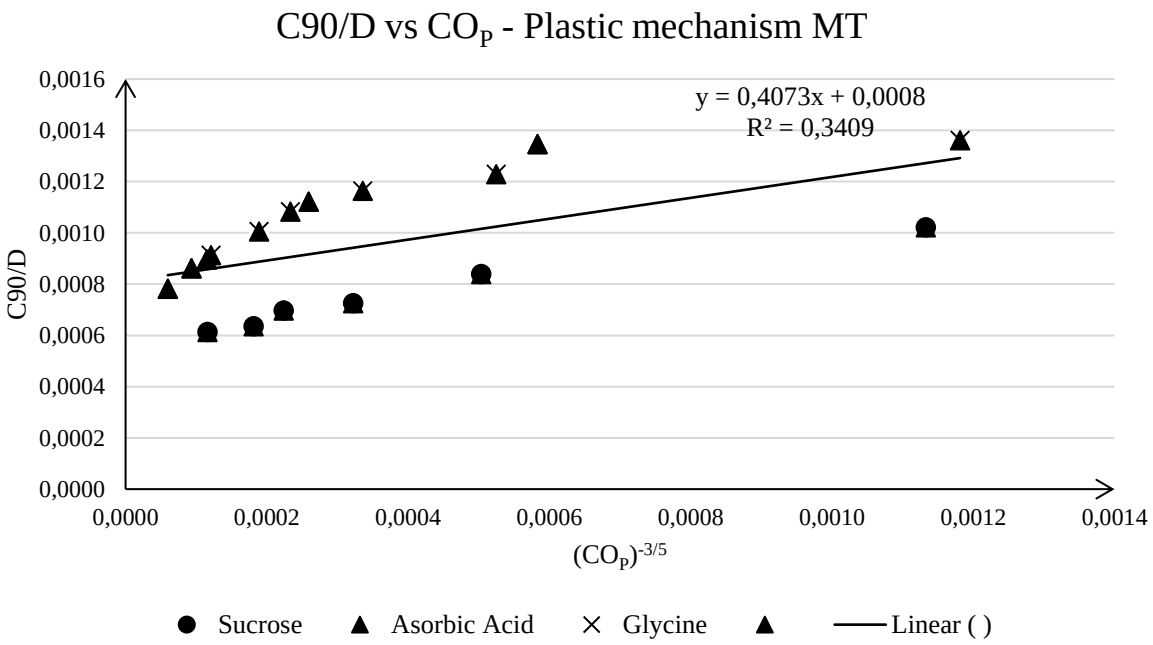

Figure 55 - C90 vs CO_P – Plastic breakage mechanism MT

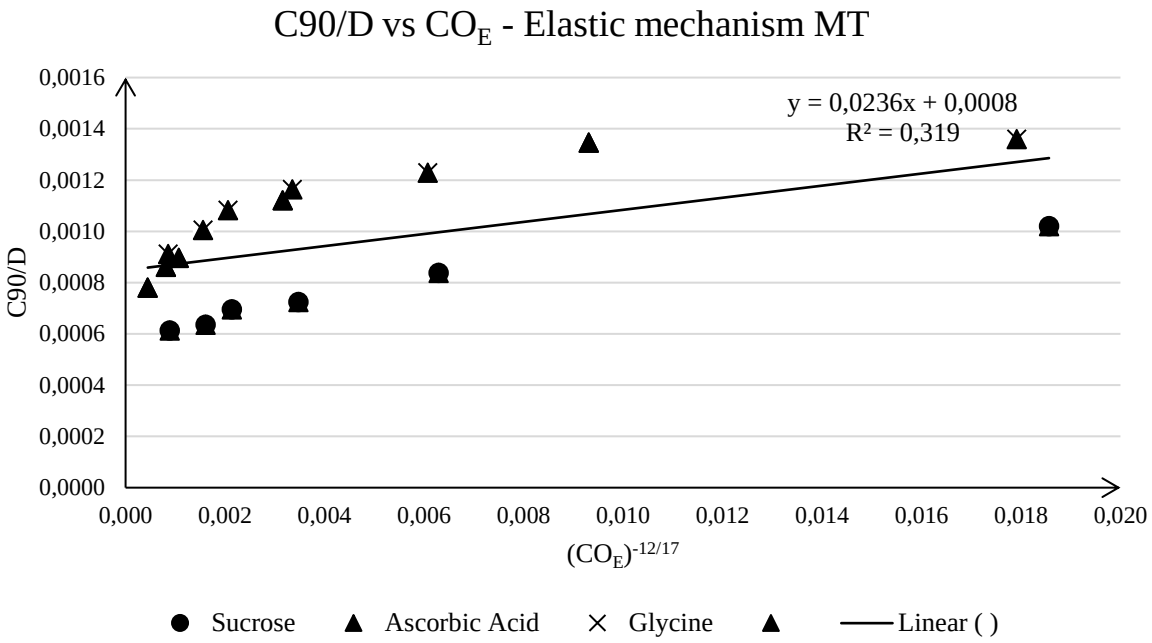

Figure 56 - C90/D vs CO_E – Elastic breakage mechanism MT

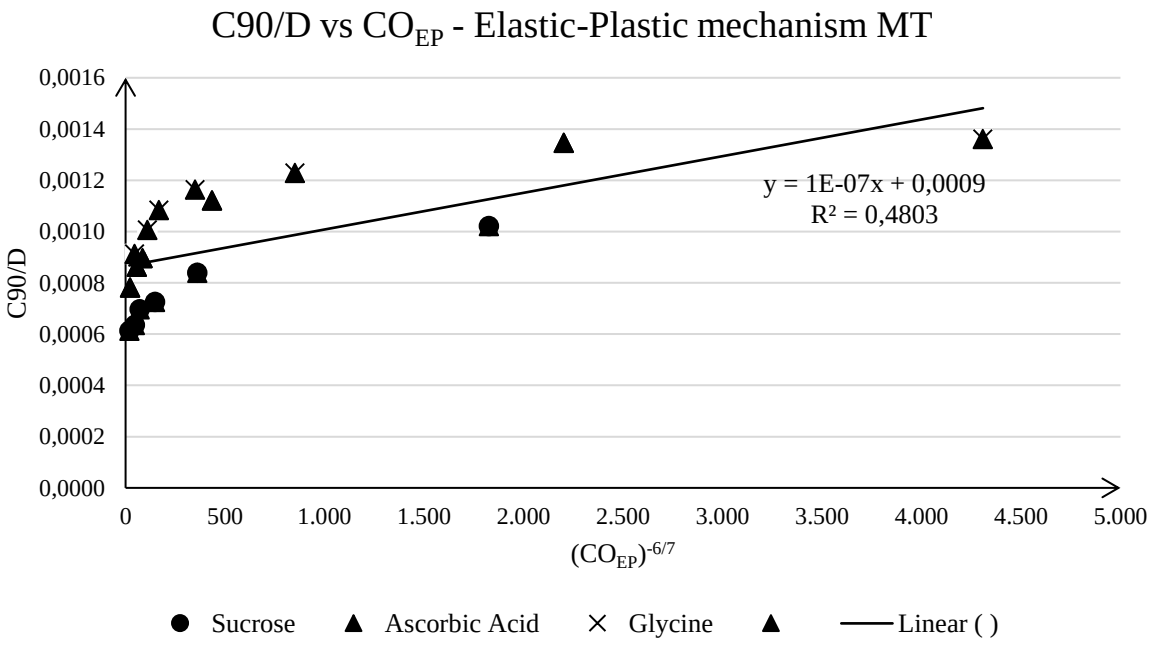

Figure 57 - C90/D vs CO_{EP} – Elastic-Plastic breakage mechanism MT

As the R^2 of the different plots does not approach a value of 1, it is reasonable to say that the linear correlation between the comminution number and the C90/D is not confirmed. The deviation from the breakage models can be explained by a difference of mill, which would have a different energy dissipation across the milling chamber. As is stated in the literature study, due to high turbulence created by the high shear mill, the breakage of particles is a compensation of the created eddy fluctuations. As the mill has a different geometry, the created eddy fluctuations will deviate and consequently so will the breakage. What stands out is the clearly better correlation achieved with Ghaderzadeh's comminution number in comparison with that of Gahn and Ghadiri, suggesting that the influence of the elasticity of a compound, as

Ghaderzadeh is the only one including this property in his Co, can be an important characteristic in the breaking of crystals. To confirm the different fracture behavior of sodium chloride, the experimental data is also plotted as a function of the comminution number, illustrated in Figure 58 - Figure 60, these are all for the IST models, because this model achieved a better correlation. The sodium chloride plot for the MT is added in Appendix F – Macroscale Turbulence plot sodium chloride Figure 70 - Figure 72. A summarizing table of the different plots is given in Table 14.

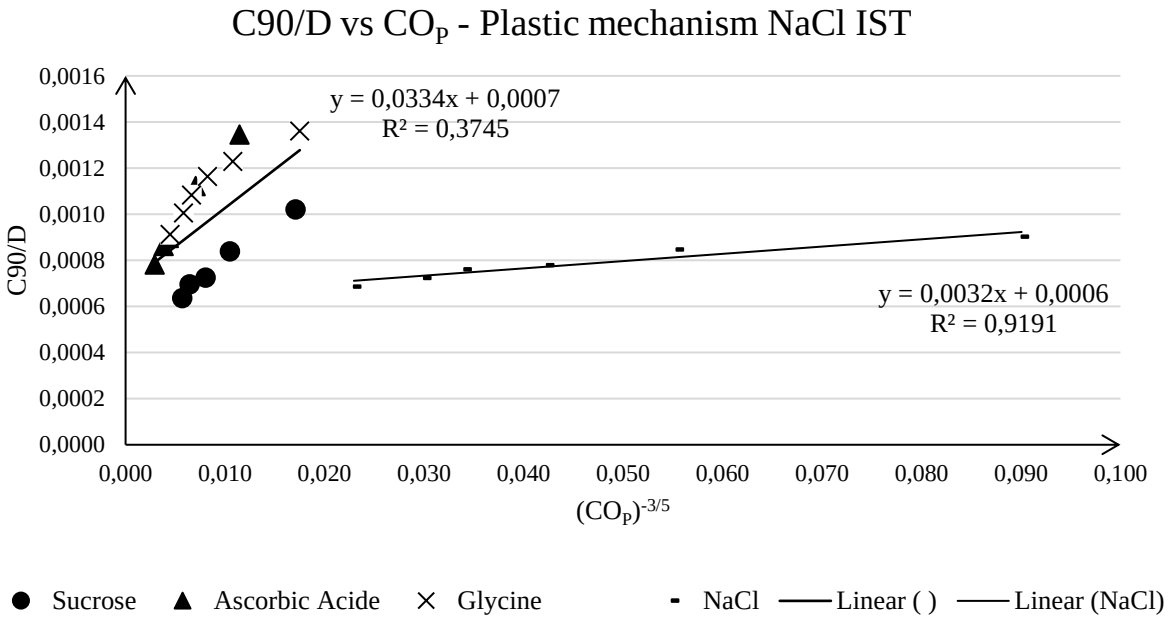

Figure 58 - C90/D vs CO_P - Plastic mechanism Sodium Chloride IST

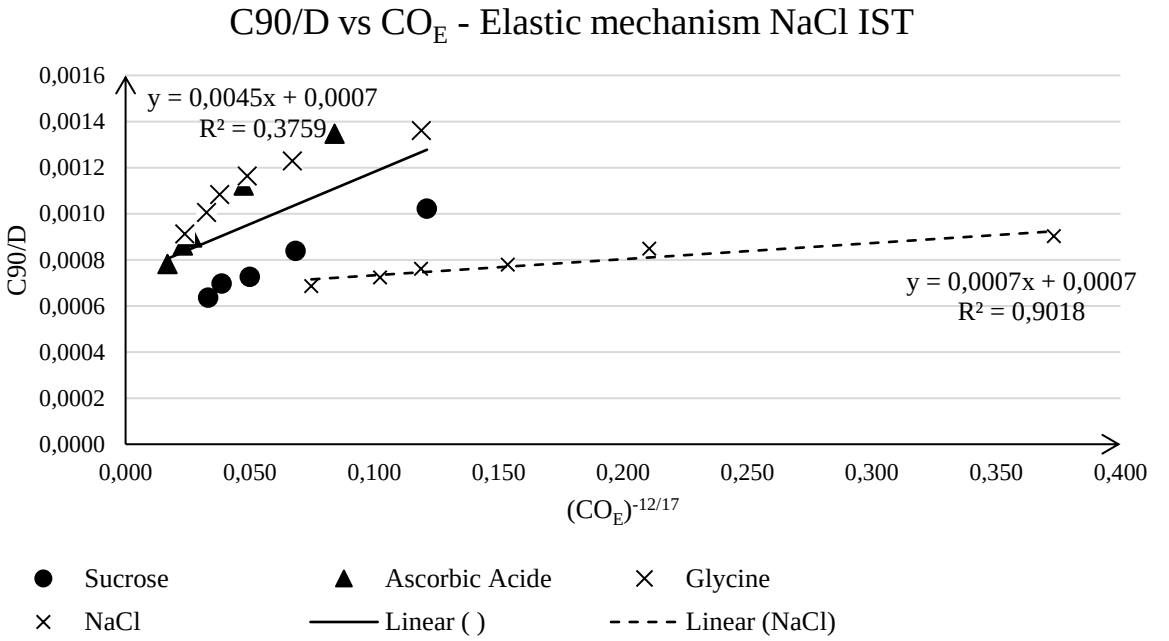

Figure 59 - C90/D vs CO_E mechanism Sodium Chloride IST

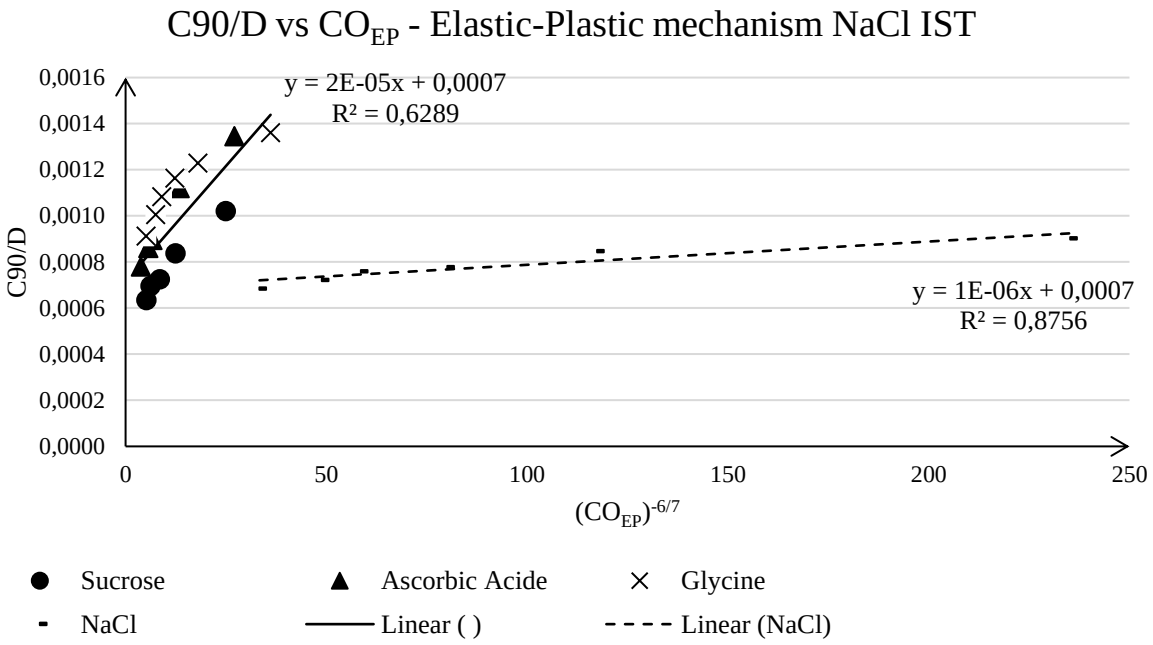

Figure 60 - C90/D vs CO_{EP} mechanism Sodium Chloride IST

Table 14 - Summarizing table IST vs MT plot

Model	Plot IST	Plot MT
Plastic Deformation	R^2 = 0.3745 NaCl fit: R^2 = 0.9191	R^2 = 0.3409 NaCl fit: R^2 = 0.8501
Elastic Deformation	R^2 = 0.3759 NaCl fit: R^2 = 0.9081	R^2 = 0.3190 NaCl fit: R^2 = 0.9018
Elastic-Plastic Deformation	R^2 = 0.6289 NaCl fit: R^2 = 0.8756	R^2 = 0.4803 NaCl fit: R^2 = 0.6937

For each model, the sodium chloride trend is strongly shifted to the right, due to an increase in Co, and slightly rotated to the right, which represents a more gradual slope. The shift, due to the Co of the compound, can be explained via the compound mechanical properties. Because the hardness, fracture toughness and density of sodium chloride strongly differs from the other compounds, the Co will differ as a consequent. While the slope can be explained through the breakage of the compound, were a decrease in slope represent a more difficult breakage behavior.

Notable is that the best fits, all approaching a R^2 of 1, are achieved using both the elastic- and the plastic deformation mechanism for both MT and IST. The sodium chloride fit of the elastic-plastic mechanism according to Ghaderzadeh achieves in both MT and IST the worst correlation. This suggests, yet again, that the sodium chloride breakage mechanism totally

differs from the other three compounds, which all achieved the best fit using the elastic-plastic deformation model. It is reasonable to say that, even for sodium chloride, the IST is still a better approach for the breakage mechanism.

The question that arises is if this shift is also observed for other compounds with roughly the same properties as sodium chloride. If this is the case, it is possible that the breakage models can be applied for certain classes, created from the properties of the compounds. The linearity of sodium chloride in the graphs above is best approached by the plastic mechanism established by Ghadiri [42], this could be an indication of the breaking mechanism of compounds with the same properties as sodium chloride.

4.3.2 Empirical approach

Based on the breakage models, discussed above, an empirical breakage model for the IKA Magic Lab® is estimated. Therefore, the material properties of the compounds are fit, using the same relationship as the other breakage models, where the model was directly proportional to the fracture toughness and the elasticity, but reversely proportional to the hardness and the square weight of the tip-speed. By influencing the exponent of the material properties, as shown in Equation *(33)*, the best fit is determined. Because the diameter of the rotor is always a constant in the Magic Lab® mill, this is eliminated from the equation.

$$Log(C90) \sim \log\left(\frac{{K_c}^x E^y}{\rho_p H^z {u_{tip}}^2}\right) \qquad (33)$$

The exponents are determined in excel, starting with a value 1. The predicted log(C90/D) values of the linear correlation are calculated, thereof the RMSE is defined. With Excels solver function, the minimum value of the RMSE is determined by manipulating the exponents values in the function. The best fit, which is depicted in Figure 61, with the function shown in Equation *(34)*.

$$\log(C90) \sim \log\left(\frac{{K_c}^{0.93} E^{3.47}}{\rho_p H^{4.14} {u_{tip}}^2}\right) \qquad (34)$$

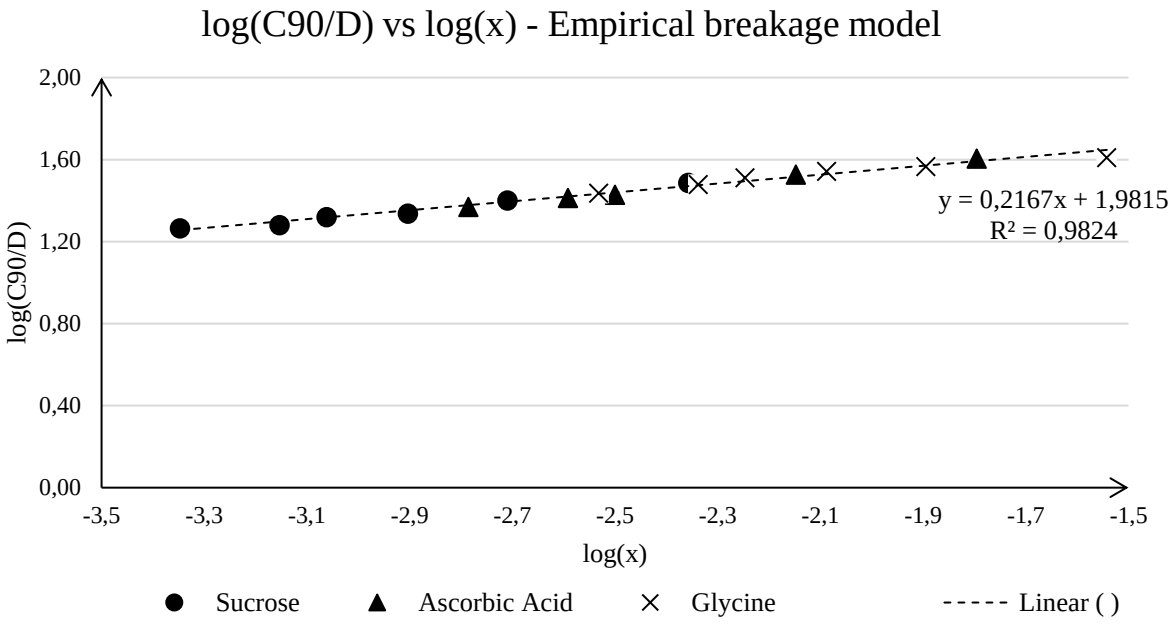

Figure 61 - Log(C90) vs log(x) - Empirical model

The x value, used to determine the x-axis, represent the best fit equation, given above. It is not a certainty whether this fit is useful for all components milled with the IKA Magic Lab®. To confirm the linearity of this fit, the experimental data of sodium chloride is fit as well, as illustrated in Figure 62.

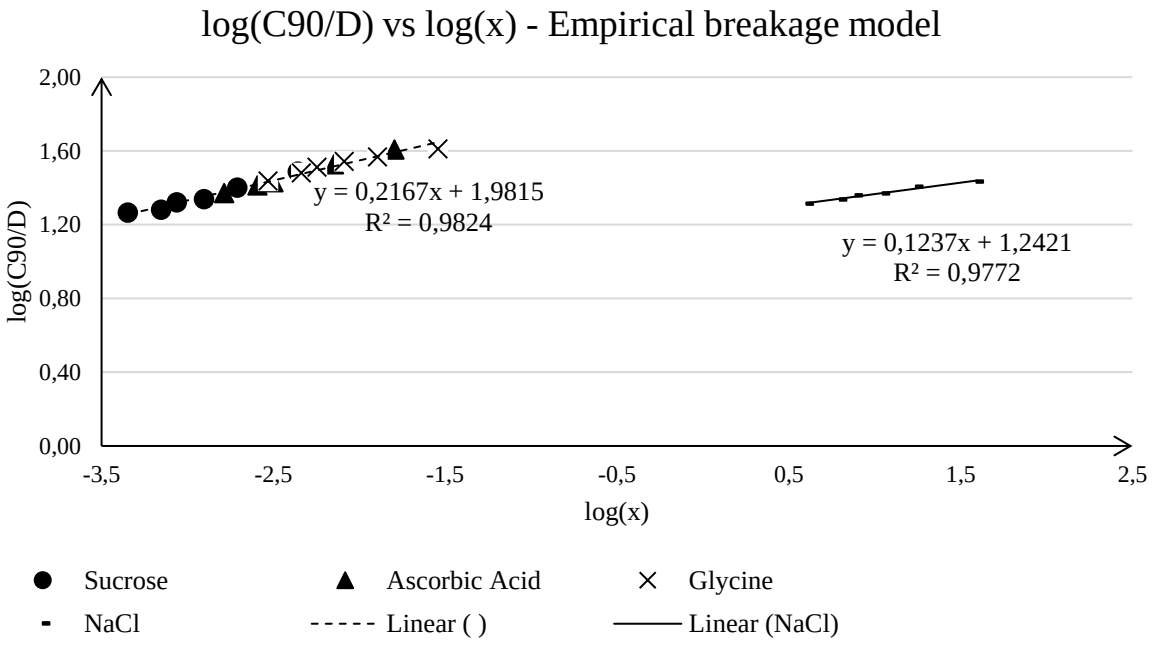

Figure 62 - log(C90) vs log(x) - Empirical model NaCl fit

Again the same shift from sodium chloride is noticed. What is important is the linearity of sodium chloride, despite the compound was not included in the model calculation. This can be an indication that the model is useful for the IKA mill. Due to the shift of sodium chloride in each experiment, a possible classification, based on the result of these experiments, is given in

Table 15. This classification system has yet to be validated via components that are within the given range.

Table 15 - Classification system

	Relative easy to break	Hard to break
H (MPa)	887 - 1105	±216
E (MPa)	21150 – 32270	±37300
K_c (MPa)	0.069 – 0.097	±0.2

This classification system gives the range of properties for components which are experimentally found more difficult or easier to break. This system is composed based on the breakage of only four components of which three components appear to have the same breaking mechanism and only one compound totally deviates from this. Therefore, the classification can still be adjusted.

5 CONCLUSION

This master's thesis explored the influence of both solid properties and operational properties on the milling mechanism of IKA's Magic Lab® high-shear rotor-stator wet mill. In addition, a theoretical breakage model was tested for multiple compounds with different mechanical properties on a recycle loop vessel in order to achieve an insight on the working mechanism of IKA's HSWM.

First of all, the influence of solid properties of multiple components on the milling process were tested. The effect of solid loading was determined negligible on the equilibrium size as only the slope, which represent the rate of the size reduction, increases slightly as more crystals are present in the vessel. This observation is interpreted as the increase in collision frequency, which will only influence the rate of breakage, but not the final crystal size. In addition, the starting size of the crystals were compared with the same solid loading. As the size of the crystals increases, less particles will be present in the vessel, causing the collision frequency to drop. Despite the frequency drop, the slope of the breakage rate is steeper with increasing particle size, but will achieve the same equilibrium size after milling. This can be explained vie the intensity of each collision. As the size increases, the intensity of the collision will increase proportional due to a higher kinetic energy. As a final solid property , the mechanical properties of multiple solids are compared, using a theoretical model that states that more brittle compounds break easier while less brittle materials should have more abrasion. To validate this theory, sucrose, ascorbic acid, glycine and sodium chloride, which properties totally differ from the others, are compared. The theoretical trends were retained for each compound, apart from sodium chloride. Based on the in-line measurements, sodium chloride achieved a lower C90 value, while the C10 value did not differ from the other compounds. Using SEM images and off-line wet samples was this observation disproved by suggesting that sodium chloride generates a lot of fines.

Furthermore, the difference between the set-up at lab scale, with suction from above which is a possibility, and production scale, using suction from the bottom valve, turns out to be negligible. Increasing the starting solid size does amplify the differences, confirming the effect of segregation in the lab scale set-up, but does not create a difference in endpoint. Therefore, the production scale set-up is more appropriate for the milling set-up, due to its independence on segregation. Next to the set-up, the mill configuration is determined to be negligible. An increase in stages and rotor teeth does not create enough energy to lower the endpoint of the milling process. The tip-speed was determined to have the largest impact on the endpoint of the milling process. As the tip-speed increases, the endpoint lowers proportionally. This effect is influenced by the particle specific properties, therefore insinuating a classification system is necessary.

Finally, the breakage models based on elastic-, plastic- and elastic-plastic deformation are recreated, using a different mill and an extra component, being sodium chloride. Due to a deviation over all models, it was concluded that the difference in mill is responsible for a difference in energy dissipation, which results in discrepancies between the literature and the experimental date. Therefore, an empirical approach was used to create a breakage model for the IKA Magic Lab® mill.

6 RECOMMENDATIONS

To gain even more information over the working principle of the mill, a single pass set-up, where all crystals inside the vessel are obligated to go through the mill once, can be interesting to see whether all particles break when going through the mill or if some particles remain untouched.

Despite that the effect of segregation was tested via different set-ups, there still other methods to determine the effect of segregation. Using another stir, another rotation direction of the stir or creating a u-turn in the outlet stream of the HSWM are all possibilities to influence the effect of segregation, as well as the effect of a "short-circuit". Using these techniques, it could be possible to minimize the effect of segregation, unreliable of the size of the starting material.

In addition, to create a more supported classification system, other compounds with the same and totally different mechanical properties can be tested. Possible compounds, which have approximately the same properties as sucrose and sodium chloride, are respectively acetaminophen [61] and lithium chloride[38]. Another method to create a classification system can be based on the Kapur equation [62]. Based on the equation, established by Kapur, the milling behavior of compounds and breakage rate from a certain size to a specific smaller size can be determined.

BIBLIOGRAPHY

[1] "Our Story | Janssen." [Online]. Available: https://www.janssen.com/about/our-story. [Accessed: 04-Mar-2019].

[2] "Biopharmaceutics Classification System (BCS)." [Online]. Available: https://www.absorption.com/kc/biopharmaceutics-classification-system-bcs/. [Accessed: 12-Apr-2019].

[3] C. Y. Wu and L. Z. Benet, "Predicting drug disposition via application of BCS: Transport/absorption/ elimination interplay and development of a biopharmaceutics drug disposition classification system," *Pharm. Res.*, vol. 22, no. 1, pp. 11–23, 2005.

[4] E. Flynn, "Pharmacokinetic parameters," *xPharm Compr. Pharmacol. Ref.*, pp. 1–3, 2011.

[5] S. Mehta, N. M. Joseph, F. Feleke, and S. Palani, "IMPROVING SOLUBILITY OF BCS CLASS II DRUGS USING SOLID DISPERSION: A REVIEW," *J. Drug Deliv. Ther.*, vol. 4, no. 3, pp. 7–13, 2014.

[6] "Water Solubility." [Online]. Available: http://npic.orst.edu/envir/watersol.html. [Accessed: 18-Mar-2019].

[7] S. Michinori, I. Teruko, O. Hiroshi, A. Hidekazu, and O. Masaki, "Effects of absorption enhancers on the transport of model compounds in Caco-2 cell monolayers: Assessment by confocal laser scanning microscopy," *J. Pharm. Sci.*, vol. 86, no. 7, pp. 779–785, 2000.

[8] C. A. Lipinski, F. Lombardo, B. W. Dominy, and P. J. Feeney, "Experimental and computational approaches to estimate solubility and permeability in drug discovery and development settings," *Adv. Drug Deliv. Rev.*, vol. 64, no. SUPPL., pp. 4–17, 2012.

[9] A. A. Noyes and W. R. Whitney, "The rate of solution of solid substances in their own solutions," *J. Am. Chem. Soc.*, vol. 19, no. 12, pp. 930–934, 1897.

[10] R. Ghadi and N. Dand, "BCS class IV drugs: Highly notorious candidates for formulation development," *J. Control. Release*, vol. 248, pp. 71–95, 2017.

[11] S. Patnaik, "Novel nanoformulations for enhanced oral bioavailability of some poorly water soluble non steroidal anti inflammatory drugs," Sri Sathya Sai Institute of Higher Learning, 2016.

[12] P. Makary, "Principles of Salt Formation," *UK J. Pharm. Biosci.*, vol. 2, no. 4, pp. 1–4, 2016.

[13] A. T. M. Serajuddin, "Salt formation to improve drug solubility," *Adv. Drug Deliv. Rev.*, vol. 59, no. 7, pp. 603–616, 2007.

[14] R. G. Strickley, "Solubilizing excipients used in commercially available oral and injectable formulations," *Pharm. Res.*, vol. 21, no. 2, pp. 201–230, 2004.

[15] B. Gielen, P. Kusters, J. Jordens, L. C. J. Thomassen, T. Van Gerven, and L. Braeken, "Energy efficient crystallization of paracetamol using pulsed ultrasound," *Chem. Eng. Process. - Process Intensif.*, vol. 114, pp. 55–66, 2017.

[16] V. S. Nalajala and V. S. Moholkar, "Investigations in the physical mechanism of sonocrystallization," *Ultrason. Sonochem.*, vol. 18, no. 1, pp. 345–355, 2011.

[17] J. J. De Yoreo, "Principles of Crystal Nucleation and Growth," *Rev. Mineral. Geochemistry*, vol. 54, no. 1, pp. 57–93, 2005.

[18] J. W. Mullin, *Crystallization*, 4th ed. Oxford: Butterworth-Heinemann, 2001.

[19] J. Anwar, S. Khan, and L. Lindfors, "Secondary crystal nucleation: Nuclei breeding factory uncovered," *Angew. Chemie - Int. Ed.*, vol. 54, no. 49, pp. 14681–14684, 2015.

[20] "TOXNET." [Online]. Available: https://toxnet.nlm.nih.gov/cgi-bin/sis/search2/r?dbs+hsdb:@term+@rn+@rel+57-50-1. [Accessed: 01-May-2019].

[21] "Using AntiSolvent For Crystallization." [Online]. Available: https://www.mt.com/be/nl/home/applications/L1_AutoChem_Applications/L2_Crystallization/Anti-Solvent-Addition-on-Supersaturation.html. [Accessed: 03-Jun-2019].

[22] S. Mostafa Nowee, A. Abbas, and J. A. Romagnoli, "Antisolvent crystallization: Model identification, experimental validation and dynamic simulation," *Chem. Eng. Sci.*, vol. 63, no. 22, pp. 5457–5467, 2008.

[23] M. Giulietti and A. Bernardo, "Crystallization by Antisolvent Addition and Cooling," in *Crystallization - Science and Technology*, NA., M. Andreeta, Ed. Brasil: Intech, 2012, pp. 379–397.

[24] Janardhana Bantwal Baliga, "Crystal Nucleation and Growth Kinetics in Batch Evaporative Crystallization," Iowa State University, 1970.

[25] J. Hipple, "Evaporation and Crystallization," in *Chemical Engineering for Non-Chemical Engineers*, vol. 1, Hoboken, New Jersey: John Wiley & Sons Inc, 2017, pp. 203–219.

[26] X. M. ZENG, G. P. MARTIN, C. MARRIOTT, and J. PRITCHARD, "The Influence of Crystallization Conditions on the Morphology of Lactose Intended for Use as a Carrier for Dry Powder Aerosols," *J. Pharm. Pharmacol.*, vol. 52, no. 6, pp. 633–643, 2002.

[27] R. J. Davey, "The role of the solvent in crystal growth from solution," *J. Cryst. Growth*, vol. 76, no. 3, pp. 637–644, 1986.

[28] C. V. Luciani, E. W. Conder, and K. D. Seibert, "Modeling-aided scale-up of high-shear rotor-stator wet milling for pharmaceutical applications," *Org. Process Res. Dev.*, vol. 19, no. 5, pp. 582–589, 2015.

[29] "IKA Company." [Online]. Available: https://www.ikaprocess.com/en/Company/Company-comh-1.html. [Accessed: 30-Apr-2019].

[30] C. J. Brown, A. J. Florence, B. Ahmed, J. Sefcik, D. L. Bowering, and T. McGlone, "Engineering of acetaminophen particle attributes using a wet milling crystallisation platform," *Int. J. Pharm.*, vol. 554, no. August 2018, pp. 201–211, 2018.

[31] R. Buergelin, "Janssen Pharmaceutica N . V . Welcome to our seminar /// Scale up - Training," 2018, p. 105.

[32] J. Engstrom, C. Wang, C. Lai, and J. Sweeney, "Introduction of a new scaling approach for particle size reduction in toothed rotor-stator wet mills," *Int. J. Pharm.*, vol. 456, pp. 260–268, 2013.

[33] C. V. Luciani, "Impact of Process Parameters on the Grinding Limit in High-Shear Wet Milling," *Org. Process Res. Dev.*, vol. 22, no. 9, pp. 1328–1333, 2018.

[34] A. Harter, L. Schenck, I. Lee, and A. Cote, "High-shear rotor-stator wet milling for drug substances: Expanding capability with improved scalability," *Org. Process Res. Dev.*, vol. 17, pp. 1335–1344, 2013.

[35] J. G. Donovan, “Fracture Toughness Based Models for the Prediction of Power Consumption, Production Size and Capacity of Jaw Crushers,” Virginia Polytechnic Institute and State University, 2003.

[36] E. Stamboliadis, “A Novel Process for the Study of Breakage Energy versus Particle Size,” *Geomaterials*, vol. 03, no. 03, pp. 102–110, 2013.

[37] K. Ghaderzadeh and R. V Calabrese, “Crystal Wet Milling and Particle Attrition in High Shear Mixers,” 2017, no. September, p. 49.

[38] H. N. Kim and K. S. Suslick, “Sonofragmentation of Ionic Crystals,” *Chem. - A Eur. J.*, vol. 23, no. 12, pp. 2778–2782, 2017.

[39] D. Tromans and J. A. Meech, “Fracture toughness and surface energies of covalent minerals: Theoretical estimates,” *Miner. Eng.*, vol. 17, no. 1, pp. 1–15, 2004.

[40] R. D. Rawlings and C. B. Ponton, “Vickers indentation fracture toughness test part 1 review of literature and formulation of standardised indentation toughness equations,” *Mater. Sci. Technol.*, vol. 5, no. September, pp. 865–872, 1989.

[41] C. Gahn and A. Mersmann, “Theoretical prediction and experimental determination of attrition rates,” *Chem. Eng. Res. Des.*, vol. 75, no. 2, pp. 125–131, 1997.

[42] M. Ghadiri and Z. Zhang, “Impact attrition of particulate solids. Part 1: A theoretical model of chipping,” *Chem. Eng. Sci.*, vol. 57, no. 17, pp. 3659–3669, 2002.

[43] C. Gahn and A. Mersmann, “The brittleness of substances crystallized in industrial processes,” *Powder Technol.*, vol. 85, no. 1, pp. 71–81, 1995.

[44] L. J. Taylor *et al.*, “Predictive milling of pharmaceutical materials using nanoindentation of single crystals,” *Org. Process Res. Dev.*, vol. 8, no. 4, pp. 674–679, 2004.

[45] K. Ghaderzadeh, “CRYSTAL WET MILLING IN ROTOR-STATOR MIXERS,” University of Maryland, 2018.

[46] R. O. Williams III, A. B. Watts, and D. A. Miller, *Formulating Poorly Water Soluble Drugs*, 2nd ed., vol. 22. 2012.

[47] I. Lee, N. Variankaval, C. Lindemann, and C. Starbuck, “Rotor-stator Milling of APIs - Empirical Scale-up Parameters and Theoretical Relationships Between the Morphology and Breakage of Crystals,” *Am. Pharm. Rev.*, vol. 7, no. 5, pp. 120-123+128, 2004.

[48] S. Xu, J. Shi, Q. Cheng, W. Li, and J. Zhang, “Residence time distributions of in-line high shear mixers with ultrafine teeth,” *Chem. Eng. Sci.*, vol. 87, pp. 111–121, 2013.

[49] V. A. Atiemo-obeng, “Rotor – Stator Mixing Devices,” pp. 479–505, 2004.

[50] “magic LAB - Pilot plants,.” [Online]. Available: https://www.ikaprocess.com/en/Products/Pilot-plants-cph-40/magic-LAB-csb-MLAB/. [Accessed: 29-May-2019].

[51] “FBRM-meetmethode - METTLER TOLEDO.” [Online]. Available: https://www.mt.com/be/nl/home/library/videos/automated-reactors/Lasentec-FBRM-Method-of-Measurement.html. [Accessed: 18-Mar-2019].

[52] A. R. Heath, P. D. Fawell, P. A. Bahri, and J. D. Swift, “Estimating average particle size by focused beam reflectance measurement (FBRM),” *Part. Part. Syst. Charact.*, vol. 19, no. 2, pp. 84–95, 2002.

[53] C. Mayers, “Sieve analyses, laser diffraction, image analyses & FBRM,” 2013. [Online]. Available: https://www.ivoryresearch.com/writers/christopher-mayers-ivory-research-writer/. [Accessed: 01-Apr-2019].

[54] “ParticleTrack met FBRM-technologie - Overzicht - METTLER TOLEDO.” [Online]. Available: https://www.mt.com/be/nl/home/products/L1_AutochemProducts/FBRM-PVM-Particle-System-Characterization/FBRM.html. [Accessed: 28-May-2019].

[55] “PVM-technologie - Overzicht - METTLER TOLEDO.” [Online]. Available: https://www.mt.com/be/nl/home/products/L1_AutochemProducts/FBRM-PVM-Particle-System-Characterization/PVM.html. [Accessed: 29-May-2019].

[56] “Phenom - Pro - Desktop Scanning Electron Microscope by Phenom-World BV.” [Online]. Available: https://www.environmental-expert.com/products/phenom-model-pro-desktop-scanning-electron-microscope-326909. [Accessed: 28-May-2019].

[57] “Q150R Plus - Rotary Pumped Coater | Quorum Technologies.” [Online]. Available: https://www.quorumtech.com/quorum-product/q150r-rotary-pumped-sputter-coatercarbon-coater. [Accessed: 28-May-2019].

[58] “Scanning electron microscope | instrument | Britannica.com.” [Online]. Available: https://www.britannica.com/technology/scanning-electron-microscope. [Accessed: 28-May-2019].

[59] J. Jordens, T. Appermont, B. Gielen, T. Van Gerven, and L. Braeken, “Sonofragmentation: Effect of Ultrasound Frequency and Power on Particle Breakage,” *Cryst. Growth Des.*, vol. 16, no. 11, pp. 6167–6177, 2016.

[60] G. G. Stokes, “ON THE EFFECT OF THE INTERNAL FRICTION OF FLUIDS ON THE MOTION OF PENDULUMS.,” *Trans. Cambridge Philos. Soc.*, vol. 9, p. 8, 1850.

[61] W. C. Duncan-Hewitt and G. C. Weatherly, “Evaluating the hardness, Young’s modulus and fracture toughness of some pharmaceutical crystals using microindentation techniques,” *J. Mater. Sci. Lett.*, vol. 8, no. 11, pp. 1350–1352, 1989.

[62] P. C. Kapur and P. K. Agrawal, “Approximate solutions to the discretized batch grinding equation,” *Chem. Eng. Sci.*, vol. 25, no. 6, pp. 1111–1113, 1970.

APPENDIX

Appendix A – Technical drawing 2P-4M configuration HSWM

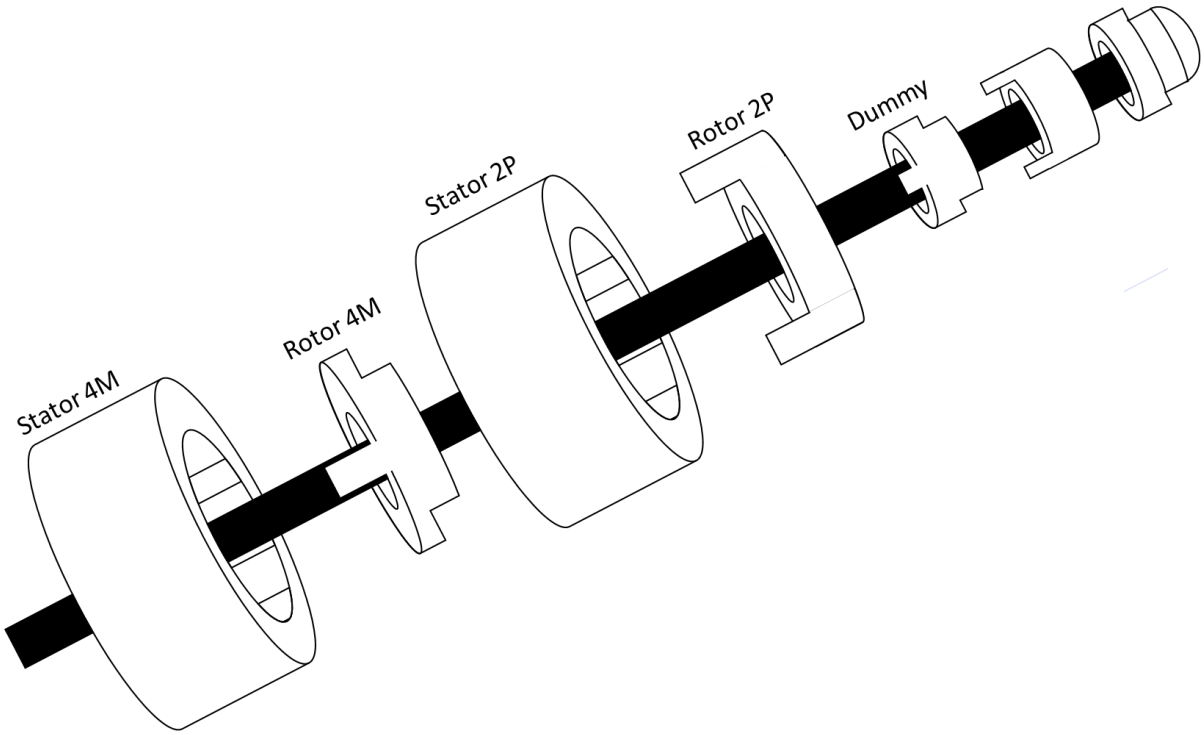

Figure 63 - 2P-4M configuration

Appendix B – Additional solid loading measurements

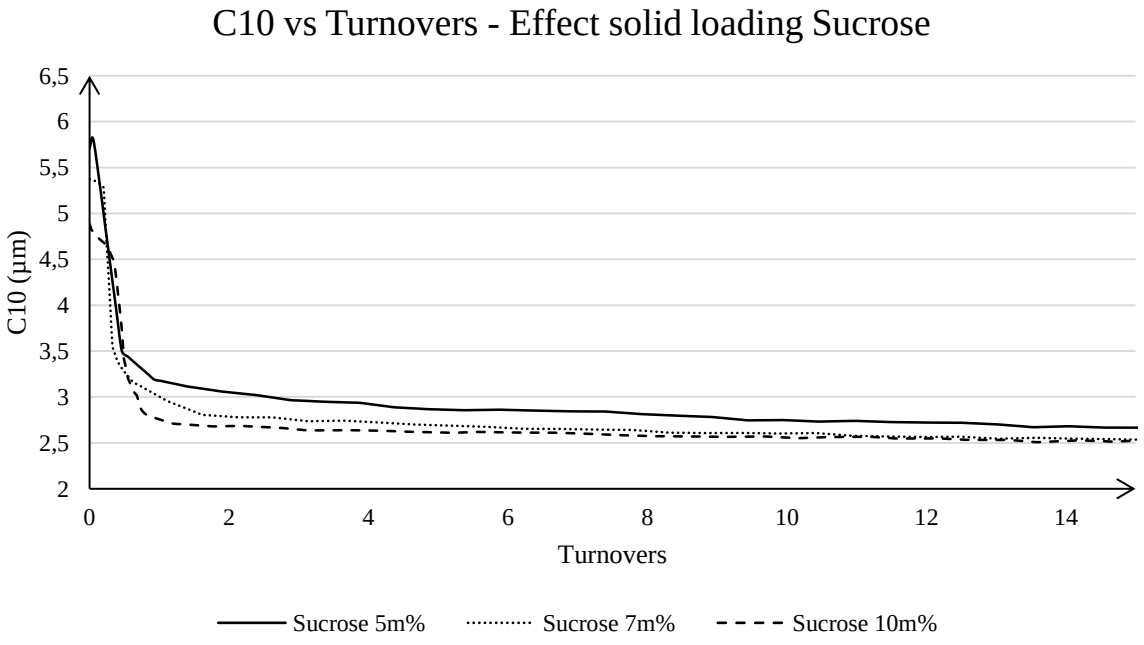

Figure 64 - C10 vs Turnovers - Effect solid Loading Sucrose

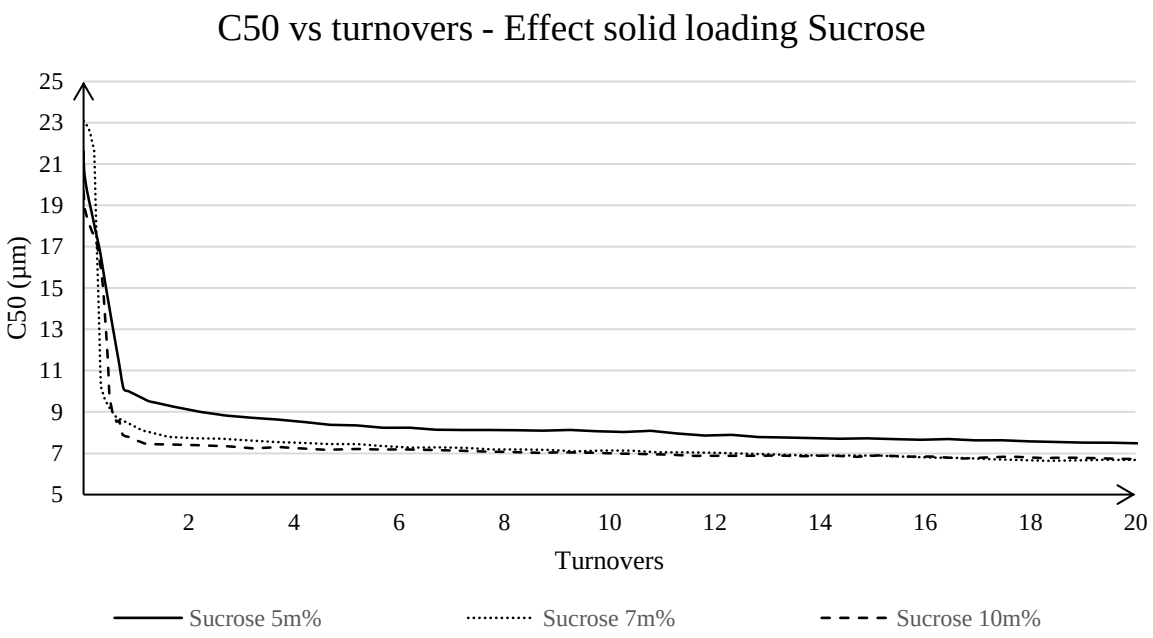

Figure 65 - C50 vs Turnovers - Effect solid loading Sucrose

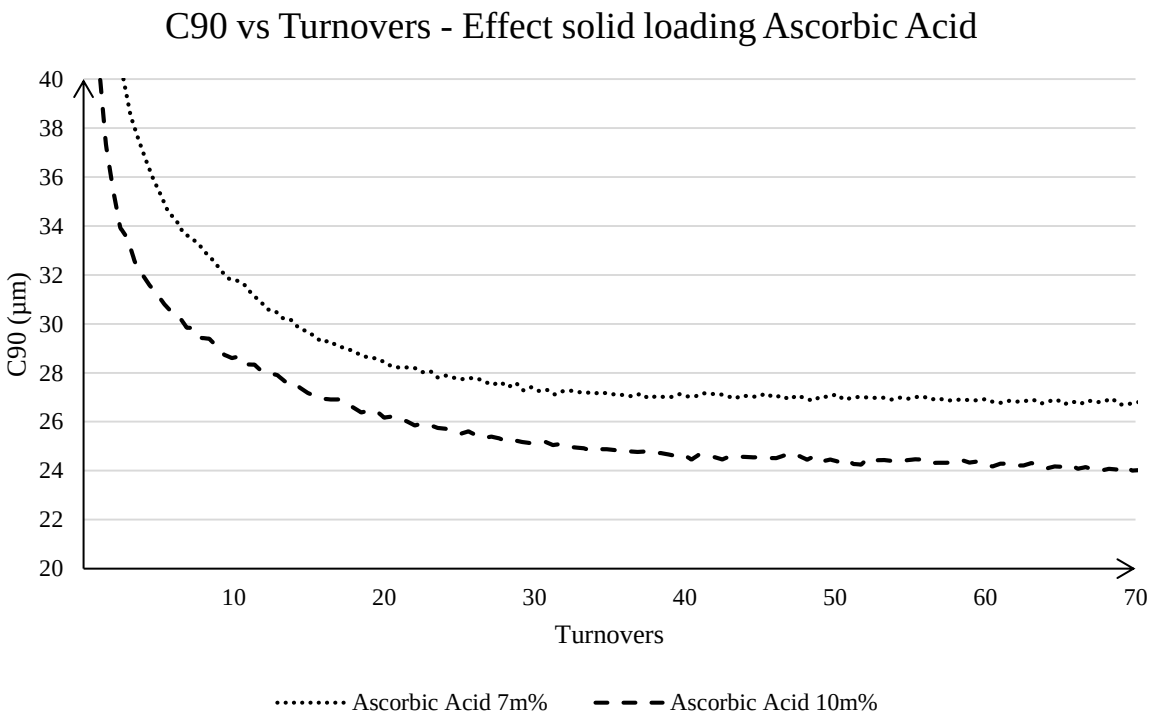

Figure 66 - C90 vs Turnovers - Effect solid loading Ascorbic Acid

Appendix C – Flowrate influence configuration

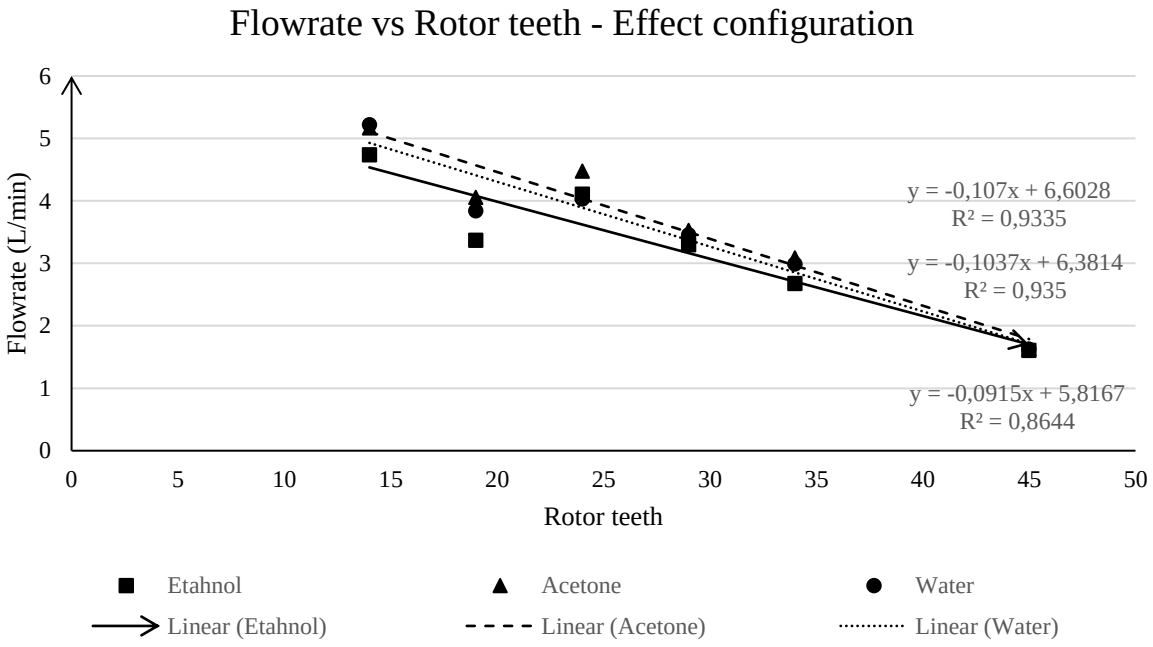

Figure 67 - Flowrate vs Rotor teeth- Effect configuration

Appendix D – Energy intake – Effect heat transfer coefficient

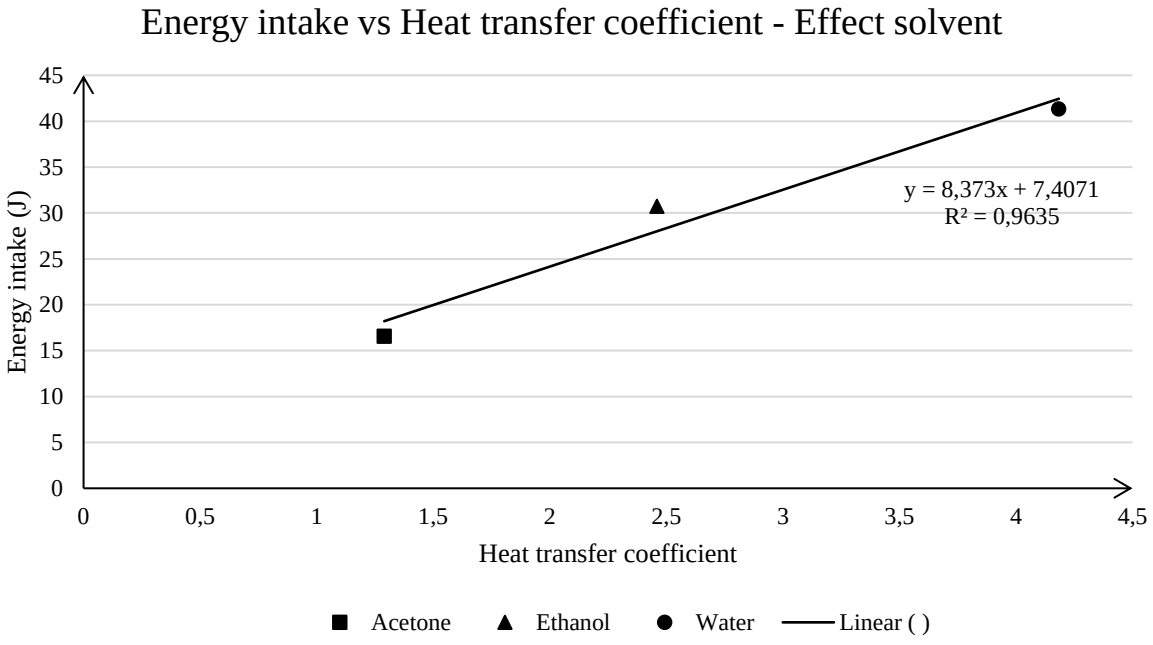

Figure 68 - Energy intake vs heat transfer coefficient - Effect solvent

Appendix E – Temperature increment due to configuration

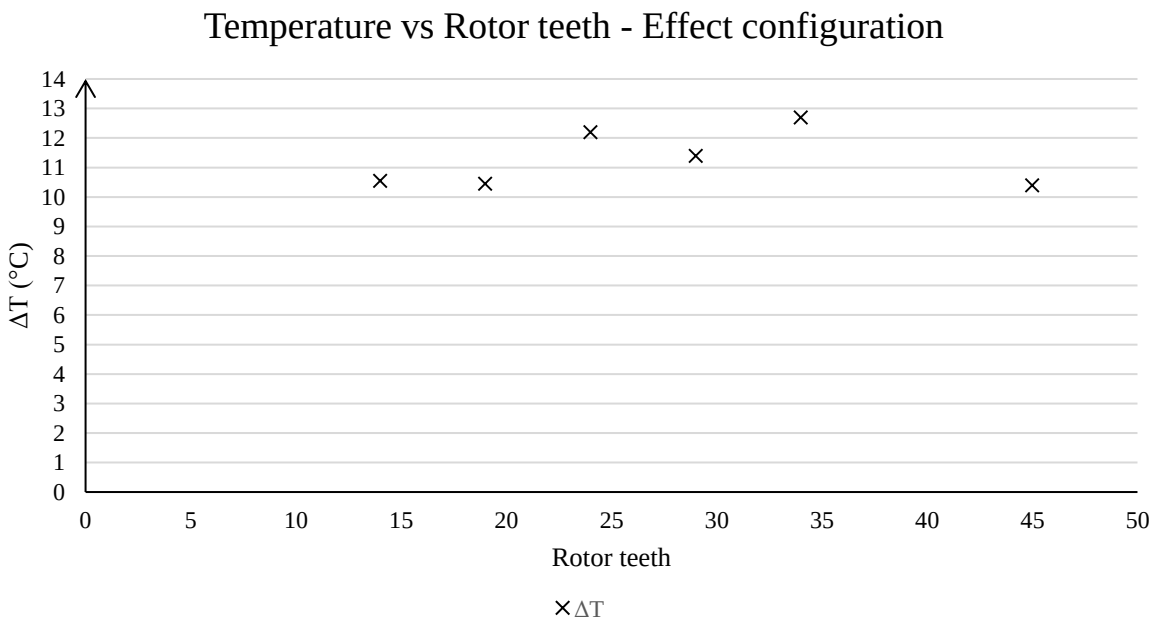

Figure 69 - Temperature increment vs Rotor teeth - Effect configuration

Appendix F – Macroscale Turbulence plot sodium chloride

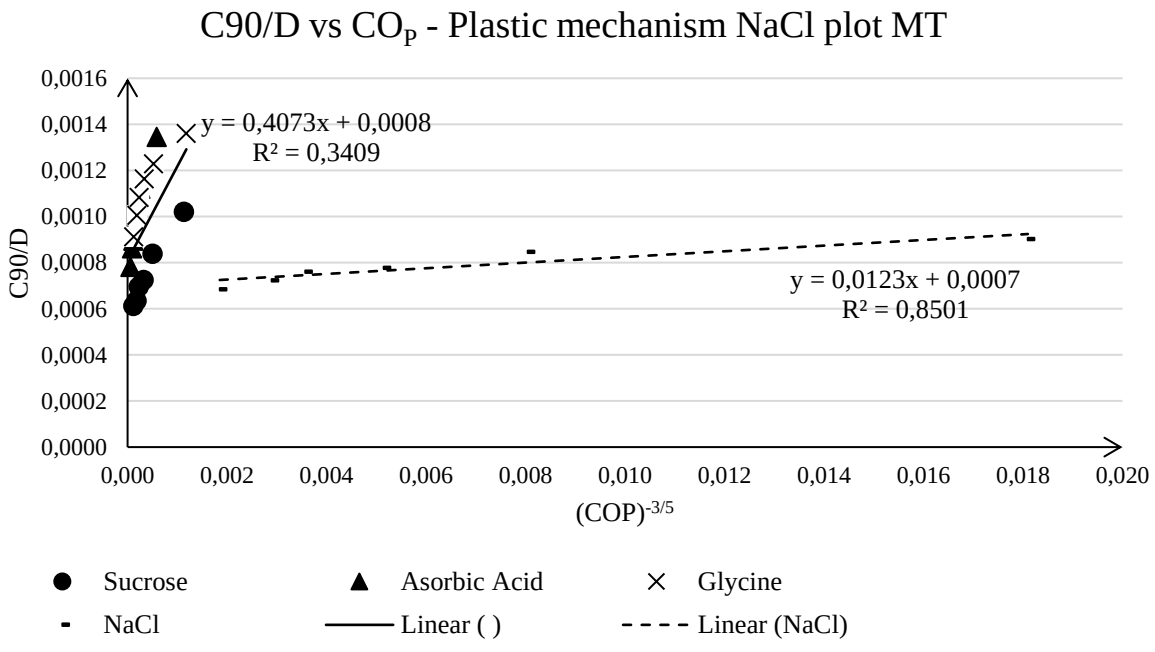

Figure 70 - C90/D vs CO_P - Plastic mechanism NaCl plot MT

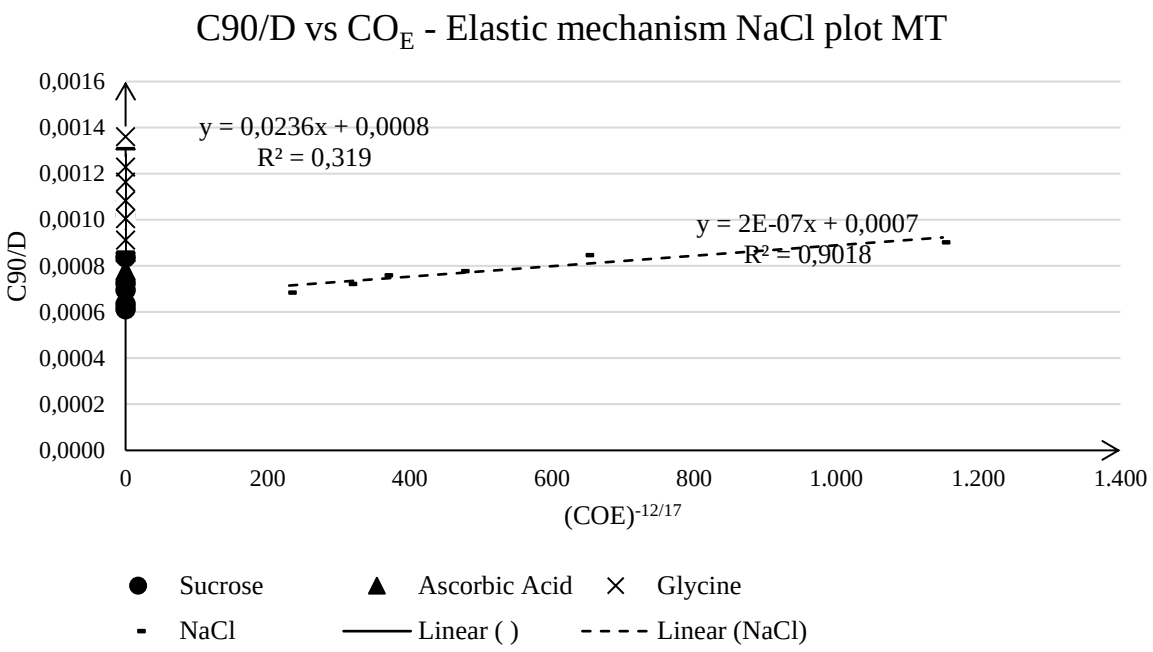

Figure 71 - C90/D vs CO_E - Elastic mechanism NaCl plot MT

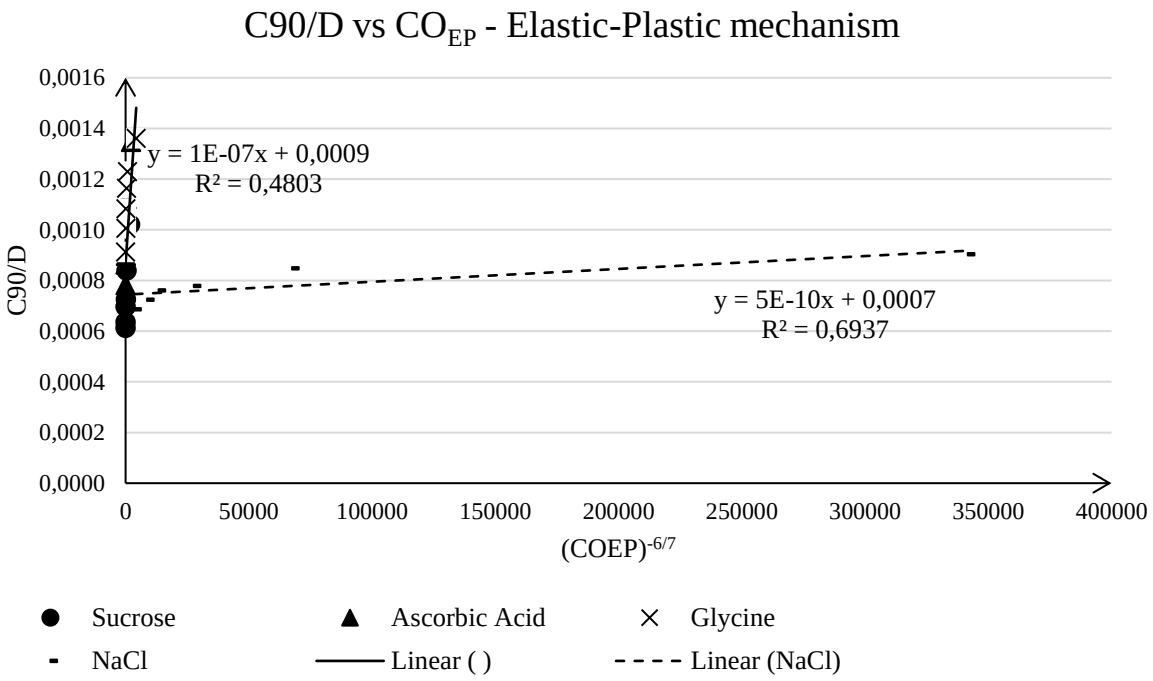

Figure 72 - C90/D vs CO_{EP} - Elastic-Plastic mechanism NaCl plot MT